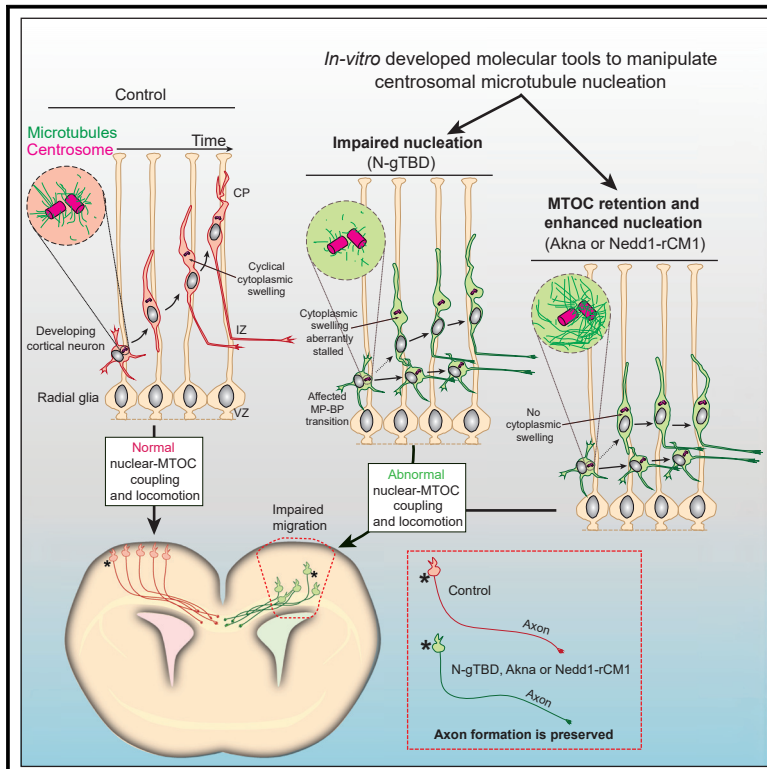# Centrosomal microtubule nucleation regulates radial migration of projection neurons independently of polarization in the developing brain

Graphical abstract

Authors

Stanislav Vinopal, Sebastian Dupraz, Eissa Alfadil, ..., Jiří Smejkal, Magdalena Götz, Frank Bradke

Correspondence

frank.bradke@dzne.de

In brief

Combining a novel expression system with live *in vivo* imaging, three-dimensional two-photon imaging, and centrosomal ablation, Vinopal and Dupraz et al. demonstrate that neurons need centrosomal microtubule nucleation for their radial migration but not axon formation.

Highlights

- Neurons polarize independently of centrosomal microtubule nucleation (CMN)

- The centrosome loses γ-tubulin as neurons enter the cortical plate

- CMN changes correlate with the cytoplasmic dilation in radially migrating neurons

- CMN regulates radial migration independently of axon formation in the developing brain

CellPress

Article

Centrosomal microtubule nucleation regulates radial migration of projection neurons independently of polarization in the developing brain

Stanislav Vinopal,[1,2,3,12] Sebastian Dupraz,[1,12] Eissa Alfadil,[1,13] Thorben Pietralla,[1,4,13] Shweta Bendre,[1] Michael Stiess,[1] Sven Falk,[5,6,10] Germán Camargo Ortega,[5,6,11] Nicola Maghelli,[7] Iva M. Tolić,[7,8] Jiří Smejkal,[2] Magdalena Götz,[5,6,9] and Frank Bradke[1,14,*]

[1]Laboratory of Axonal Growth and Regeneration, German Center for Neurodegenerative Diseases (DZNE), Bonn, Germany
[2]Centre for Nanomaterials and Biotechnology, Faculty of Science, Jan Evangelista Purkyne University, Usti nad Labem, Czech Republic
[3]Department of Biology, Faculty of Science, Jan Evangelista Purkyne University, Usti nad Labem, Czech Republic
[4]International Max Planck Research School for Brain and Behavior, Bonn, Germany
[5]Institute of Stem Cell Research, Helmholtz Center Munich, German Research Center for Environmental Health, Planegg-Martinsried, Germany
[6]Physiological Genomics, Biomedical Center, Ludwig-Maximilians University, Planegg-Martinsried, Germany
[7]Max Planck Institute of Molecular Cell Biology and Genetics, Dresden, Germany
[8]Ruđer Bošković Institute, Zagreb, Croatia
[9]Excellence Cluster SyNergy, Biomedical Center, LMU, Planegg-Martinsried, Germany
[10]Present address: Institute of Biochemistry, Friedrich-Alexander-University Erlangen-Nuremberg, Erlangen, Germany
[11]Present address: Department of Biosystems Science and Engineering, ETH Zurich, Switzerland
[12]These authors contributed equally
[13]These authors contributed equally
[14]Lead contact
*Correspondence: frank.bradke@dzne.de
https://doi.org/10.1016/j.neuron.2023.01.020

SUMMARY

Cortical projection neurons polarize and form an axon while migrating radially. Even though these dynamic processes are closely interwoven, they are regulated separately—the neurons terminate their migration when reaching their destination, the cortical plate, but continue to grow their axons. Here, we show that in rodents, the centrosome distinguishes these processes. Newly developed molecular tools modulating centrosomal microtubule nucleation combined with *in vivo* imaging uncovered that dysregulation of centrosomal microtubule nucleation abrogated radial migration without affecting axon formation. Tightly regulated centrosomal microtubule nucleation was required for periodic formation of the cytoplasmic dilation at the leading process, which is essential for radial migration. The microtubule nucleating factor γ-tubulin decreased at neuronal centrosomes during the migratory phase. As distinct microtubule networks drive neuronal polarization and radial migration, this provides insight into how neuronal migratory defects occur without largely affecting axonal tracts in human developmental cortical dysgeneses, caused by mutations in γ-tubulin.

INTRODUCTION

Building the brain involves a concerted and dynamic choreography of myriads of cells. After divisions in the ventricular zone (VZ) or subventricular zone (SVZ) of the cortex, newly born projection neurons migrate radially toward their destination in the cortical plate (CP) while transforming their morphology.[1] The neurons form their axons during migration in the intermediate zone (IZ) before they transit from their multipolar-to-bipolar morphology; others form an axon after they start locomoting and leave an axon behind as a trailing process, which then continues to

grow.[2,3] How neurons control these interwoven processes distinctly has remained unclear.

Microtubules (MTs) play instructive roles in both neuronal radial migration[4–6] and polarization.[7,8] In migrating neurons, MTs establish the force-generating scaffold in the leading process, underlying the nucleokinetic movement responsible for saltatory glial-guided locomotion.[5,6,9,10] Through interactions with the actin cytoskeleton,[11] MTs also propel axon initiation and growth.[12–14] But what is the underlying mechanism separating the movement of the cell body toward the CP while simultaneously enabling axon growth in the opposite direction?
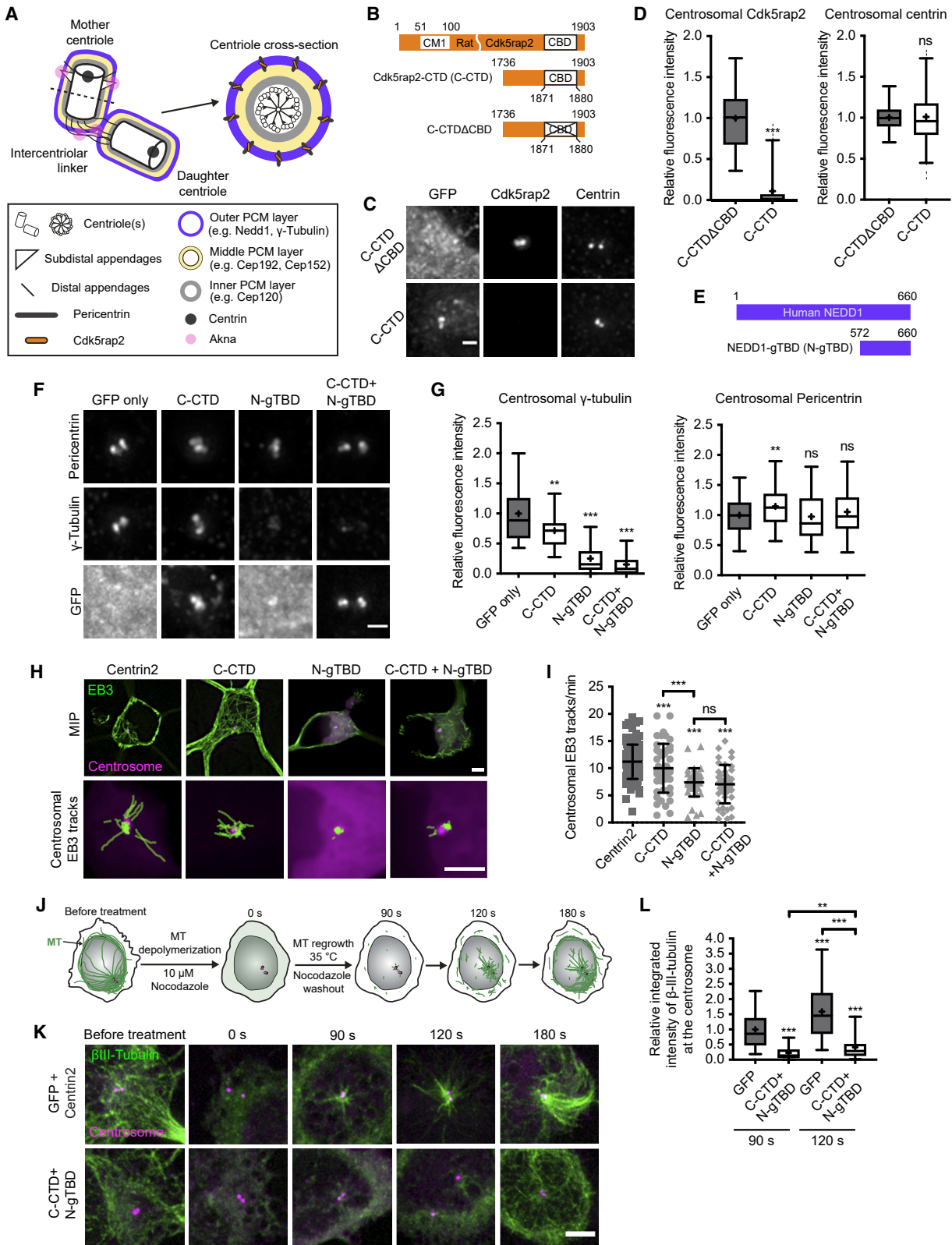
(legend on next page)

Given its function as a key MT-organizing center (MTOC)[15] and a signaling hub,[16–19] the centrosome may be involved in both radial migration and neuronal polarization. Centrosomal mother centrioles can transform into basal bodies that give rise to primary cilia: important signaling organelles involved in neocortical development,[20,21] including axonogenesis.[22,23] The role of the centrosome as an MTOC during neuronal polarization has remained less defined. A genetic study in *Drosophila* and centrosome laser ablation in already polarized rat hippocampal neurons *in vitro* demonstrated that axon extension can occur independently of the centrosome.[24,25] Yet, the centrosome is still active as an MTOC in nascent neurons,[25–27] making it an attractive putative regulator of neuronal polarization as proposed in several studies;[28–33] however, this has remained unclear.[34–38] It is even possible that centrosomal MT nucleation may inhibit neuronal polarization by inhibiting or competing with acentrosomal MT networks for nucleation factors and soluble tubulin.[39–41]

The role of the centrosome during radial migration also remains to be investigated. Although the centrosome appears to control the radial migration of projection neurons,[6,9,18,27,42–44] parallel centrosome depletion and apoptotic signaling inhibition using *Cenpj/p53* double knockout mice do not grossly perturb physiological cortical layering.[45] Taken together, the role of centrosomal MT nucleation in radial migration and axon formation remains largely undefined.

Here, we uncover that neurons polarize independently of centrosomal MT nucleation in the developing cortex and yet require it for radial migration. Intriguingly, neurons lose the MT-nucleating factor γ-tubulin from the centrosome upon migrating to the CP where they will reside, albeit continuing the growth of their axon. The involvement of distinct microtubular networks in radial migration and polarization provides a novel perspective on how mutations in human γ-tubulin gene *TUBG1*, which cause developmental pachygyrias, impair primarily neuronal migration, but not axon tract formation.

RESULTS

Development of tools to inactivate MT nucleation at the neuronal centrosome

To study the role of centrosomal MT nucleation during neuronal polarization and radial migration, we developed tools to inactivate it in nascent neurons. The key catalyzer of MT nucleation is the γ-tubulin ring complex[46,47] (γ-TuRC) and its major centrosome-targeting factor is neural precursor cell expressed developmentally downregulated 1[48,49] (Nedd1). γ-TuRC is enriched at the centrosome periphery[50] (Figure 1A) but is primarily found in the cytoplasm.[51] Cyclin-dependent kinase 5 regulatory subunit-associated protein 2 (Cdk5rap2) is a centrosomal protein that activates γ-TuRC to drive centrosomal MT nucleation.[52,53] We therefore displaced Cdk5rap2 and γ-TuRC from the centrosome to inactivate its function.

To displace centrosomal Cdk5rap2, we overexpressed its centrosome-targeting carboxy-terminal domain[54] (CTD) fused to *Aequorea coerulescens* (Ac) green fluorescent protein (GFP) (AcGFP), hereafter called C-CTD, in embryonic day 17 (E17) cultured rat hippocampal neurons (Figure 1B). C-CTD localized to the centrosome and displaced endogenous Cdk5rap2 by 1 day *in vitro* (DIV) (Figures 1C and 1D; 89% ± 6%, mean ± SEM), when neurons were unpolarized. Expression of an AcGFP-tagged Cdk5rap2 fragment that lacked the centrosome-binding domain (CBD), C-CTDΔCBD, left endogenous centrosomal Cdk5rap2 intact (Figures 1C and 1D). Levels of the core centrosomal protein centrin (Figure 1A) were not affected by Cdk5rap2 displacement (Figures 1C and 1D).

To displace endogenous γ-TuRC from the centrosome, we overexpressed the γ-tubulin-binding domain (gTBD) of

---

Figure 1. Displacement of γ-tubulin impairs centrosomal MT nucleation in neurons

(A) A schematic of the centrosome structure. The centrosome consists of two centrioles that are surrounded by pericentriolar material (PCM) and connected by the centrosomal linker.

(B) A schematic of a rat Cdk5rap2 protein (GenePept: XP_006238335.1) and its truncation mutants. CM1 is the γ-TuRC-binding and activating domain. CBD is the centrosome-binding domain. Numbers indicate positions of amino acids (AA).

(C) Maximum intensity projections (MIP) of the pericentrosomal area. Note that centrin is located at the distal part of the centriole whereas Cdk5rap2 and C-CTD localize to the PCM, enveloping both centrioles and resulting in a slight apposition of both signals. Scale bar, 1 μm.

(D) Quantification of fluorescence intensity at the centrosome in (C). N = 3; C-CTDΔCBD, n = 62; C-CTD, n = 67; ***p = 4.21 × 10^{-6} for Cdk5rap2; ns for centrin. Generalized linear model (GLM) with γ-distribution.

(E) A schematic of a human NEDD1 protein and its truncation mutant. N-gTBD is the γ-tubulin-binding domain of NEDD1.

(F) MIP of the pericentrosomal area in neurons overexpressing indicated fragments. Unlike in other channels, intensities in the GFP channel are not comparable because soluble N-gTBD and GFP signals are greatly diminished after methanol fixation. Scale bar, 1 μm.

(G) Quantification of fluorescence intensity at the centrosome in (F). GFP, N = 5, n = 142; C-CTD, N = 3, n = 99; N-gTBD, N = 3, n = 99; N-gTBD+C-CTD, N = 3, n = 76; ***p < 0.001, **p < 0.01, GLM with γ-distribution. All conditions compared with GFP only. See also Figure S1.

(H) Representative images of EB3 tracks. MIPs of the first 60 frames from videos and detected centrosomal EB3 tracks (green) in whole 3-min videos in the same cells. Scale bars, 3 μm.

(I) Quantification of the number of centrosomal EB3 tracks per minute. Centrin2, N = 9, n = 133; for the rest of the conditions N = 3; C-CTD, n = 45; N-gTBD, n = 41; N-gTBD+C-CTD, n = 43; ***p < 0.001; GLM with Poisson distribution and simultaneous tests for GLM (R multcomp package). Data are presented as mean ± SD. For co-expression with EB3-mNeonGreen, C-CTD was tagged with td-mCherry and N-gTBD with mOrange2. See also Video S1.

(J) A schematic of the MT regrowth experiment.

(K) Representative examples of MT regrowth from the centrosome in control (GFP + Centrin2-tdTomato) and N-gTBD + C-CTD overexpressing neurons. Scale bar, 3 μm.

(L) Quantification of fluorescence intensity of βIII-tubulin at the centrosome at the indicated time points. 90 s: GFP only, N = 4, n = 138; N-gTBD+C-CTD, N = 4, n = 117; 120 s: GFP only, N = 3, n = 108; N-gTBD + C-CTD, N = 3, n = 98; ***p < 0.0001, **p = 0.0024. Brown-Forsythe and Welch ANOVA tests with Games-Howell's multiple comparisons test. Data are presented as boxplots. DIV1 rat hippocampal neurons. ns = nonsignificant.
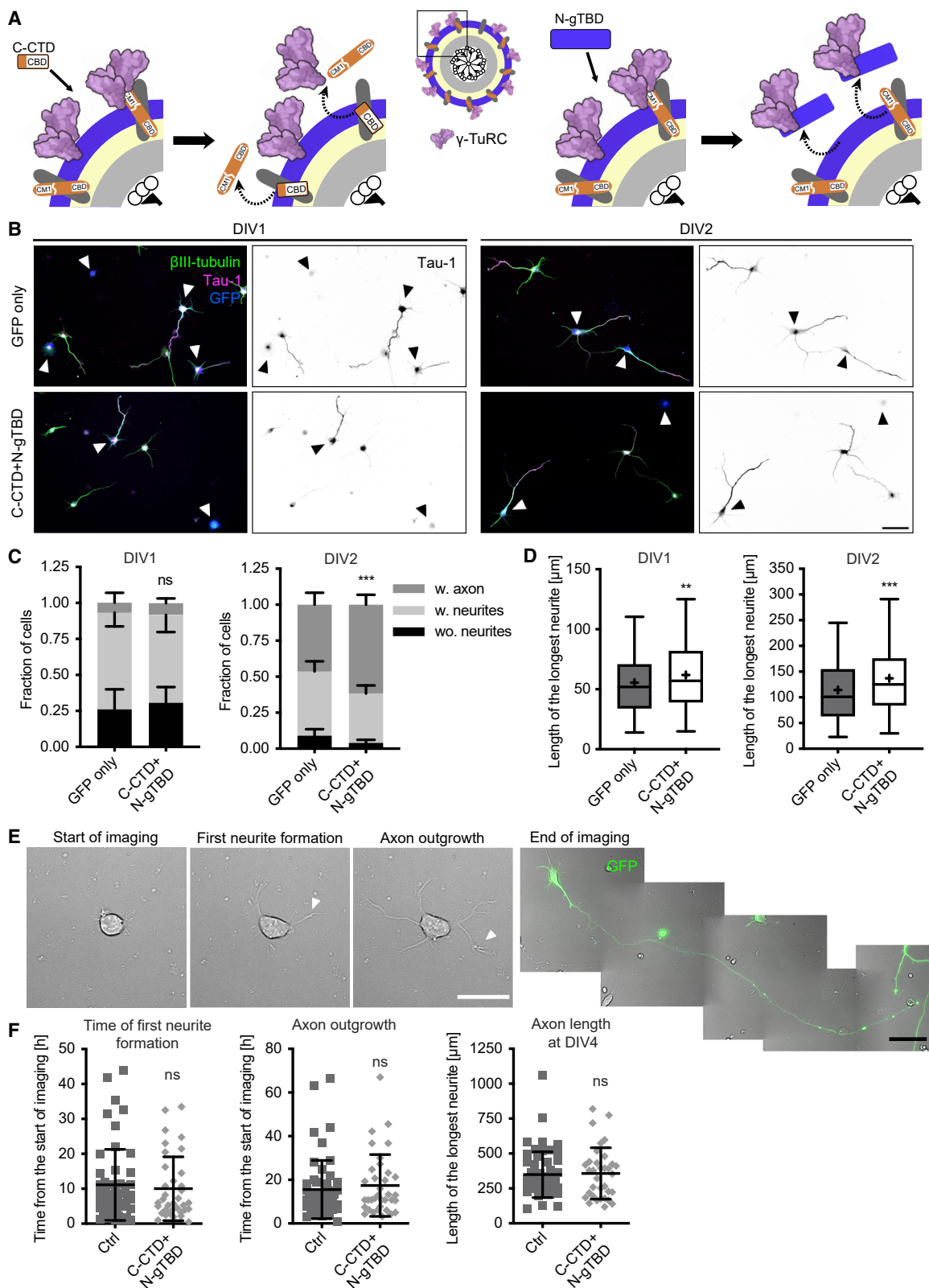
(legend on next page)

NEDD1[55] fused to enhanced (E) GFP, hereafter called N-gTBD, in E17 neurons (Figure 1E). N-gTBD overexpression in neurons displaced 75% ± 5% (mean ± SEM) of centrosomal γ-tubulin compared with control cells overexpressing only GFP (Figures 1F and 1G).

In addition to activating γ-TuRC, Cdk5rap2 anchors a subset of γ-tubulin complexes to the centrosome in non-neuronal cells.[53,56] In neurons, Cdk5rap2 displacement by C-CTD overexpression reduced centrosomal γ-tubulin by 28% ± 5% (mean ± SEM; Figures 1F and 1G). Consistently, overexpression of N-gTBD and C-CTD together depleted 85% ± 5% (mean ± SEM) of γ-tubulin from the centrosome (Figures 1F and 1G) and also displaced exogenous centrosomal γ-tubulin (Figure S1A). The centrosomal component Pericentrin was not negatively affected (Figures 1F and 1G).

We next tested whether the newly developed tools downregulate centrosomal MT nucleation. To this end, we transfected neurons with end-binding protein 3 (EB3), a marker of polymerizing MT plus ends,[57] fused to mNeonGreen. Automated analysis of EB3 tracks initiating at the centrosome, labeled by C-CTD or Centrin2-tdTomato,[36] showed that centrosomal MT nucleation is equally impaired in cells overexpressing N-gTBD or N-gTBD + C-CTD at DIV1 (Figures 1H and 1I; Video S1). Interestingly, centrosomal depletion of Cdk5rap2 by C-CTD alone caused only a small decrease in centrosomal MT nucleation (Figures 1H and 1I). Thus, in contrast to non-neuronal cells,[52,53] Cdk5rap2 plays only a minor role in activating centrosomal γ-TuRC in neurons. Consequently, overexpression of N-gTBD or N-gTBD + C-CTD was equally effective in impairing centrosomal MT nucleation.

Similarly, MT regrowth after nocodazole wash-out (Figure 1J) was greatly reduced in N-gTBD + C-CTD overexpressing neurons, contrasting the distinct and focused centrosomal MT asters formed in controls (Figures 1K and 1L). In conclusion, our molecular tools impair centrosomal MT nucleation in nascent neurons by displacing γ-tubulin from the centrosome. This provides the opportunity to investigate the role of centrosomal MT nucleation during neuronal polarization and migration.

Neurons polarize without centrosomal MT nucleation

To distinguish between the role of centrosomal MT nucleation in cellular migration and neuronal polarization, we first investigated neuronal polarization in cultured neurons. These neurons do not migrate *in vitro*, facilitating a focus on polarization. Immunocyto-

chemistry showed that neurons overexpressing N-gTBD + C-CTD (Figure 2A) polarized equivalently to control neurons overexpressing GFP alone (Figures 2B and 2C). Approximately two-thirds of neurons formed neurites after DIV1; after DIV2, approximately one-half of neurons had formed an axon, as marked by the axonal marker Tau-1 (Figures 2C and 2D). N-gTBD + C-CTD-overexpressing neurons showed even a slight increase in both axon formation and the length of the longest neurite compared with controls. Also, at DIV5, when dendrites have molecularly segregated and are enriched for the microtubule-associated protein 2 (Map2),[58] N-gTBD + C-CTD-overexpressing neurons were indistinguishable from control neurons—the number and lengths of axons and dendrites were equal (Figures S2A and S2B). The only subtle difference found was that axon branching and total axon length were slightly decreased in N-gTBD + C-CTD-overexpressing neurons compared with controls. As this effect was observed for all tested conditions (Figures S2A and S2B), it appears to be unspecific for downregulation of centrosomal microtubule nucleation. Long-term video-microscopic analysis revealed that round, unpolarized N-gTBD + C-CTD-overexpressing neurons formed the first neurite, as well as their axon, in intervals indistinguishable from control neurons (Figures 2E and 2F; Video S2). We followed these neurons to DIV4 and found that the axon reached the same length in both conditions (Figures 2E and 2F).

To test our findings using an alternative approach, we ablated the centrosome via two-photon laser ablation in round, unpolarized neurons lacking neurites (Figure S1E). We previously used this technique to remove the centrosome from already polarized neurons possessing an axon.[25] To this end, round, unpolarized neurons overexpressing Centrin2-EGFP were plated on photoetched grid coverslips, allowing identification and imaging at later time points after centrosome ablation. Removal of the centrosome was validated by immunostaining for γ-tubulin and Pericentrin in neurons 2 days after laser ablation (Figures S1F and S1G; Stiess et al.[25]). We found that the longest neurites reached similar lengths in neurons with ablated centrosomes and in those that did not undergo laser ablation, or where γ-tubulin and Pericentrin were retained after attempted laser ablation (Figure S1H). Taken together, neither centrosomal MT nucleation nor an intact centrosome structure are required for neuronal polarization *in vitro*.

We also tested Golgi-mediated MT nucleation as an acentrosomal source for the generation of MTs.[59–61] To this end, we

Figure 2. Neurons polarize independently of centrosomal MT nucleation

(A) A schematic of γ-tubulin displacement upon overexpression of C-CTD and N-gTBD.

(B) Representative images of rat neurons overexpressing either GFP only or N-gTBD+C-CTD at DIV1 and DIV2. Gradient of Tau-1 was used as an axonal marker. Scale bar, 50 μm. The image of N-gTBD+C-CTD at DIV2 is a combination of tiles.

(C) Fractions of neurons in developmental stages at DIV1 and DIV2 with (w.) axons or neurites or without (wo.) them. DIV1: N = 6, n ≥ 674 for each condition; DIV2: N = 5, n ≥ 782 for each condition; ***p = 2.7 × 10^{-12}. Ordinal logistic regression model. Data are presented as mean ± SD.

(D) Length of the longest neurite at DIV1 and DIV2. DIV1: N = 6, n ≥ 459; DIV2: N = 5, n ≥ 753; ***p < 0.0001, **p = 0.0021. Unpaired Welch's t test. Analysis of the same dataset as in (C), excluding neurons without neurites. Data are presented as boxplots.

(E) Live imaging of rat neurons overexpressing mOrange2 with EGFP-Centrin2 (Ctrl) or GFP-tagged N-gTBD + C-CTD. Imaging started when neurons were still non-polarized (without neurites, stage 1). An N-gTBD + C-CTD overexpressing neuron is depicted. White scale bar 25 μm, black scale bar, 50 μm. The image on the right was stitched using Fiji (MosaicJ).

(F) Quantification of polarization events and the length of the longest neurite at DIV4, N = 3. The first neurite formation: Ctrl, n = 53; N-gTBD + C-CTD, n = 35; Axon outgrowth: Ctrl, n = 53; N-gTBD + C-CTD, n = 35; Axon length at DIV4: Ctrl, n = 53; N-gTBD + C-CTD, n = 34. Unpaired Welch's t test. Data are presented as mean ± SD. See also Video S2. ns = nonsignificant.
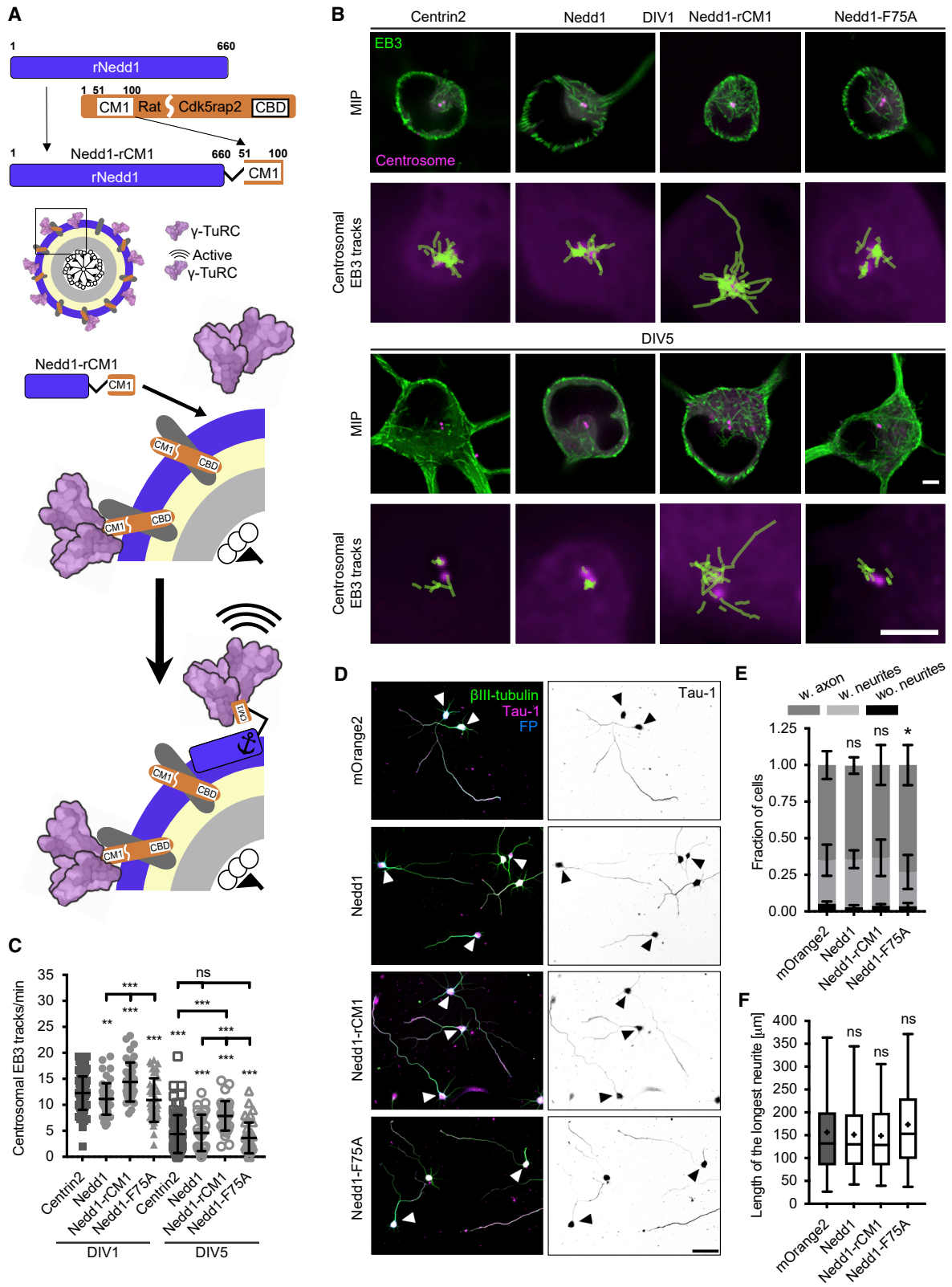
blocked Golgi-mediated MT nucleation by displacing A-kinase anchor protein 9 (Akap9), the molecular linker between the Golgi matrix protein 130 (GM-130), a peripheral membrane protein attached to the *cis*-Golgi, and Cdk5rap2, as well as myomegalin variants that directly bind to γ-TuRC.[40] We employed an Akap9 fragment that competitively displaces AKAP9 from GM-130 in human cells[62] (Figure S3A). Indeed, overexpression of a rat homolog of such a fragment, which we named "Akap9-dis," displaced Akap9 from the Golgi membrane (Figures S3B and S3C).

Consequently, Golgi-mediated MT nucleation was markedly impaired in neurons overexpressing Akap9-dis at DIV1. Similar to the centrosome, Golgi-mediated MT nucleation was downregulated in neurons at DIV5—displacing Akap9 at that time point did not show any additive effect (Figures S3D and S3E; Video S3). In contrast to the impairment of centrosomal microtubule nucleation, neurons overexpressing Akap9-dis had shorter axons at DIV2 (Figures S3F–S3H). This phenotype was even more pronounced at DIV5 (Figures S2C and S2D). Detailed morphological analysis further revealed that impairment of Golgi-mediated MT nucleation also decreased the total length of the axon but increased the number of neurites and axonal branching (Figures S2C and S2D). Thus, Golgi-mediated MT nucleation supports axonal growth, contrasting the centrosome's dispensability for this process.

Downregulation of centrosomal MT nucleation is dispensable for neuronal polarization

As the centrosome loses its MT-nucleating activity during polarization,[25,63] it raises the possibility that downregulation of centrosomal MT nucleation may be necessary for polarization. To test this, we developed a strategy to enhance and prolong centrosomal MT nucleation.

The neuronal centrosome was inert to manipulations that activated the MT-nucleating function of non-neuronal centrosomes in dividing cells.[52,53,56] First, overexpression of full-length rat Cdk5rap2 failed to increase centrosomal MT nucleation at DIV1 or DIV5 (Figures S1C and S1D; Video S4), further corroborating that Cdk5rap2 is not a major activator of centrosomal γ-TuRCs in neurons. Second, the centrosomin motif 1 (CM1) at the N terminus of CDK5RAP2 activates γ-TuRC.[52,64] When overexpressed in fusion with the Pericentrin-AKAP450 centrosomal targeting (PACT) domain,[65] PACT-hCM1 localized to the centro-

some but failed to increase centrosomal MT nucleation (Figures S1C and S1D; Video S4).

One reason for this may be that PACT-hCM1 targets deeper pericentriolar material (PCM) layers, preventing interaction with γ-TuRCs.[66] Hence, we explored whether Nedd1, localized to the outer layer of PCM, together with γ-TuRCs,[66] could be used as a carrier for CM1. Of note, downregulation of Nedd1 is thought to be the primary cause of physiological γ-TuRC depletion from the neuronal centrosome.[25,64] Although overexpressed full-length Nedd1-mOrange2 localized to the centrosome (Figure S4A), centrosomal MT nucleation remained unchanged after DIV1 or DIV5 (Figures 3B and 3C; Video S4). Intriguingly, Nedd1 overexpression reduced both exogenous and endogenous γ-tubulin at the centrosome (Figures S1B, S4A, and S4B). Hence, increasing Nedd1 in the cell decreases γ-tubulin steady-state levels at the centrosome. Fluorescence recovery after photobleaching (FRAP) revealed that Nedd1 increases centrosomal γ-tubulin mobility (Figures S4E–S4G), suggesting that Nedd1 shuttling of γ-tubulin is not rate limiting for centrosomal MT nucleation.

Based on these results, we used Nedd1 to target CM1 to the centrosome to activate γ-TuRC (Figure 3A). To ensure that no species-dependent differences impacted the activity of the Nedd1-CM1 fusion, we used not only hCM1 but also a CM1 from rat Cdk5rap2 (rCM1). As expected, Nedd1-rCM1 decreased centrosomal γ-tubulin levels (Figures S4A and S4B). Strikingly, neurons overexpressing either Nedd1-hCM1 or Nedd1-rCM1 increased centrosomal MT nucleation at DIV1 when compared with neurons overexpressing Centrin2-tdTomato or Nedd1 fused to rCM1 containing a point mutation (F75A), rendering CM1 incapable of binding and activating γ-TuRC,[52] termed "Nedd1-F75A" (Figures 3B, 3C, S1C, and S1D; Video S4). Importantly, at DIV5, when centrosome activity is downregulated (Figures 3B and 3C; Stiess et al.[25]), Nedd1-hCM1 or Nedd1-rCM1 overexpression almost doubled centrosomal MT nucleation compared with controls (Figures 3B, 3C, S1C, and S1D; Video S4).

When we investigated whether activation of the MT nucleation at the centrosome affects neuronal polarization, we found that Nedd1-rCM1 overexpressing neurons were largely unaffected. Progression through the developmental stages, axon formation, and the length of the longest neurite were unchanged compared with control neurons overexpressing mOrange2

Figure 3. Centrosomal MTOC activation does not prevent neuronal polarization

(A) A schematic of Nedd1-CM1 chimera function.

(B) Representative images of EB3 tracks in DIV1 and DIV5 rat hippocampal neurons. MIPs of the first 60 frames from videos and detected centrosomal EB3 tracks (green) in whole 3-min videos in the same cells. Scale bars, 3 μm.

(C) Quantification of the number of centrosomal EB3 tracks per minute. DIV1: Centrin2, N = 6, n = 82 cells; Nedd1, N = 3, n = 45; Nedd1-rCM1, N = 3, n = 40; Nedd1-F75A, N = 3, n = 40. DIV5: Centrin2, N = 6, n = 74, Nedd1, N = 3, n = 33; Nedd1rCM1, N = 3, n = 36; Nedd1-F75A, N = 3, n = 38. ***p < 0.001; **p = 0.003. GLM with Poisson distribution and simultaneous tests for GLM (R multcomp package). Data are presented as mean ± SD. See also Video S4.

(D) Representative images of neurons overexpressing indicated constructs at DIV2. Control neurons overexpressed mOrange2 only. Neurons overexpressing Nedd1 variants were detected using anti-Nedd1 antibody. Scale bar, 50 μm.

(E) Fractions of rat neurons in developmental stages at DIV2 with (w.) axons or neurites or without (wo.) them. N = 3, n ≥ 414 for each condition; *p = 0.012. Ordinal logistic regression model. Data are presented as mean ± SD.

(F) Length of the longest neurite at DIV2. N = 3, n ≥ 406 for each condition. Brown-Forsythe and Welch ANOVA tests with Games-Howell's multiple comparisons test. Analysis of the same dataset as in (E), excluding neurons without neurites. Data are presented as boxplots.

See also Figures S2 and S3.

ns = nonsignificant.

(Figures 3D–3F). Of note, neurons overexpressing the mutant control Nedd1-F75A polarized at a slightly faster rate at DIV2 (Figure 3E). At DIV5, dendritic length, Map2 distribution, number, and branching of Nedd1-rCM1 overexpressing neurons were indistinguishable from Nedd1-F75A control neurons; only axon length was slightly decreased (Figures S2A and S2B). Nedd1-rCM1 overexpressing neurons acquired a single axon, as did control neurons (Figures S2A and S2B).

To independently validate our results, we exploited the recently characterized MT-nucleating activity of the novel centrosomal protein Akna, which is developmentally downregulated in neurons.[67] Indeed, Akna overexpression increased levels of centrosomal γ-tubulin (Figures 4A, S4C, and S4D) and centrosomal MT nucleation by 1.5- and 3.2-fold at DIV1 and DIV5, respectively (Figures 4B and 4C; Video S4). In fact, at DIV5, Akna-overexpressing neurons exhibited centrosomal MTOC activity similar to control neurons at DIV1.

Yet, despite enhanced centrosomal nucleating activity, Akna-overexpressing neurons showed no difference in polarization speed, and the length of their longest neurites at DIV2 was only marginally increased (Figures 4D–4G). Collectively, our data indicate that the downregulation of centrosomal MT nucleation is not required for the polarization of cultured neurons. This begs the question—could it play a role in radial migration?

Fine-tuned centrosomal MT nucleation is necessary for radial migration but dispensable for neuronal polarization *in vivo*

To probe for a potential role of centrosomal MT nucleation in radial migration, we first investigated the distribution of centrosomal γ-tubulin during cortical development (Figure 5A). Immunohistochemistry in mouse E16 cortices showed a drastic decrease in γ-tubulin-positive centrosomes at the IZ and CP when compared with VZ (Figures 5B–5D). A similar decrease also occurred at later developmental stages when more neurons assembled at the CP. At both E18 and P2, the CP contained fewer γ-tubulin-positive centrosomes than the VZ and SVZ (Figures 5B–5D). However, immunoblotting of biochemical extracts from E17 microdissected VZ/SVZ and CP revealed that the γ-tubulin protein level remained constant between these zones (Figures 5E and 5F). Consistently, bioinformatic analysis of an RNA sequencing (RNA-seq) dataset of the developing mouse cortex at E14.5[68] showed that expression of genes encoding γ-TuRC components, which drive microtubule nucleation, including Tubg1, Tubgcp2, Tubgcp3, Tubgcp4, Tubgcp5, and Tubgcp6,[47] is decreased in neurons only mildly or remains unchanged compared with their progenitors (Table S1). In contrast, the factor that targets γ-TuRCs to the centrosome, Nedd1, is markedly transcriptionally downregulated in neurons (Table S1). This argues that the decrease of γ-tubulin-positive centrosomes in maturing neurons is driven by the delocalization of γ-TuRCs from the centrosome. Collectively, our findings are consistent with the possibility that fine-tuned centrosomal MT nucleation is important for radial migration.

We therefore investigated whether centrosomal MT nucleation has distinct roles in neuronal migration and polarization by manipulating centrosomal MT nucleation with our established molecular tools *in vivo*. To this end, we developed a genetic

expression system that enabled neuron-specific overexpression of a protein of interest (POI), together with a conditional fluorescent reporter (Figure S5A). In short, a plasmid expression system was generated that included a GFP-based Cre-dependent reporter and a POI expression vector, where a lox-flanked autonomous tubulin-α-1 promoter (Tα1)-driven neuron-specific[69–71] iCre expression element acts as a STOP cassette in non-neuronal cells, preventing expression of the POI before neuronal differentiation (Figure S5A). Upon neuronal differentiation, the cassette drives iCre expression and self-excises, enabling the expression of the selected POI and an accompanying GFP reporter (Figure S5A). Thereby, only neurons express the POI and the reporter. Accordingly, we found that 95% of the fluorescent cells were positive for the neuronal nuclei marker NeuN but negative for the proliferation marker Ki-67 (Figures S5B and S5C). As a control, we prepared a plasmid driving neuron-specific expression of the integrase Dre and a Dre-dependent/Cre-inactivated RFP-based reporter, inducing expression of RFP in control neurons while avoiding crosstalk between the expression and control systems (Figure S5A). Hence, we delivered either the expression system including a GFP (*Zoanthus* sp. [Zs] Green)-based recombination reporter or the control system containing a turbo-(t)RFP-based reporter in each ventricle of the brains of E14 embryos via bilateral *in utero* electroporation (IUE), followed by analysis of these brains at E18 (Figure S5A).

This system was implemented to investigate the role of the centrosome in neuronal polarization and migration simultaneously *in vivo*. First, we impaired centrosomal MT nucleation *in vivo* by performing neuron-specific overexpression of N-gTBD + C-CTD; however, this resulted in increased cell death (Figure S5D). We therefore overexpressed N-gTBD alone, which impaired centrosomal MT nucleation equally well (Figures 1H and 1I) without affecting cell viability (Figure S5E).

We also assayed MT nucleation in cortical slices by *in utero* electroporating plasmids encoding EB3-mNeonGreen and Centrin1-mNeonGreen at E14. As the stationary centrosome contrasts with the moving EB3 comets, it allows the use of the same fluorescent protein for both markers. Consistent with our cell culture analysis, manual tracking of EB3 comets showed that centrosomal MT nucleation was also abrogated in N-gTBD-overexpressing neurons in acute cortical slice culture (Figures S6A and S6B; Video S5).

Strikingly, N-gTBD-overexpressing neurons failed to migrate radially toward the CP, contrasting the migration of control tRFP-overexpressing neurons to outer cortical layers (Figures 6A–6C). Importantly, N-gTBD-overexpressing neurons still polarized (Figure 6A). Specifically, N-gTBD-overexpressing neurons formed axons that coursed in a trajectory similar to that of control transfected neurons (Figure 6A). We found a mild reduction in axon bundle density (Figure 6D), which disappeared by postnatal day 2 (P2); yet impaired migration persisted (Figures S7A–S7C). Whole tissue-cleared cortices were imaged using two-photon microscopy, revealing that N-gTBD-expressing neurons have axonal morphologies and trajectories indistinguishable from control cells (Figures 6E–6G; Video S6). Following individual neurons that stalled their migration directly showed that their axons entered the callosal axonal bundle (Video S7). Live imaging of cells in acute slice cultures of the
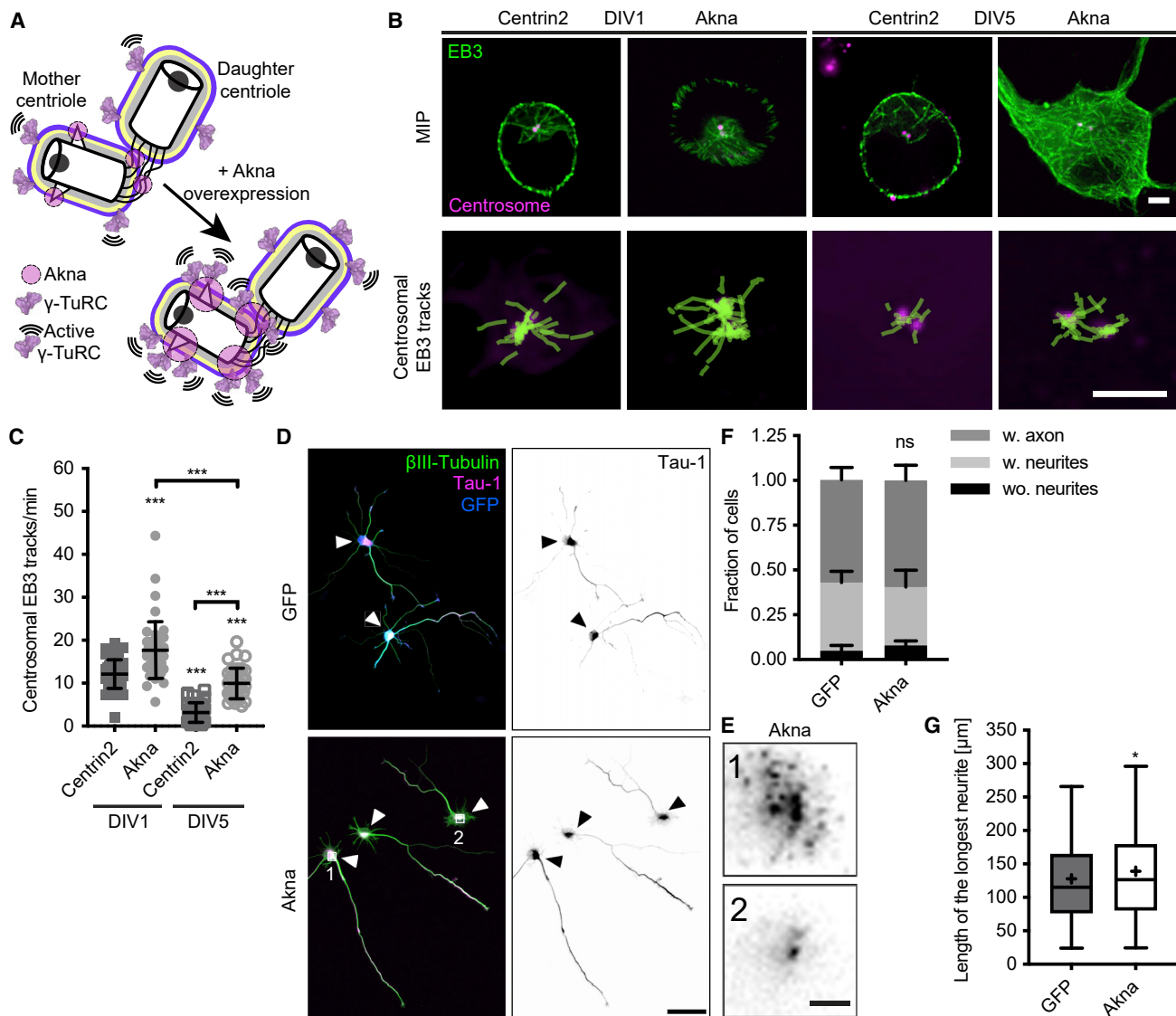
Figure 4. Akna overexpression induces centrosomal MT nucleation without hindering neuronal polarization

(A) A schematic of Akna function.

(B) Representative examples of EB3 tracks in DIV1 and DIV5 rat hippocampal neurons. MIPs of the first 60 frames from videos and detected centrosomal EB3 tracks (green) in whole 3-min videos in the same cells. Scale bars, 3 μm.

(C) Quantification of centrosomal EB3 tracks per minute. N = 3 for all conditions. DIV1: Centrin2, n = 45 cells; Akna, n = 44. DIV5: Centrin2, n = 36; Akna, n = 36. ***p < 0.0001. GLM with Poisson distribution and simultaneous tests for GLM (R multcomp package). Data are presented as mean ± SD. See also Video S4.

(D) Representative images of rat neurons overexpressing indicated constructs at DIV2. Images are a combination of tiles. Scale bar, 50 μm.

(E) Magnified insets of Akna channel showing Akna speckles in high expressing neurons and clear centrosomal localization of Akna in low-expressing neurons. Scale bar 3 μm.

(F) Fractions of rat neurons in developmental stages at DIV2 with (w.) axons or neurites or without (wo.) them. N = 4, n ≥ 596 for each condition; ns, nonsignificant. Ordinal logistic regression model. Data are presented as mean ± SD.

(G) Length of the longest neurite at DIV2. N = 4, n ≥ 552 for each condition; *p = 0.0162. Unpaired Welch's t test. Analysis of the same dataset as in (F), excluding neurons without neurites. Data are presented as boxplots.

cortex revealed that few N-gTBD-expressing neurons migrated radially compared with control neurons during the observation period (Figures 6H–6L; Video S8). The migration speed and directionality of N-gTBD-overexpressing neurons were decreased (Figures 6M–6O); lateral movements, however, were not affected (Figures 6I and 6L; Video S8). The migration of

N-gTBD-expressing neurons was blocked in the IZ (Figure 6C). Concomitantly, N-gTBD-expressing neurons showed a 2-fold increase in multipolar morphology compared with control neurons, independent of axon formation, and a corresponding decrease in bipolar neurons reaching the CP (Figure 6J). Intriguingly, despite defective radial migration, N-gTBD-overexpressing
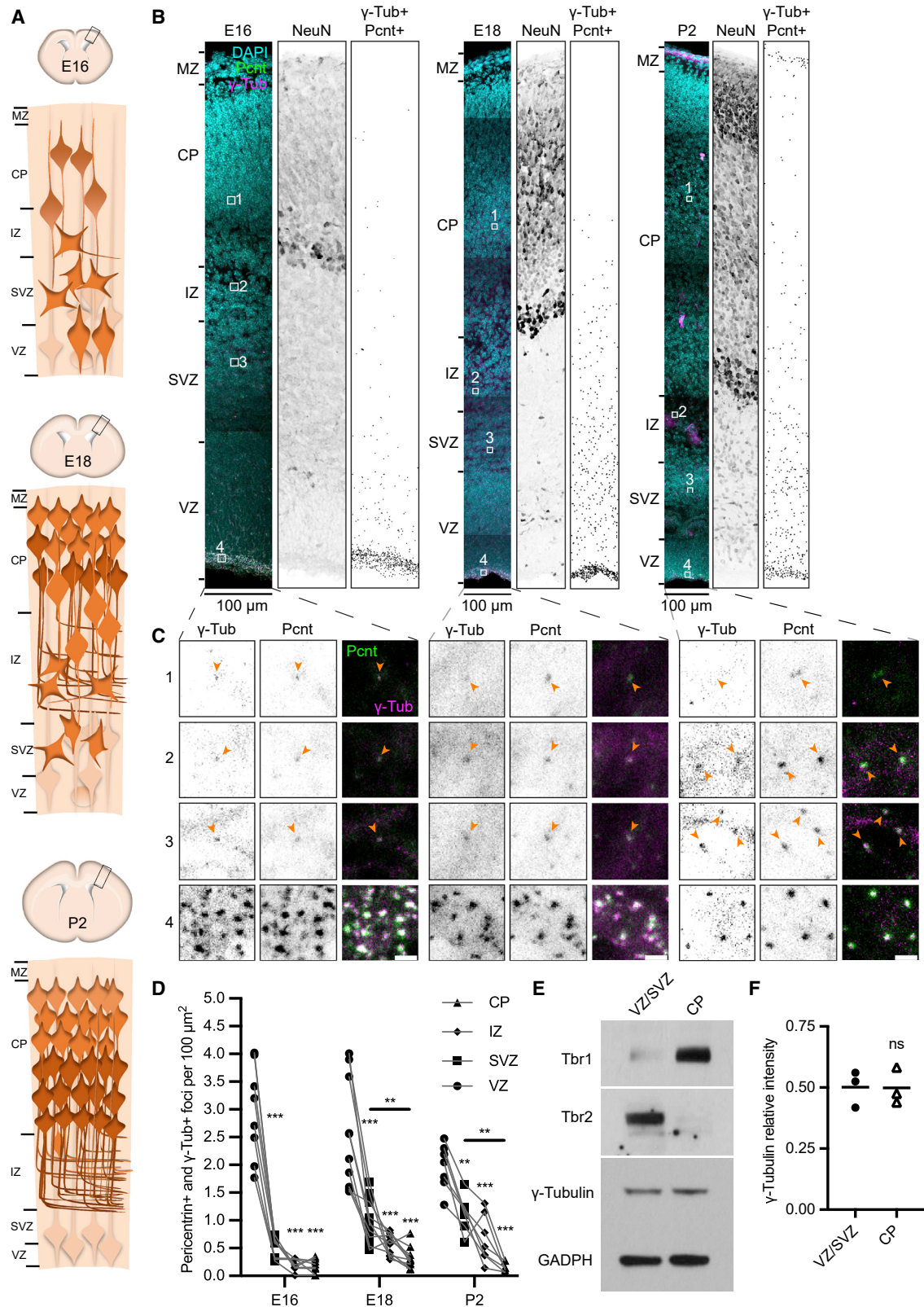
neurons formed axons equivalently to control neurons (Figures 6I and 6K; Video S8).

Although our data show that centrosomal MT nucleation is important for radial migration, we further asked—does counteracting physiological processes of centrosome MTOC deactivation in maturing neurons via enhanced centrosomal MT nucleation also influence radial migration? To do so, we employed our newly developed genetic system to overexpress either Nedd1-rCM1 or Akna in vivo. Overexpression of these constructs did not affect cell viability (Figures S5F and S5G). However, neurons expressing either construct showed defective neuronal migration by E18 (Figures 7A–7E; Camargo Ortega et al.[67]), remaining detectable at P2 (Figures S7D–S7H). Axon formation was not impaired (Figures 7A–7F and S7D–S7I; Video S7), although centrosomal MT nucleation was upregulated, as shown by Akna overexpression ex vivo (Figures S6A and S6B; Video S5).

Interestingly, downregulation of Golgi-mediated MT nucleation by Akap9-dis in vivo did not lead to migratory deficits (Figures S3I and S3J). However, consistent with the reduction of Golgi-mediated MT nucleation impacting axon growth in vitro (Figures S2C, S2D, and S3H), we found that the thickness of the callosal axonal bundle was reduced (Figures S3I–S3K).

The migratory blockade was also present when we followed the embryonic brains electroporated with N-gTBD- or Akna-expressing vectors at earlier (E13→E16) or later (E15→E18) developmental time frames (Figures S6C–S6F). Notably, we found that N-gTBD- or Akna-overexpressing neurons were positive for Map2 in vivo, similar to control neurons, further corroborating our finding that centrosomal dysregulation does not markedly perturb neuronal polarization (Figures S8A and S8B). Moreover, both stalled and migrating N-gTBD- or Akna-overexpressing neurons were positive for the upper cortical layer marker Satb2 but negative for the deep cortical layer markers Tbr1 and Ctip2, as was the case for control neurons (Figures S8C–S8H). This suggests that manipulation of centrosomal MT nucleation, once the cells acquired neuronal fate, did not influence the acquisition of cortical identity. Taken together, whereas tightly regulated centrosomal MT nucleation is crucial for radial migration, neuronal polarization occurs independently of it.

Neurons migrate radially by the periodic formation of a cytoplasmic dilation, also referred to as "swelling,"[27] in the leading process, which the centrosome invades. The nucleus follows the centrosome through their coupling, completing the locomotion cycle (Figure 8A).[4,5,9,27,43] We studied how our manipulations with centrosomal MT nucleation affected these processes

essential for radial migration. Video-microscopic analysis in cortical slices expressing Centrin1-mNeonGreen and EB3-mNeonGreen (Figure 8B) uncovered a drastic reduction of nuclear movement in N-gTBD- or Akna-overexpressing neurons (Figure 8C; Video S9), consistent with the migratory defects we observed in our previous experiments (Figures 6 and 7; Videos S6, S7, and S8). Strikingly, we found an increased nucleus-centrosome (n-c) distance in N-gTBD-overexpressing neurons, whereas the n-c distance in Akna-overexpressing neurons decreased (Figure 8D). Moreover, although there were no differences in the diameter of the cytoplasmic dilation (Figure 8E), we found changes in its dynamics—in N-gTBD-overexpressing neurons, the cytoplasmic dilation formed twice as often as in control neurons (Figures 8B and 8F). In contrast, the cytoplasmic dilation hardly occured in Akna-expressing neurons (Figures 8B and 8F). Thus, this inability to timely and periodically disassemble and reassemble the cytoplasmic dilation, together with changes in n-c coupling, can contribute to the observed migratory block.

The migratory block presented here is similar to that observed upon dysregulation of the Reelin-Ras-related protein 1 (Rap1)-N-Cadherin (NCad) pathway.[72,73] Trafficking of the adhesion protein NCad is crucial for neuronal migration[72,74,75] including multipolar-to-bipolar transition,[73] and depends on endocytic pathways,[76] which in turn rely on MTs.[77] Endocytic pathways are also influenced by direct interactions of vesicles with the centrosome, even in the absence of MTs.[78,79] Therefore, we hypothesized that the migratory block might be related to dysregulated trafficking of NCad. In addition, the migratory block might be related to the misbalance between centrosomal and acentrosomal microtubule networks.[39–41] Indeed, dysregulation of Calmodulin-regulated spectrin-associated protein (Camsap) family proteins leads to migratory phenotypes.[80–82] It is worth noting in this context that Akna interacts with Camsap3 and can recruit it to the centrosome.[67]

We therefore finally tested the possibility that Akna-induced impairment of migration could be restored by overexpressing NCad or CAMSAP3. To this end, we overexpressed Akna together with NCad or CAMSAP3 using our IUE approach at E14. We found that both proteins were able to mitigate the migration defect elicited by Akna expression. Compared with Akna-overexpressing neurons, both Akna plus NCad or Akna plus CAMSAP3-overexpressing neurons were decreased by one-third in the IZ, instead reaching the CP more frequently (Figures 8G and 8H).

To conclude, a tight balance between centrosomal and acentrosomal MT networks and downstream regulation of cell

Figure 5. γ-Tubulin positive centrosomes abundance decreases as neurons migrate radially through the layers of the developing neocortex
(A) A schematic of cortical development.
(B) MIPs of automated tile scanning of coronal sections from E16, E18, and P2 mouse brains with indicated cortical layers. Left, γ-tubulin (γ-Tub), Pericentrin (Pcnt), and cell nuclei (DAPI) staining. Middle, NeuN staining shown separately. Right, center of mass of centrosomes, foci positive for both γ-tub (γ-Tub+) and Pcnt (Pcnt+), detected using Imaris surface function (see method details); represented as black squares. In some cases, tiled images were rotated using Fiji to enable preparation of 100-μm broad slices spanning all cortical layers or errors in tile stitching were corrected using MosaicJ (Fiji).
(C) Representative MIPs of the cortical areas indicated by numbered white squares in the left panels in (B). Left, E16; middle, E18; right, P2. Scale bars, 3 μm.
(D) Quantification of abundance of γ-tub+ and Pcnt+ centrosomes in cortical layers (B, right). E16, n = 8; E18, n = 10; P2, n = 7. Two-way ANOVA with Tukey's multiple comparisons test, ***p < 0.0001, **p < 0.01. All datapoints shown. n, number of independent brains.
(E) Western blot of samples of VZ/SVZ and CP regions of the E18 mouse cortex. Tbr2 marks dividing neuronal progenitors that are abundant in the germinal zone (VZ/SVZ) of the cortex. Tbr1 is a neuronal marker enriched in the CP. GAPDH was used as a loading control.
(F) Quantification of γ-tubulin relative signal intensity in (E). Welch's t test; ns = nonsignificant.
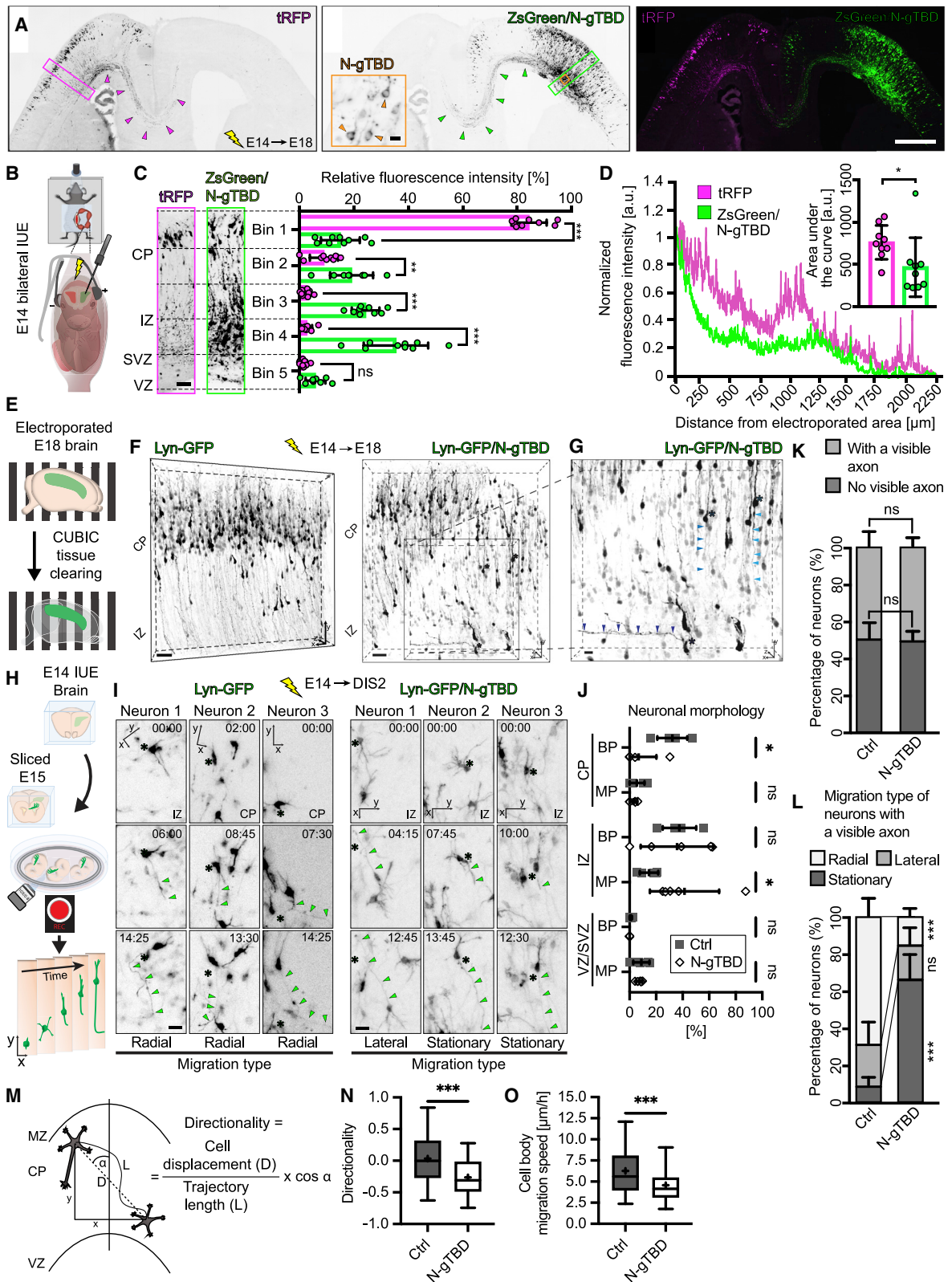
adhesion and signaling molecules, including NCad, is indispensable for proper neuronal migration. However, for axon formation and growth, MT generation at the centrosome is not required.

DISCUSSION

Here, we have found that radial migration and neuronal polarization—two closely interwoven processes—are mechanistically separable through their distinct dependency on centrosomal MT nucleation. Our work provides an insight into how complex neuronal morphology can be achieved and how parallel motility events within the same cell can be separately controlled.

Molecular insights into the neuronal centrosome

Our molecular tools manipulating the centrosomal MTOC shed light on the composition of the neuronal centrosome. Similar to non-neuronal centrosomes,[53] the neuronal centrosome contains a pool of γ-tubulin during early neuronal development, dependent on Cdk5rap2. In contrast to non-neuronal cells,[52,53,56] however, Cdk5rap2 fails to activate centrosomal γ-TuRC in neurons. This indicates that other activators exist in neurons. A promising candidate for this is Akna, a recently described centrosomal protein that activates centrosomal MT nucleation[67] and is present in nascent neurons. Indeed, we found in maturing neurons that Akna overexpression increases centrosomal MT nucleation to the level of nascent neurons. This was accompanied by a small increase in centrosomal γ-tubulin levels that remained below the level found in nascent neurons. This suggests that it is the activation of centrosomal γ-TuRCs, and not their amount, that is rate limiting for centrosomal MT nucleation.

This view is further supported by our finding that overexpression of Nedd1 decreases centrosomal γ-tubulin levels without affecting centrosomal MT nucleation. Our FRAP experiments revealed that Nedd1 centrosomal turnover is higher than that of γ-tubulin, in agreement with proteomic experiments.[83] Exogenous Nedd1 increased γ-tubulin recovery at the centrosome while simultaneously shifting the steady state between centrosomal and cytoplasmic γ-tubulin to the cytoplasm. This raises the possibility that, as observed in keratinocytes,[53] Nedd1 in neurons influences the more mobile centrosomal γ-TuRC pool, which is not in direct contact with its activators and therefore does not contribute to MT nucleation. This increase in γ-tubulin exchange could compensate for the partial relocation of centrosomal γ-TuRCs to the cytoplasm. In contrast, cytoplasmic N-gTBD, which fails to shuttle γ-TuRC to the centrosome,[55] depletes centrosomal γ-TuRCs from both inactive and active pools, leading to impairment of centrosomal MT nucleation.

Taken together, our data indicate that the neuronal centrosome contains distinct pools of γ-TuRCs with differential activity. Because Akna and Nedd1-CM1 both activated centrosomal MT nucleation, albeit with varying γ-tubulin centrosomal levels, we propose that activation is key for γ-TuRC-mediated centrosomal MT nucleation. This view is further supported by other studies showing the necessity of γ-TuRC activation.[47,52,53,67,84–86]
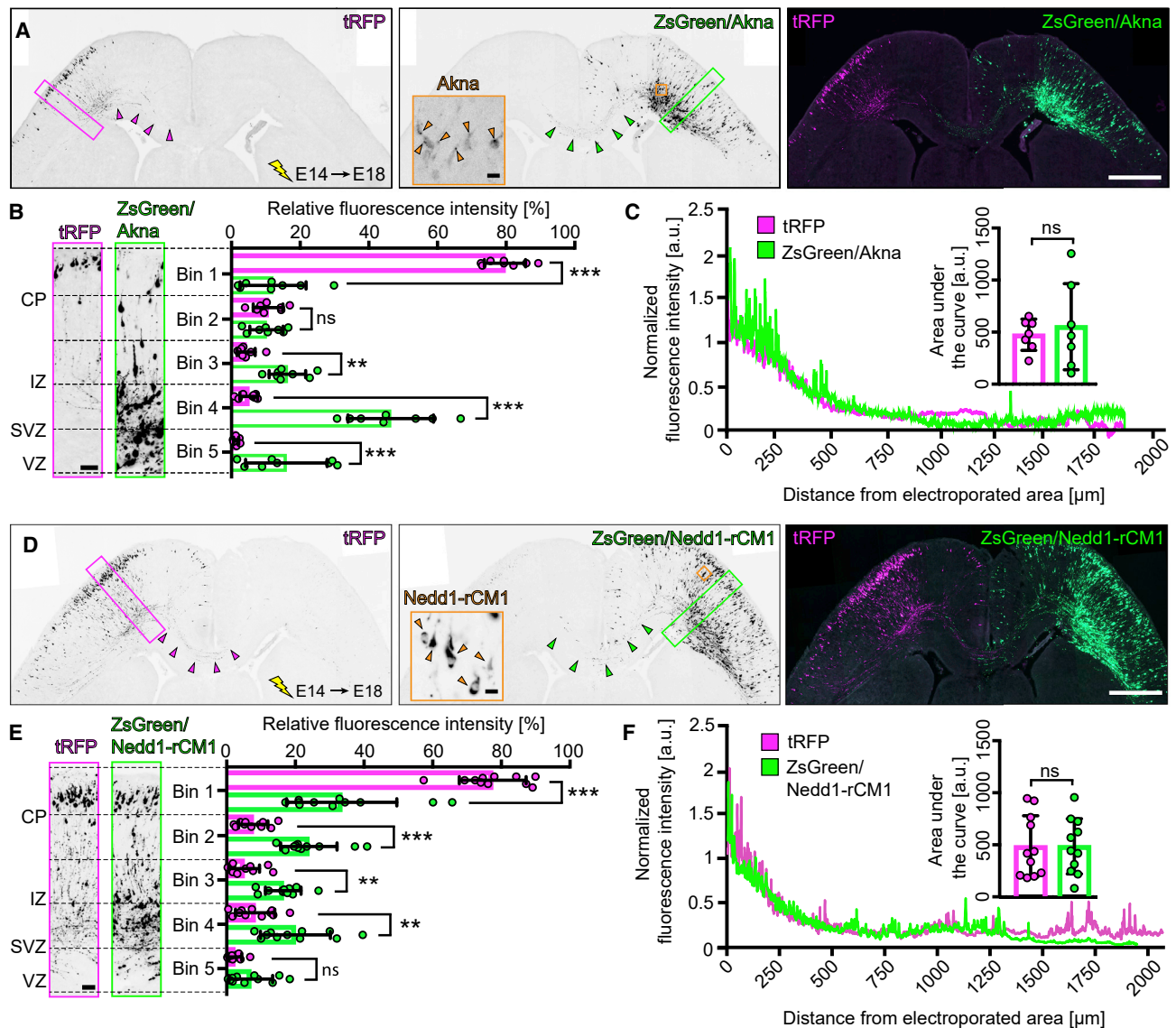
Centrosomal MT nucleation: Neuronal migration versus axon formation

Because the physiological downregulation of the centrosomal MT nucleation is common to neuronal and non-neuronal differentiating cells,[25,53,64,87,88] it was tempting to speculate that this process is necessary to facilitate neuronal differentiation. However, we found that the downregulation of the centrosomal MT nucleation is neither required for neuronal polarization in cell culture nor *in vivo*. Our data thus indicate that axon formation and

---

Figure 6. Radial migration but not polarization depends on centrosomal MT nucleation in vivo

(A) Automated tile scanning of coronal sections from E18 mouse brains bilaterally electroporated *in utero* at E14 showing control tRFP-transfected neurons (left, magenta) and ZsGreen/N-gTBD-overexpressing neurons (middle, green). Arrowheads indicate axons navigating the axon bundle within the IZ. Scale bar, 500 μm. Middle panel, a magnification inset corresponding to the orange-outlined area shows N-gTBD overexpression levels in ZsGreen/N-gTBD-electroporated neurons. Scale bar, 10 μm.

(B) A schematic of bilateral IUE.

(C) Quantification of (A). Left, magnifications depicting the distribution of neurons in the different cortical compartments, determined by DAPI stain, corresponding to the magenta and green areas outlined in (A). Scale bar, 50 μm. Right, average fraction of neurons distributed in the indicated cortical compartments. n = 9[#]; ***p < 0.001; **p < 0.01. Two-way ANOVA with Šídák's multiple comparisons test.

(D) Quantification of (A). The magenta (tRFP) and green (ZsGreen/NgTBD) curves represent the average density of axons along the IZ as extending from the electroporated region. The bar plot indicates the average area under the curves. n = 9[#]; **p = 0.0078. Ratio paired t test.

(E) A schematic of a brain clearing experiment.

(F) 3D reconstruction of 2-photon tile scans of cleared E18 mouse brains electroporated at E14 with a Lyn-GFP control (left) or Lyn-GFP/N-gTBD mix (middle). Scale bar, 50 μm.

(G) 3D magnification of frame in middle (F). Matching color-coded asterisks and arrowheads indicate neurons overexpressing N-gTBD and their axons, respectively. Magnification scale bar, 20 μm.

(H) A schematic of the IUE and *in situ* time-lapse experiment.

(I) Representative time-lapse frames of three independent neurons overexpressing either Lyn-GFP (left) or a Lyn-GFP/N-gTBD mix (right) from mouse brains electroporated at E14 and analyzed two days later *in situ* (DIS). Asterisks depict the initial position of the neuronal soma and arrowheads indicate the progression of the extending axons. Scale bar, 20 μm.

(J–O) Quantification of (I). Morphology, bipolar (BP) versus multipolar (MP; including neurons with the axon), of N-gTBD-overexpressing neurons in indicated regions of the developing cortex compared with control (J), Lyn-GFP (Ctrl), N = 5; N-gTBD, N = 5. *p < 0.0206; with or without axon (K), migratory behavior (L) compared with control, Lyn-GFP (Ctrl), N = 7; N-gTBD, N = 4. ***p < 0.0001. Directionality (M and N) and migration speed (O) of N-gTBD-overexpressing neurons compared with control, N = 7, n ≥ 130, N-gTBD, N = 4, n ≥ 109. ***p < 0.001. Two-way ANOVA with Šídák's multiple comparisons test (J–L), Unpaired Welch's t test (N and O). Values are plotted as mean ± SD or as boxplots (N and O).

ns = nonsignificant

([#]) Each point represents an average of at least 2 consecutive coronal sections per brain. "n" represents a number of independent electroporated brains.

See also Figures S5 and S7 and Videos S6 and S7.

Figure 7. Finely tuned centrosomal MT nucleation is necessary for radial migration but not axon formation *in vivo*

(A) Automated tile scanning of coronal sections from E18 mouse brains bilaterally electroporated *in utero* at E14 showing control tRFP-transfected neurons (left, magenta) and ZsGreen/Akna-overexpressing neurons (middle, green). Arrowheads indicate axons navigating the axon bundle within the IZ. Scale bar, 500 μm. Middle panel, magnification inset corresponding to the orange-outlined area shows Akna overexpression levels in ZsGreen/Akna-electroporated neurons. Scale bar, 10 μm.

(B) Quantification of (A). Left, magnifications depicting the distribution of neurons in the different cortical compartments, determined by DAPI stain, corresponding to the magenta and green areas outlined in (A). Scale bar, 50 μm. Right, average fraction of neurons distributed in the indicated cortical compartments. n = 8[#]; ***p < 0.001; **p < 0.01. Two-way ANOVA with Šídák's multiple comparisons test.

(C) Quantification of (A). The magenta (control) and green (ZsGreen/Akna) curves represent the average density of axons along the IZ as extending from the electroporated region. The bar plot indicates the average area under the curves. n = 7[#]. Ratio paired t test.

(D) Automated tile scanning of coronal sections from E18 mouse brains bilaterally electroporated *in utero* at E14 showing control tRFP-transfected neurons (left, magenta) and ZsGreen/Nedd1-rCM1 overexpressing neurons (middle, green). Arrowheads indicate axons navigating the axon bundle within the IZ. Scale bar, 500 μm. Middle panel, magnification inset corresponding to the orange-outlined area shows Nedd1-rCM1 overexpression levels in ZsGreen/Nedd1-rCM1-electroporated neurons. Scale bar, 10 μm.

(E) Quantification of (D). Left, magnifications depicting the distribution of neurons in the different cortical compartments corresponding to the magenta and green areas outlined in (D). Scale bar, 50 μm. Right, average percentage distribution of neurons in the different cortical compartments. n = 11[#]; ***p < 0.001; **p < 0.01. Two-way ANOVA with Šídák's multiple comparisons test.

(legend continued on next page)

early growth *in vivo* are governed by acentrosomal MT networks. This view is supported by our finding that Golgi-mediated MT nucleation facilitates axon growth. Furthermore, recent findings implicated acentrosomal MT nucleation[64,89] and the MT minus-end regulators Camsaps in the regulation of axonogenesis.[81,82,90]

The symmetry break in differentiating multipolar neurons is controlled by signaling pathways, including phosphatidylinositol (3,4,5)-trisphosphate (PIP3) signaling, synapses of the amphid defective (SAD) kinase, or liver kinase B1 (LKB1)-regulated pathways.[91–95] As these pathways are upstream of MT dynamics,[96,97] these data are consistent with our findings that centrosomal MT nucleation is not involved in the establishment of neuronal polarity. But could centrosomal MT nucleation be involved in the maintenance of neuronal polarity? This seems unlikely as the centrosome becomes inactivated as a MTOC at later developmental stages.[25,64,98,99]

Remarkably, regenerating neurons are thought to lose their cell identity and de-differentiate.[100] In fact, the program of regeneration is regarded as a reactivation of a developmental program.[101] Therefore, we cannot exclude the possibility that regenerating neurons, where microtubules play a key role,[102–105] may reactivate the centrosome. Future studies will need to decipher the role of centrosomal and acentrosomal MT nucleation during axon regeneration.

Strikingly, both prolonged and prematurely downregulated centrosomal MT nucleation disrupted neuronal radial migration. We found that centrosomal dysregulation in neurons manifests as multipolar-to-bipolar transition and locomotion problems, in line with our previous findings.[67] Interestingly, dysregulation of neuronal polarity can negatively influence neuronal migration. Events as molecularly diverse as precocious dendritic differentiation by overexpression of actin network upstream regulator Nck-associated protein 1 (Nap1),[106] deregulated RhoA activity,[107] or impairment of the single axon formation program through Camsap1 downregulation[80] converge on blocking the acquisition and consolidation of neuronal bipolar morphology. However, not all perturbations of neuronal polarity lead to a migratory block, as we show that impairment of Golgi-MT nucleation has an impact on neuronal morphology but not on radial migration.

When we manipulated centrosomal microtubule nucleation, neuronal identity and neuronal polarization were virtually unperturbed. However, we would like to point out that processes of later neuronal development remain to be studied, including late axon guidance and arborization. It was recently shown that γ-TuRC is involved in ciliary resorption pathways.[108] Because primary cilia signaling promotes axonal tract development,[22,109] an excess of centrosomal γ-TuRC might perturb these pathways. Thus, the physiological downregulation of centrosomal γ-TuRC, which we and others have observed,[25,64,67,98,99] might

also be relevant in this context. Collectively, our data reveal the existence of independent neuronal programs for migration and polarization that share regulatory pathways and effectors.[4–6,8,11,12,14,110–112]

Decrease and increase of centrosomal microtubule nucleation differentially affect the key migratory structure, the cytoplasmic dilation, periodically forming in the leading process of locomoting projection neurons.[5,27,43] The cytoplasmic dilation is enriched in dynein[27] and the centrosome is repeatedly moving toward it during glial-guided locomotion.[5,27] The centrosomal movement toward dilation depends on the lissencephaly-1 protein (Lis1) and dynein but is independent of actomyosin.[27] Many dynein regulators, essential for neuronal migration, including Lis1 or nuclear distribution protein nudE-like 1 (Ndel1), localize to the centrosome.[43,113] In fact, dysregulation of Lis1[27,43,114] and dynein subunits[27,115] leads to migratory deficits similar to the ones described here. It is plausible that transmission of force generated by molecular motors through centrosomally attached MTs is crucial for radial movement of both the centrosome and the nucleus; a misbalance between opposing forces of molecular motors acting on abnormal MT networks is implied in neuronal migration disorders[4,9]

Consistently, a defect of neuronal migration was reported upon reduction of γ-tubulin centrosomal levels after depletion of the PCM protein, serologically defined colon cancer antigen 8 (SDCCAG8), associated with ciliopathies and schizophrenia.[44] Moreover, mutations in *TUBG1* cause neuronal migration disorders.[116,117] Conversely, loss of phosphorylated centrosomal Cdk5 in Cep85L-depleted neurons leads to abnormal accumulation of Lis1, nuclear distribution protein nudE homolog 1 (Nde1), dynein, and MT depolymerizing kinesin KIF2A at the centrosome.[18] This results in increased centrosomal MT density and anchoring at the mother centriole and subsequent neuronal migration impairment. To complete the circle, formation of the cytoplasmic dilation is governed by Cdk5 and depends on both MTs and endocytic recycling.[118] Because MT nucleation and anchoring are intertwined processes,[119] it is likely that some level of centrosomal MT nucleation is required for centrosomal MT anchoring, as observed in radially migrating neurons.[27,43] Thus, finely tuned centrosomal MT nucleation is necessary for radial migration.

Therefore, we investigated its role in the centrosome-related migratory block. Remarkably, NCad cell surface exposure negatively correlates with centrosomal MT nucleation during the neuronal development.[72,120,121] First, increased centrosomal MT nucleation leads to NCad internalization and neuronal delamination.[120,121] It is tempting to speculate that Akna plays a direct or indirect role in NCad internalization because Akna redistributes Camsap3 from adherens junctions to the centrosome.[67] Later, Reelin-induced increase of NCad on the cell surface is required for neuronal orientation toward the CP


(F) Quantification of (D). The magenta (control) and green (ZsGreen/Nedd1-rCM1) curves represent the average density of axons along the IZ as extending from the electroporated region. The bar plot indicates the average area under the curves. n = 11#. Ratio paired t test.

(#) Each point represents the average of at least 2 consecutive coronal sections per brain. n, number of independent bilaterally electroporated brains. Values are plotted as mean ± SD.

ns = nonsignificant

See also Video S7.
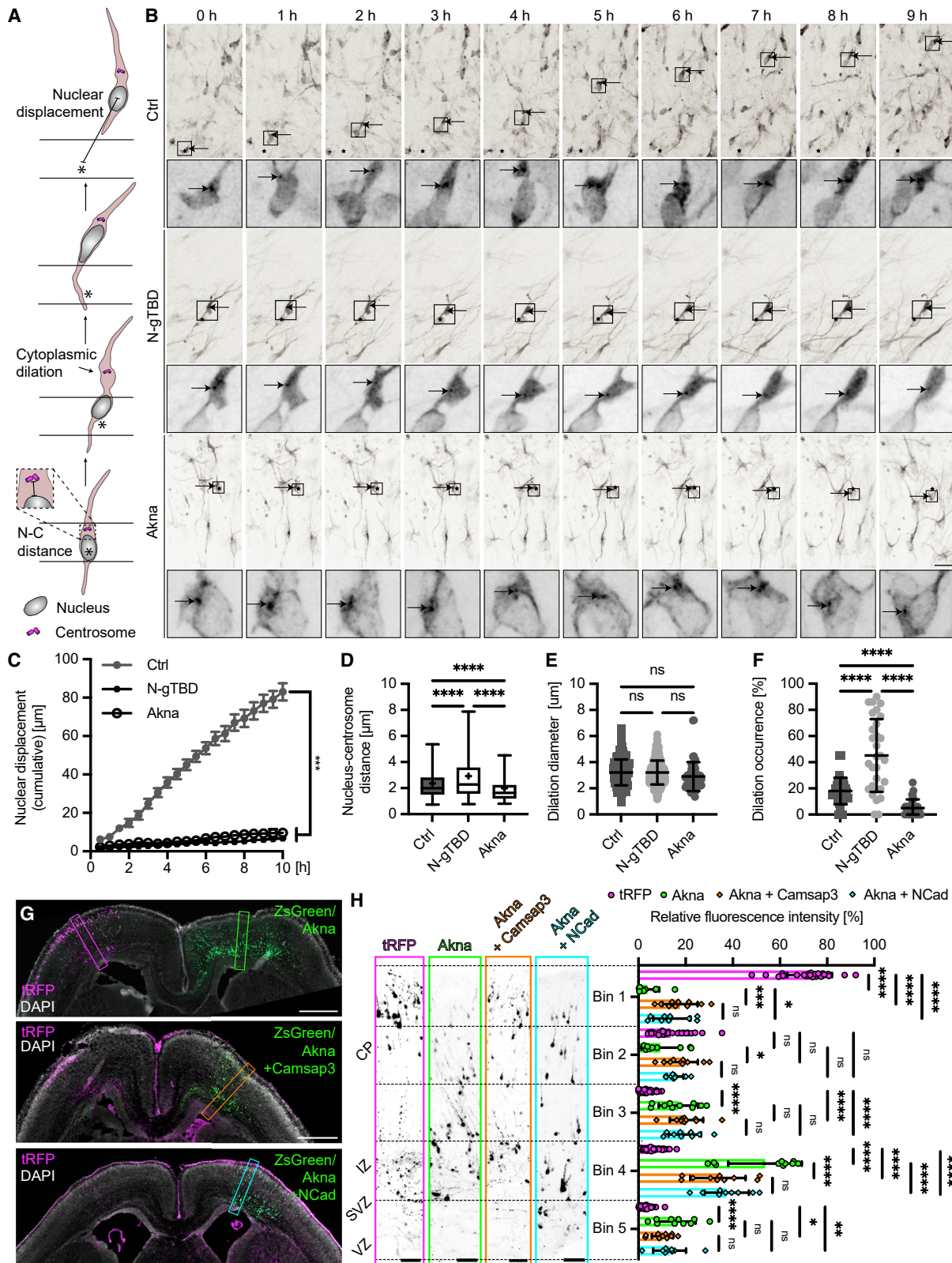
(legend on next page)

and for multipolar-to-bipolar transition.[72] This occurs in the IZ, where we found that centrosomal γ-tubulin levels are already decreased.

The migratory block induced by Akna overexpression was partially overcome by co-expression of either NCad or Camsap3. Thus, we show that the balance between centrosomal and acentrosomal MT networks and normal NCad trafficking are crucial for several milestones of neuronal migration, including multipolar-to-bipolar transition, cytoplasmic dilation formation, and locomotion of cortical projection neurons. In this context, it is noteworthy that cortical neurons polarize and form an axon even in the absence of adhesion sites in 3D cultures.[122] This raises the possibility that two distinct growth mechanisms occur simultaneously in the same cell through the distinct centrosomal and acentrosomal MT networks.

From this perspective, it is interesting to note that centriole depletion in *Sas4/p53* double knockout (KO) mice, which does not perturb the formation of the neocortex, induces the generation of ectopically placed cortical neurons.[45] Centrosome loss was not complete in these mice, with approximately half of Pericentrin or Arl13b-positive structures present in *Sas4* KO cortices at E15.5.[45] This supports the possibility of centrosomal regulation of neuronal migration. Clearly, there are also non-cell-autonomous factors that influence neuronal migration[1] and these may partially compensate for the reduction of centrioles in *Sas4/p53* KO neocortex.

Developmental cortical defects: Differential impact on radial migration and polarization

The lissencephaly spectrum of cortical developmental malformations, including cortical agyria, pachygyria, and subcortical band heterotopia, is characterized by mispositioned neurons.[4] Intellectual disabilities, epileptic seizures, and underlying pachygyria or even agyria in patients with rare *TUBG1* mutations[117,123–125] are associated with neuronal migratory deficits, as confirmed experimentally in mice.[116,117] Remarkably, the cortical malformations are accompanied by modest or no defects to axon tracts, including the corpus callosum.[124] In light of our data, this phenomenon can be explained by the distinct regulation of radial migration and neuronal polarization.

As the majority of patients also exhibit microcephaly, it is likely that *TUBG1* mutants impair centrosomal MT nucleation during mitosis of neuronal progenitors.[123] Indeed, two human *TUBG1* disease variants misplace the mitotic spindle when expressed in yeasts.[117] Furthermore, *TUBG1* mutants have a reduced ability to form γ-TuRC.[116] Because the centrosomes of migrating cortical neurons are active,[27] they may be involved in the migratory phenotypes of *TUBG1* variants. Clearly, we cannot exclude that acentrosomal γ-tubulin-dependent MT nucleation pathways also contribute to neuronal migration. In addition, acentrosomal γ-tubulin complexes are involved in axon growth,[64,89] which may explain minor and less frequent axonal phenotypes in patients suffering from mutations in *TUBG1*.[124] In this context, it is interesting to note that tubulinopathies, which affect both the centrosomal and acentrosomal MT network, cause axonal tract defects,[126,127] thereby contrasting with γ-tubulinopathies.[123,124] Taken together, our finding that radial migration depends on a centrosomal MT network that is dispensable for neuronal polarization helps to define specific molecular steps that must be manipulated to overcome the defects of these developmental disorders.

Conclusions

Centrosomal MT nucleation distinguishes radial migration from axon formation. In essence, radial migration and neuronal polarization are similar dynamic processes that also share cytoskeletal effectors. The defining difference, however, is that axon outgrowth occurs without dragging the nucleus and cell soma in the growth direction. The nucleokinesis associated with migratory locomotion needs a fine-tuned centrosomal microtubule network, which is not required for axon formation and growth.

STAR★METHODS

Detailed methods are provided in the online version of this paper and include the following:

- KEY RESOURCES TABLE
- RESOURCE AVAILABILITY
  - Lead contact

Figure 8. Centrosomal microtubule nucleation correlates with cytoplasmic dilation occurrence and its dysregulation can be partially overcome by Camsap3 or NCad overexpression

(A) A schematic of the nucleus-centrosome coupling and cytoplasmic dilation formation during neuronal locomotion.

(B) Representative time-lapse frames of mouse neurons overexpressing either mOrange2 (Ctrl), mOrange2-N-gTBD, or Akna-mOrange2, together with mNeonGreen-hCentrin1 and EB3-mNeonGreen. The brains were electroporated at E14.5 and sliced after 2 days. The slices were then imaged *in situ* every 30 min in tiled 30- to 50-μm z stacks for 10–15 h. Asterisks depict the initial position of the neuronal soma and arrows indicate the position of the centrosome. Insets highlight pericentrosomal area including the cytoplasmic dilation. Scale bar, 20 μm.

(C–F) Quantification of (B), N = 3. Cumulative displacement of the nucleus, n = 30 cells for each condition (C), nucleus-centrosome (n-c) distance, n = 600 (30 cells times 20 measurements per cell for all conditions; the n-c distance was measured in every frame of each video) (D), diameter of the cytoplasmic dilation in the leading process, mOrange2 (Ctrl), n = 175, N-gTBD, n = 466, Akna, n = 54 (difference in the number of values (n) is caused by variable occurrence of the cytoplasmic dilation during the time-lapse sequence) (E), and frequency of its occurrence, n = 30 for all conditions, in N-gTBD and Akna-overexpressing neurons compared with control (F). ****p < 0.0001, ***p < 0.001, two-way ANOVA with Tukey's multiple comparisons test (C), Brown-Forsythe and Welsh ANOVA with Dunnet's T3 multiple comparisons test (D–F). See also Video S9.

(G) Automated tile scanning of coronal sections from E18 mouse brains bilaterally electroporated *in utero* at E14 showing control tRFP-transfected neurons (left, magenta) and ZsGreen/Akna, ZsGreen/Akna + Camsap3 or ZsGreen/Akna +NCad overexpressing neurons (right, green). Scale bar, 500 μm.

(H) Quantification of (G). Left, magnifications depicting the distribution of neurons in the different cortical compartments, determined by DAPI stain, corresponding to the magenta, green, orange, and cyan areas outlined in (G). Scale bar, 50 μm. Right, average fraction of neurons distributed in the indicated cortical compartments. n ≥ 9#; ****p < 0.0001, ***p < 0.001, **p < 0.01, *p <0.05. Two-way ANOVA with Tukey's multiple comparisons test. ns = nonsignificant. (#) Each point represents an average of at least 2 consecutive coronal sections per brain. "n" represents the number of independent electroporated brains.

SUPPLEMENTAL INFORMATION

Supplemental information can be found online at https://doi.org/10.1016/j.neuron.2023.01.020.

AUTHOR CONTRIBUTIONS

Conceptualization, S.V. and F.B.; methodology, S.V., S.D., M.S., E.A., T.P., S.B., S.F., G.C.O, N.M., and I.M.T.; investigation, S.V., S.D., M.S., E.A., T.P., S.B., S.F., G.C.O, N.M., and I.M.T.; resources, M.G. and F.B.; formal analysis, J.S.; writing original draft, S.V. and F.B.; writing – review & editing, S.V., S.D., T.P., E.A., S.B., M.S., S.F., G.C.O., N.M., I.M.T., J.S., M.G., and F.B.; funding acquisition, M.G. and F.B.; supervision, F.B., M.G., and I.M.T.; supervision of the project, F.B.

DECLARATION OF INTERESTS

The authors declare no competing interests.

REFERENCES

1. Hansen, A.H., and Hippenmeyer, S. (2020). Non-cell-autonomous mechanisms in radial projection neuron migration in the developing cerebral cortex. Front. Cell Dev. Biol. 8, 574382. https://doi.org/10.3389/fcell.2020.574382.

2. Sakakibara, A., Ando, R., Sapir, T., and Tanaka, T. (2013). Microtubule dynamics in neuronal morphogenesis. Open Biol. 3, 130061. https://doi.org/10.1098/rsob.130061.

3. Namba, T., Kibe, Y., Funahashi, Y., Nakamuta, S., Takano, T., Ueno, T., Shimada, A., Kozawa, S., Okamoto, M., Shimoda, Y., et al. (2014). Pioneering axons regulate neuronal polarization in the developing cerebral cortex. Neuron 81, 814–829. https://doi.org/10.1016/j.neuron.2013.12.015.

4. Francis, F., and Cappello, S. (2021). Neuronal migration and disorders – an update. Curr. Opin. Neurobiol. 66, 57–68. https://doi.org/10.1016/j.conb.2020.10.002.

5. Nishimura, Y.V., Nabeshima, Y.-I.I., and Kawauchi, T. (2017). Morphological and molecular basis of cytoplasmic dilation and swelling in cortical migrating neurons. Brain Sci. 7, 1–12. https://doi.org/10.3390/brainsci7070087.

6. Jossin, Y. (2020). Molecular mechanisms of cell polarity in a range of model systems and in migrating neurons. Mol. Cell. Neurosci. 106, 103503. https://doi.org/10.1016/j.mcn.2020.103503.

7. Schelski, M., and Bradke, F. (2017). Neuronal polarization: from spatiotemporal signaling to cytoskeletal dynamics. Mol. Cell. Neurosci. 84, 11–28. https://doi.org/10.1016/j.mcn.2017.03.008.

8. Yogev, S., and Shen, K. (2017). Establishing neuronal polarity with environmental and intrinsic mechanisms. Neuron 96, 638–650. https://doi.org/10.1016/j.neuron.2017.10.021.

9. Gonçalves, J.C., Quintremil, S., Yi, J., and Vallee, R.B. (2020). Nesprin-2 recruitment of BicD2 to the nuclear envelope controls dynein/kinesin-mediated neuronal migration in vivo. Curr. Biol. 30, 3116–3129.e4. https://doi.org/10.1016/j.cub.2020.05.091.

10. Asada, N., and Sanada, K. (2010). LKB1-mediated spatial control of GSK3beta and adenomatous polyposis coli contributes to centrosomal forward movement and neuronal migration in the developing neocortex. J. Neurosci. 30, 8852–8865. https://doi.org/10.1523/JNEUROSCI.6140-09.2010.

11. Coles, C.H., and Bradke, F. (2015). Coordinating neuronal actin–microtubule dynamics. Curr. Biol. 25, R677–R691. https://doi.org/10.1016/j.cub.2015.06.020.

12. Witte, H., Neukirchen, D., and Bradke, F. (2008). Microtubule stabilization specifies initial neuronal polarization. J. Cell Biol. 180, 619–632. https://doi.org/10.1083/jcb.200707042.

13. van Beuningen, S.F.B., Will, L., Harterink, M., Chazeau, A., van Battum, E.Y., Frias, C.P., Franker, M.A.M., Katrukha, E.A., Stucchi, R., Vocking, K., et al. (2015). TRIM46 controls neuronal polarity and axon specification by driving the formation of parallel microtubule arrays. Neuron 88, 1208–1226. https://doi.org/10.1016/j.neuron.2015.11.012.

14. Dupraz, S., Hilton, B.J., Husch, A., Santos, T.E., Coles, C.H., Stern, S., Brakebusch, C., and Bradke, F. (2019). RhoA controls axon extension independent of specification in the developing brain. Curr. Biol. 29, 3874–3886.e9. https://doi.org/10.1016/j.cub.2019.09.040.

15. Bornens, M. (2012). The centrosome in cells and organisms. Science 335, 422–426. https://doi.org/10.1126/science.1209037.

16. Stoufflet, J., Chaulet, M., Doulazmi, M., Fouquet, C., Dubacq, C., Métin, C., Schneider-Maunoury, S., Trembleau, A., Vincent, P., and Caillé, I. (2020). Primary cilium-dependent cAMP/PKA signaling at the

centrosome regulates neuronal migration. Sci. Adv. *6*, 1–11. https://doi.org/10.1126/sciadv.aba3992.

17. Arquint, C., Gabryjonczyk, A.M., and Nigg, E.A. (2014). Centrosomes as signalling centres. Philos. Trans. R. Soc. Lond. B Biol. Sci. *369*, 20130464. https://doi.org/10.1098/rstb.2013.0464.

18. Kodani, A., Kenny, C., Lai, A., Gonzalez, D.M., Stronge, E., Sejourne, G.M., Isacco, L., Partlow, J.N., O'Donnell, A., McWalter, K., et al. (2020). Posterior neocortex-specific regulation of neuronal migration by CEP85L identifies maternal centriole-dependent activation of CDK5. Neuron *106*, 246–255.e6. https://doi.org/10.1016/j.neuron.2020.01.030.

19. O'Neill, A.C., Uzbas, F., Antognolli, G., Merino, F., Draganova, K., Jäck, A., Zhang, S., Pedini, G., Schessner, J.P., Cramer, K., et al. (2022). Spatial centrosome proteome of human neural cells uncovers disease-relevant heterogeneity. Science *376*, eabf9088. https://doi.org/10.1126/science.abf9088.

20. Hasenpusch-Theil, K., and Theil, T. (2021). The multifaceted roles of primary cilia in the development of the cerebral cortex. Front. Cell Dev. Biol. *9*, 630161. https://doi.org/10.3389/fcell.2021.630161.

21. Wilsch-Bräuninger, M., and Huttner, W.B. (2021). Primary cilia and centrosomes in neocortex development. Front. Neurosci. *15*, 755867. https://doi.org/10.3389/fnins.2021.755867.

22. Guo, J., Otis, J.M., Suciu, S.K., Catalano, C., Xing, L., Constable, S., Wachten, D., Gupton, S., Lee, J., Lee, A., et al. (2019). Primary cilia signaling promotes axonal tract development and is disrupted in Joubert syndrome-related disorders models. Dev. Cell *51*, 759–774.e5. https://doi.org/10.1016/j.devcel.2019.11.005.

23. Toro-Tapia, G., and Das, R.M. (2020). Primary cilium remodeling mediates a cell signaling switch in differentiating neurons. Sci. Adv. *6*, eabb0601. https://doi.org/10.1126/sciadv.abb0601.

24. Basto, R., Lau, J., Vinogradova, T., Gardiol, A., Woods, C.G., Khodjakov, A., and Raff, J.W. (2006). Flies without centrioles. Cell *125*, 1375–1386. https://doi.org/10.1016/j.cell.2006.05.025.

25. Stiess, M., Maghelli, N., Kapitein, L.C., Gomis-Rüth, S., Wilsch-Bräuninger, M., Hoogenraad, C.C., Tolić-Nørrelykke, I.M., and Bradke, F. (2010). Axon extension occurs independently of centrosomal microtubule nucleation. Science *327*, 704–707. https://doi.org/10.1126/science.1182179.

26. Yu, W., Centonze, V.E., Ahmad, F.J., and Baas, P.W. (1993). Microtubule nucleation and release from the neuronal centrosome. J. Cell Biol. *122*, 349–359. https://doi.org/10.1083/jcb.122.2.349.

27. Tsai, J.W., Bremner, K.H., and Vallee, R.B. (2007). Dual subcellular roles for LIS1 and dynein in radial neuronal migration in live brain tissue. Nat. Neurosci. *10*, 970–979. https://doi.org/10.1038/nn1934.

28. de Anda, F.C., Pollarolo, G., Da Silva, J.S., Camoletto, P.G., Feiguin, F., and Dotti, C.G. (2005). Centrosome localization determines neuronal polarity. Nature *436*, 704–708. https://doi.org/10.1038/nature03811.

29. Zmuda, J.F., and Rivas, R.J. (1998). The Golgi apparatus and the centrosome are localized to the sites of newly emerging axons in cerebellar granule neurons in vitro. Cell Motil. Cytoskeleton *41*, 18–38. https://doi.org/10.1002/(SICI)1097-0169(1998)41:1<18::AID-CM2>3.0.CO;2-B.

30. de Anda, F.C., Meletis, K., Ge, X., Rei, D., and Tsai, L.H. (2010). Centrosome motility is essential for initial axon formation in the neocortex. J. Neurosci. *30*, 10391–10406. https://doi.org/10.1523/JNEUROSCI.0381-10.2010.

31. Meka, D.P., Scharrenberg, R., Zhao, B., Kobler, O., König, T., Schaefer, I., Schwanke, B., Klykov, S., Richter, M., Eggert, D., et al. (2019). Radial somatic F-actin organization affects growth cone dynamics during early neuronal development. EMBO Rep. *20*, e47743. https://doi.org/10.15252/embr.201947743.

32. Baas, P.W. (1999). Microtubules and neuronal polarity. Neuron *22*, 23–31. https://doi.org/10.1016/S0896-6273(00)80675-3.

33. Ahmad, F.J., Joshi, H.C., Centonze, V.E., and Baas, P.W. (1994). Inhibition of microtubule nucleation at the neuronal centrosome compro-

mises axon growth. Neuron *12*, 271–280. https://doi.org/10.1016/0896-6273(94)90270-4.

34. Gärtner, A., Fornasiero, E.F., Munck, S., Vennekens, K., Seuntjens, E., Huttner, W.B., Valtorta, F., and Dotti, C.G. (2012). N-cadherin specifies first asymmetry in developing neurons. EMBO J. *31*, 1893–1903. https://doi.org/10.1038/emboj.2012.41.

35. Sakakibara, A., Sato, T., Ando, R., Noguchi, N., Masaoka, M., and Miyata, T. (2014). Dynamics of centrosome translocation and microtubule organization in neocortical neurons during distinct modes of polarization. Cereb. Cortex *24*, 1301–1310. https://doi.org/10.1093/cercor/bhs411.

36. Distel, M., Hocking, J.C., Volkmann, K., and Köster, R.W. (2010). The centrosome neither persistently leads migration nor determines the site of axonogenesis in migrating neurons in vivo. J. Cell Biol. *191*, 875–890. https://doi.org/10.1083/jcb.201004154.

37. Nguyen, M.M., Stone, M.C., and Rolls, M.M. (2011). Microtubules are organized independently of the centrosome in Drosophila neurons. Neural Dev. *6*, 38. https://doi.org/10.1186/1749-8104-6-38.

38. Zolessi, F.R., Poggi, L., Wilkinson, C.J., Chien, C.B., and Harris, W.A. (2006). Polarization and orientation of retinal ganglion cells in vivo. Neural Dev. *1*, 2. https://doi.org/10.1186/1749-8104-1-2.

39. Tanaka, N., Meng, W., Nagae, S., and Takeichi, M. (2012). Nezha/CAMSAP3 and CAMSAP2 cooperate in epithelial-specific organization of noncentrosomal microtubules. Proc. Natl. Acad. Sci. USA *109*, 20029–20034. https://doi.org/10.1073/pnas.1218017109.

40. Wu, J., de Heus, C., Liu, Q., Bouchet, B.P., Noordstra, I., Jiang, K., Hua, S., Martin, M., Yang, C., Grigoriev, I., et al. (2016). Molecular pathway of microtubule organization at the Golgi apparatus. Dev. Cell *39*, 44–60. https://doi.org/10.1016/j.devcel.2016.08.009.

41. Gavilan, M.P., Gandolfo, P., Balestra, F.R., Arias, F., Bornens, M., and Rios, R.M. (2018). The dual role of the centrosome in organizing the microtubule network in interphase. EMBO Rep. *19*, 1–21. https://doi.org/10.15252/embr.201845942.

42. Kawauchi, T. (2015). Cellular insights into cerebral cortical development: focusing on the locomotion mode of neuronal migration. Front. Cell. Neurosci. *9*, 394. https://doi.org/10.3389/fncel.2015.00394.

43. Tanaka, T., Serneo, F.F., Higgins, C., Gambello, M.J., Wynshaw-Boris, A., and Gleeson, J.G. (2004). Lis1 and doublecortin function with dynein to mediate coupling of the nucleus to the centrosome in neuronal migration. J. Cell Biol. *165*, 709–721. https://doi.org/10.1083/jcb.200309025.

44. Insolera, R., Shao, W., Airik, R., Hildebrandt, F., and Shi, S.H. (2014). SDCCAG8 regulates pericentriolar material recruitment and neuronal migration in the developing cortex. Neuron *83*, 805–822. https://doi.org/10.1016/j.neuron.2014.06.029.

45. Insolera, R., Bazzi, H., Shao, W., Anderson, K.V., and Shi, S.H. (2014). Cortical neurogenesis in the absence of centrioles. Nat. Neurosci. *17*, 1528–1535. https://doi.org/10.1038/nn.3831.

46. Böhler, A., Vermeulen, B.J.A., Würtz, M., Zupa, E., Pfeffer, S., and Schiebel, E. (2021). The gamma-tubulin ring complex: deciphering the molecular organization and assembly mechanism of a major vertebrate microtubule nucleator. BioEssays *43*, e2100114. https://doi.org/10.1002/bies.202100114.

47. Liu, P., Würtz, M., Zupa, E., Pfeffer, S., and Schiebel, E. (2021). Microtubule nucleation: the waltz between γ-tubulin ring complex and associated proteins. Curr. Opin. Cell Biol. *68*, 124–131. https://doi.org/10.1016/j.ceb.2020.10.004.

48. Haren, L., Remy, M.H., Bazin, I., Callebaut, I., Wright, M., and Merdes, A. (2006). NEDD1-dependent recruitment of the γ-tubulin ring complex to the centrosome is necessary for centriole duplication and spindle assembly. J. Cell Biol. *172*, 505–515. https://doi.org/10.1083/jcb.200510028.

49. Lüders, J., Patel, U.K., and Stearns, T. (2006). GCP-WD is a gamma-tubulin targeting factor required for centrosomal and chromatin-mediated microtubule nucleation. Nat. Cell Biol. *8*, 137–147. https://doi.org/10.1038/ncb1349.

50. Comartin, D., and Pelletier, L. (2016). Organizational properties of the pericentriolar material. In The Microtubule Cytoskeleton, J. Lüders, ed. (Springer), pp. 43–77. https://doi.org/10.1007/978-3-7091-1903-7_3.

51. Moudjou, M., Bordes, N., Paintrand, M., and Bornens, M. (1996). Gamma-tubulin in mammalian cells: the centrosomal and the cytosolic forms. J. Cell Sci. *109*, 875–887. https://doi.org/10.1242/jcs.109.4.875.

52. Choi, Y.K., Liu, P., Sze, S.K., Dai, C., and Qi, R.Z. (2010). CDK5RAP2 stimulates microtubule nucleation by the γ-tubulin ring complex. J. Cell Biol. *191*, 1089–1095. https://doi.org/10.1083/jcb.201007030.

53. Muroyama, A., Seldin, L., and Lechler, T. (2016). Divergent regulation of functionally distinct γ-tubulin complexes during differentiation. J. Cell Biol. *213*, 679–692. https://doi.org/10.1083/jcb.201601099.

54. Wang, Z., Wu, T., Shi, L., Zhang, L., Zheng, W., Qu, J.Y., Niu, R., and Qi, R.Z. (2010). Conserved motif of CDK5RAP2 mediates its localization to centrosomes and the Golgi complex. J. Biol. Chem. *285*, 22658–22665. https://doi.org/10.1074/jbc.M110.105965.

55. Manning, J.A., Shalini, S., Risk, J.M., Day, C.L., and Kumar, S. (2010). A direct interaction with NEDD1 regulates γ-tubulin recruitment to the centrosome. PLoS One *5*, e9618. https://doi.org/10.1371/journal.pone.0009618.

56. Fong, K.W., Choi, Y.K., Rattner, J.B., and Qi, R.Z. (2008). CDK5RAP2 is a pericentriolar protein that functions in centrosomal attachment of the γ-tubulin ring complex. Mol. Biol. Cell *19*, 115–125. https://doi.org/10.1091/mbc.e07-04-0371.

57. Piehl, M., Tulu, U.S., Wadsworth, P., and Cassimeris, L. (2004). Centrosome maturation: measurement of microtubule nucleation throughout the cell cycle by using GFP-tagged EB1. Proc. Natl. Acad. Sci. USA *101*, 1584–1588. https://doi.org/10.1073/pnas.0308205100.

58. Wilson, C., Rozés-Salvador, V., and Cáceres, A. (2020). Protocol for evaluating neuronal polarity in murine models. Star Protoc. *1*, 100114. https://doi.org/10.1016/j.xpro.2020.100114.

59. Chabin-Brion, K., Marceiller, J., Perez, F., Settegrana, C., Drechou, A., Durand, G., and Poüs, C. (2001). The Golgi complex is a microtubule-organizing organelle. Mol. Biol. Cell *12*, 2047–2060.

60. Ravichandran, Y., Goud, B., and Manneville, J.B. (2020). The Golgi apparatus and cell polarity: roles of the cytoskeleton, the Golgi matrix, and Golgi membranes. Curr. Opin. Cell Biol. *62*, 104–113. https://doi.org/10.1016/j.ceb.2019.10.003.

61. Rios, R.M. (2014). The centrosome–Golgi apparatus nexus. Philos. Trans. R. Soc. Lond. B Biol. Sci. *369*, 20130462. https://doi.org/10.1098/rstb.2013.0462.

62. Hurtado, L., Caballero, C., Gavilan, M.P., Cardenas, J., Bornens, M., and Rios, R.M. (2011). Disconnecting the Golgi ribbon from the centrosome prevents directional cell migration and ciliogenesis. J. Cell Biol. *193*, 917–933. https://doi.org/10.1083/jcb.201011014.

63. Yau, K.W., van Beuningen, S.F.B.B., Cunha-Ferreira, I., Cloin, B.M.C.C., van Battum, E.Y., Will, L., Schätzle, P., Tas, R.P., van Krugten, J., Katrukha, E.A., et al. (2014). Microtubule minus-end binding protein CAMSAP2 controls axon specification and dendrite development. Neuron *82*, 1058–1073. https://doi.org/10.1016/j.neuron.2014.04.019.

64. Sánchez-Huertas, C., Freixo, F., Viais, R., Lacasa, C., Soriano, E., and Lüders, J. (2016). Non-centrosomal nucleation mediated by augmin organizes microtubules in post-mitotic neurons and controls axonal microtubule polarity. Nat. Commun. *7*, 12187. https://doi.org/10.1038/ncomms12187.

65. Gillingham, A.K., and Munro, S. (2000). The PACT domain, a conserved centrosomal targeting motif in the coiled-coil proteins AKAP450 and pericentrin. EMBO Rep. *1*, 524–529. https://doi.org/10.1093/embo-reports/kvd105.

66. Lawo, S., Hasegan, M., Gupta, G.D., and Pelletier, L. (2012). Subdiffraction imaging of centrosomes reveals higher-order organizational features of pericentriolar material. Nat. Cell Biol. *14*, 1148–1158. https://doi.org/10.1038/ncb2591.

67. Camargo Ortega, G., Falk, S., Johansson, P.A., Peyre, E., Broix, L., Sahu, S.K., Hirst, W., Schlichthaerle, T., De Juan Romero, C., Draganova, K., et al. (2019). The centrosome protein AKNA regulates neurogenesis via microtubule organization. Nature *567*, 113–117. https://doi.org/10.1038/s41586-019-0962-4.

68. Aprea, J., Prenninger, S., Dori, M., Ghosh, T., Monasor, L.S., Wessendorf, E., Zocher, S., Massalini, S., Alexopoulou, D., Lesche, M., et al. (2013). Transcriptome sequencing during mouse brain development identifies long non-coding RNAs functionally involved in neurogenic commitment. EMBO J. *32*, 3145–3160. https://doi.org/10.1038/emboj.2013.245.

69. Gloster, A., El-Bizri, H., Bamji, S.X., Rogers, D., and Miller, F.D. (1999). Early induction of Talpha1 alpha-tubulin transcription in neurons of the developing nervous system. J. Comp. Neurol. *405*, 45–60. https://doi.org/10.1002/(sici)1096-9861(19990301)405:1<45::aid-cne4>3.0.co;2-m.

70. Gloster, A., Wu, W., Speelman, A., Weiss, S., Causing, C., Pozniak, C., Reynolds, B., Chang, E., Toma, J.G., and Miller, F.D. (1994). The T alpha 1 alpha-tubulin promoter specifies gene expression as a function of neuronal growth and regeneration in transgenic mice. J. Neurosci. *14*, 7319–7330. https://doi.org/10.1523/JNEUROSCI.14-12-07319.1994.

71. Stancik, E.K., Navarro-Quiroga, I., Sellke, R., and Haydar, T.F. (2010). Heterogeneity in ventricular zone neural precursors contributes to neuronal fate diversity in the postnatal neocortex. J. Neurosci. *30*, 7028–7036. https://doi.org/10.1523/JNEUROSCI.6131-09.2010.

72. Jossin, Y., and Cooper, J.A. (2011). Reelin, Rap1 and N-cadherin orient the migration of multipolar neurons in the developing neocortex. Nat. Neurosci. *14*, 697–703. https://doi.org/10.1038/nn.2816.

73. Kon, E., Calvo-Jiménez, E., Cossard, A., Na, Y., Cooper, J.A., and Jossin, Y. (2019). N-cadherin-regulated FGFR ubiquitination and degradation control mammalian neocortical projection neuron migration. eLife *8*, 1–28. https://doi.org/10.7554/eLife.47673.

74. Matsunaga, Y., Noda, M., Murakawa, H., Hayashi, K., Nagasaka, A., Inoue, S., Miyata, T., Miura, T., Kubo, K.I., and Nakajima, K. (2017). Reelin transiently promotes N-cadherin-dependent neuronal adhesion during mouse cortical development. Proc. Natl. Acad. Sci. USA *114*, 2048–2053. https://doi.org/10.1073/pnas.1615215114.

75. Franco, S.J., Martinez-Garay, I., Gil-Sanz, C., Harkins-Perry, S.R., and Müller, U. (2011). Reelin regulates cadherin function via Dab1/Rap1 to control neuronal migration and lamination in the neocortex. Neuron *69*, 482–497. https://doi.org/10.1016/j.neuron.2011.01.003.

76. Kawauchi, T., Sekine, K., Shikanai, M., Chihama, K., Tomita, K., Kubo, K., Nakajima, K., Nabeshima, Y., and Hoshino, M. (2010). Rab GTPases-dependent endocytic pathways regulate neuronal migration and maturation through N-cadherin trafficking. Neuron *67*, 588–602. https://doi.org/10.1016/j.neuron.2010.07.007.

77. Hunt, S.D., Townley, A.K., Danson, C.M., Cullen, P.J., and Stephens, D.J. (2013). Microtubule motors mediate endosomal sorting by maintaining functional domain organization. J. Cell Sci. *126*, 2493–2501. https://doi.org/10.1242/jcs.122317.

78. Marie, M., Dale, H.A., Sannerud, R., and Saraste, J. (2009). The function of the intermediate compartment in pre-Golgi trafficking involves its stable connection with the centrosome. Mol. Biol. Cell *20*, 4458–4470. https://doi.org/10.1091/mbc.e08-12-1229.

79. Hehnly, H., Chen, C.T., Powers, C.M., Liu, H.L., and Doxsey, S. (2012). The centrosome regulates the Rab11- dependent recycling endosome pathway at appendages of the mother centriole. Curr. Biol. *22*, 1944–1950. https://doi.org/10.1016/j.cub.2012.08.022.

80. Zhou, Z., Xu, H., Li, Y., Yang, M., Zhang, R., Shiraishi, A., Kiyonari, H., Liang, X., Huang, X., Wang, Y., et al. (2020). CAMSAP1 breaks the homeostatic microtubule network to instruct neuronal polarity. Proc. Natl. Acad. Sci. USA *117*, 22193–22203. https://doi.org/10.1073/pnas.1913177117.

81. Chen, Y., Zheng, J., Li, X., Zhu, L., Shao, Z., Yan, X., and Zhu, X. (2020). Wdr47 controls neuronal polarization through the Camsap family

microtubule minus-end-binding proteins. Cell Rep. *31*, 107526. https://doi.org/10.1016/j.celrep.2020.107526.

82. Pongrakhananon, V., Saito, H., Hiver, S., Abe, T., Shioi, G., Meng, W., and Takeichi, M. (2018). CAMSAP3 maintains neuronal polarity through regulation of microtubule stability. Proc. Natl. Acad. Sci. USA *115*, 9750–9755. https://doi.org/10.1073/pnas.1803875115.

83. Jakobsen, L., Vanselow, K., Skogs, M., Toyoda, Y., Lundberg, E., Poser, I., Falkenby, L.G., Bennetzen, M., Westendorf, J., Nigg, E.A., et al. (2011). Novel asymmetrically localizing components of human centrosomes identified by complementary proteomics methods. EMBO J. *30*, 1520–1535. https://doi.org/10.1038/emboj.2011.63.

84. Thawani, A., Rale, M.J., Coudray, N., Bhabha, G., Stone, H.A., Shaevitz, J.W., and Petry, S. (2020). The transition state and regulation of γ-TuRC-mediated microtubule nucleation revealed by single molecule microscopy. eLife *9*, 1–34. https://doi.org/10.7554/eLife.54253.

85. Liu, P., Zupa, E., Neuner, A., Böhler, A., Loerke, J., Flemming, D., Ruppert, T., Rudack, T., Peter, C., Spahn, C., et al. (2020). Insights into the assembly and activation of the microtubule nucleator γ-TuRC. Nature *578*, 467–471. https://doi.org/10.1038/s41586-019-1896-6.

86. Consolati, T., Locke, J., Roostalu, J., Chen, Z.A., Gannon, J., Asthana, J., Lim, W.M., Martino, F., Cvetkovic, M.A., Rappsilber, J., et al. (2020). Microtubule nucleation properties of single human γTuRCs explained by their cryo-EM structure. Dev. Cell *53*, 603–617.e8. https://doi.org/10.1016/j.devcel.2020.04.019.

87. Sanchez, A.D., and Feldman, J.L. (2017). Microtubule-organizing centers: from the centrosome to non-centrosomal sites. Curr. Opin. Cell Biol. *44*, 93–101. https://doi.org/10.1016/j.ceb.2016.09.003.

88. Pimenta-Marques, A., Bento, I., Lopes, C.A.M., Duarte, P., Jana, S.C., and Bettencourt-Dias, M. (2016). A mechanism for the elimination of the female gamete centrosome in Drosophila melanogaster. Science *353*, aaf4866. https://doi.org/10.1126/science.aaf4866.

89. Cunha-Ferreira, I., Chazeau, A., Buijs, R.R., Stucchi, R., Will, L., Pan, X., Adolfs, Y., van der Meer, C., Wolthuis, J.C., Kahn, O.I., et al. (2018). The HAUS complex is a key regulator of non-centrosomal microtubule organization during neuronal development. Cell Rep. *24*, 791–800. https://doi.org/10.1016/j.celrep.2018.06.093.

90. Buijs, R.R., Hummel, J.J.A., Burute, M., Pan, X., Cao, Y., Stucchi, R., Altelaar, M., Akhmanova, A., Kapitein, L.C., and Hoogenraad, C.C. (2021). WDR47 protects neuronal microtubule minus ends from katanin-mediated severing. Cell Rep. *36*, 109371. https://doi.org/10.1016/j.celrep.2021.109371.

91. Shi, S.H., Jan, L.Y., and Jan, Y.N. (2003). Hippocampal neuronal polarity specified by spatially localized mPar3/mPar6 and PI 3-kinase activity. Cell *112*, 63–75. https://doi.org/10.1016/S0092-8674(02)01249-7.

92. Ménager, C., Arimura, N., Fukata, Y., and Kaibuchi, K. (2004). PIP3 is involved in neuronal polarization and axon formation. J. Neurochem. *89*, 109–118. https://doi.org/10.1046/j.1471-4159.2004.02302.x.

93. Barnes, A.P., Lilley, B.N., Pan, Y.A., Plummer, L.J., Powell, A.W., Raines, A.N., Sanes, J.R., and Polleux, F. (2007). LKB1 and SAD kinases define a pathway required for the polarization of cortical neurons. Cell *129*, 549–563. https://doi.org/10.1016/j.cell.2007.03.025.

94. Shelly, M., Cancedda, L., Heilshorn, S., Sumbre, G., and Poo, M.M. (2007). LKB1/STRAD promotes axon initiation during neuronal polarization. Cell *129*, 565–577. https://doi.org/10.1016/j.cell.2007.04.012.

95. Asada, N., Sanada, K., and Fukada, Y. (2007). LKB1 regulates neuronal migration and neuronal differentiation in the developing neocortex through centrosomal positioning. J. Neurosci. *27*, 11769–11775. https://doi.org/10.1523/JNEUROSCI.1938-07.2007.

96. Conde, C., and Cáceres, A. (2009). Microtubule assembly, organization and dynamics in axons and dendrites. Nat. Rev. Neurosci. *10*, 319–332. https://doi.org/10.1038/nrn2631.

97. Takano, T., Funahashi, Y., and Kaibuchi, K. (2019). Neuronal polarity: positive and negative feedback signals. Front. Cell Dev. Biol. *7*, 69. https://doi.org/10.3389/fcell.2019.00069.

98. Leask, A., Obrietan, K., and Stearns, T. (1997). Synaptically coupled central nervous system neurons lack centrosomal γ- tubulin. Neurosci. Lett. *229*, 17–20. https://doi.org/10.1016/S0304-3940(97)00412-6.

99. Yonezawa, S., Shigematsu, M., Hirata, K., and Hayashi, K. (2015). Loss of γ-tubulin, GCP-WD/NEDD1 and CDK5RAP2 from the centrosome of Neurons in Developing Mouse Cerebral and cerebellar Cortex. Acta Histochem. Cytochem. *48*, 145–152. https://doi.org/10.1267/ahc.15023.

100. Renthal, W., Tochitsky, I., Yang, L., Cheng, Y.C., Li, E., Kawaguchi, R., Geschwind, D.H., and Woolf, C.J. (2020). Transcriptional reprogramming of distinct peripheral sensory neuron subtypes after axonal injury. Neuron *108*, 128–144.e9. https://doi.org/10.1016/j.neuron.2020.07.026.

101. Hilton, B.J., and Bradke, F. (2017). Can injured adult CNS axons regenerate by recapitulating development? Development *144*, 3417–3429. https://doi.org/10.1242/dev.148312.

102. Ertürk, A., Hellal, F., Enes, J., and Bradke, F. (2007). Disorganized microtubules underlie the formation of retraction bulbs and the failure of axonal regeneration. J. Neurosci. *27*, 9169–9180. https://doi.org/10.1523/JNEUROSCI.0612-07.2007.

103. Hellal, F., Hurtado, A., Ruschel, J., Flynn, K.C., Laskowski, C.J., Umlauf, M., Kapitein, L.C., Strikis, D., Lemmon, V., Bixby, J., et al. (2011). Microtubule stabilization reduces scarring and causes axon regeneration after spinal cord injury. Science *331*, 928–931. https://doi.org/10.1126/science.1201148.

104. Ruschel, J., Hellal, F., Flynn, K.C., Dupraz, S., Elliott, D.A., Tedeschi, A., Bates, M., Sliwinski, C., Brook, G., Dobrindt, K., et al. (2015). Axonal regeneration. Systemic administration of epothilone B promotes axon regeneration after spinal cord injury. Science *348*, 347–352. https://doi.org/10.1126/science.aaa2958.

105. Stern, S., Hilton, B.J., Burnside, E.R., Dupraz, S., Handley, E.E., Gonyer, J.M., Brakebusch, C., and Bradke, F. (2021). RhoA drives actin compaction to restrict axon regeneration and astrocyte reactivity after CNS injury. Neuron *109*, 3436–3455.e9. https://doi.org/10.1016/j.neuron.2021.08.014.

106. Yokota, Y., Ring, C., Cheung, R., Pevny, L., and Anton, E.S. (2007). Nap1-regulated neuronal cytoskeletal dynamics is essential for the final differentiation of neurons in cerebral cortex. Neuron *54*, 429–445. https://doi.org/10.1016/j.neuron.2007.04.016.

107. Azzarelli, R., Pacary, E., Garg, R., Garcez, P., van den Berg, D., Riou, P., Ridley, A.J., Friedel, R.H., Parsons, M., and Guillemot, F. (2014). An antagonistic interaction between PlexinB2 and Rnd3 controls RhoA activity and cortical neuron migration. Nat. Commun. *5*, 3405. https://doi.org/10.1038/ncomms4405.

108. Shankar, S., Hsu, Z.T., Ezquerra, A., Li, C.C., Huang, T.L., Coyaud, E., Viais, R., Grauffel, C., Raught, B., Lim, C., et al. (2022). A γ-tubulin complex-dependent pathway suppresses ciliogenesis by promoting cilia disassembly. Cell Rep. *41*, 111642. https://doi.org/10.1016/j.celrep.2022.111642.

109. Ferent, J., Constable, S., Gigante, E.D., Yam, P.T., Mariani, L.E., Legué, E., Liem, K.F., Caspary, T., and Charron, F. (2019). The ciliary protein Arl13b functions outside of the primary cilium in shh-mediated axon guidance. Cell Rep. *29*, 3356–3366.e3. https://doi.org/10.1016/j.celrep.2019.11.015.

110. Garvalov, B.K., Flynn, K.C., Neukirchen, D., Meyn, L., Teusch, N., Wu, X., Brakebusch, C., Bamburg, J.R., and Bradke, F. (2007). Cdc42 regulates cofilin during the establishment of neuronal polarity. J. Neurosci. *27*, 13117–13129. https://doi.org/10.1523/JNEUROSCI.3322-07.2007.

111. Tahirovic, S., Hellal, F., Neukirchen, D., Hindges, R., Garvalov, B.K., Flynn, K.C., Stradal, T.E., Chrostek-Grashoff, A., Brakebusch, C., and Bradke, F. (2010). Rac1 regulates neuronal polarization through the

WAVE complex. J. Neurosci. *30*, 6930–6943. https://doi.org/10.1523/JNEUROSCI.5395-09.2010.

112. Azzarelli, R., Kerloch, T., and Pacary, E. (2014). Regulation of cerebral cortex development by Rho GTPases: insights from in vivo studies. Front. Cell. Neurosci. *8*, 445. https://doi.org/10.3389/fncel.2014.00445.

113. Shu, T., Ayala, R., Nguyen, M.D., Xie, Z., Gleeson, J.G., and Tsai, L.H. (2004). Ndel1 operates in a common pathway with LIS1 and cytoplasmic dynein to regulate cortical neuronal positioning. Neuron *44*, 263–277. https://doi.org/10.1016/j.neuron.2004.09.030.

114. Tsai, J.W., Chen, Y., Kriegstein, A.R., and Vallee, R.B. (2005). LIS1 RNA interference blocks neural stem cell division, morphogenesis, and motility at multiple stages. J. Cell Biol. *170*, 935–945. https://doi.org/10.1083/jcb.200505166.

115. Gonçalves, J.C., Dantas, T.J., and Vallee, R.B. (2019). Distinct roles for dynein light intermediate chains in neurogenesis, migration, and terminal somal translocation. J. Cell Biol. *218*, 808–819. https://doi.org/10.1083/jcb.201806112.

116. Ivanova, E.L., Gilet, J.G., Sulimenko, V., Duchon, A., Rudolf, G., Runge, K., Collins, S.C., Asselin, L., Broix, L., Drouot, N., et al. (2019). TUBG1 missense variants underlying cortical malformations disrupt neuronal locomotion and microtubule dynamics but not neurogenesis. Nat. Commun. *10*, 2129. https://doi.org/10.1038/s41467-019-10081-8.

117. Poirier, K., Lebrun, N., Broix, L., Tian, G., Saillour, Y., Boscheron, C., Parrini, E., Valence, S., Pierre, B.S., Oger, M., et al. (2013). Mutations in TUBG1, DYNC1H1, KIF5C and KIF2A cause malformations of cortical development and microcephaly. Nat. Genet. *45*, 639–647. https://doi.org/10.1038/ng.2613.

118. Nishimura, Y.V., Shikanai, M., Hoshino, M., Ohshima, T., Nabeshima, Y., Mizutani, K., Nagata, K., Nakajima, K., and Kawauchi, T. (2014). Cdk5 and its substrates, Dcx and p27Kip1, regulate cytoplasmic dilation formation and nuclear elongation in migrating neurons. Development *141*, 3540–3550. https://doi.org/10.1242/dev.111294.

119. Delgehyr, N., Sillibourne, J., and Bornens, M. (2005). Microtubule nucleation and anchoring at the centrosome are independent processes linked by ninein function. J. Cell Sci. *118*, 1565–1575. https://doi.org/10.1242/jcs.02302.

120. Das, R.M., and Storey, K.G. (2014). Apical abscission alters cell polarity and dismantles the primary cilium during neurogenesis. Science *343*, 200–204. https://doi.org/10.1126/science.1247521.

121. Kasioulis, I., Das, R.M., and Storey, K.G. (2017). Inter-dependent apical microtubule and actin dynamics orchestrate centrosome retention and neuronal delamination. eLife *6*, 1–31. https://doi.org/10.7554/eLife.26215.

122. Santos, T.E., Schaffran, B., Broguière, N., Meyn, L., Zenobi-Wong, M., and Bradke, F. (2020). Axon growth of CNS neurons in three dimensions is amoeboid and independent of adhesions. Cell Rep. *32*, 107907. https://doi.org/10.1016/j.celrep.2020.107907.

123. Brock, S., Stouffs, K., Scalais, E., D'Hooghe, M., Keymolen, K., Guerrini, R., Dobyns, W.B., Di Donato, N., and Jansen, A.C. (2018). Tubulinopathies continued: refining the phenotypic spectrum associated with variants in TUBG1. Eur. J. Hum. Genet. *26*, 1132–1142. https://doi.org/10.1038/s41431-018-0146-y.

124. Yuen, Y.T.K., Guella, I., Roland, E., Sargent, M., and Boelman, C. (2019). Case reports: novel TUBG1 mutations with milder neurodevelopmental presentations. BMC Med. Genet. *20*, 95. https://doi.org/10.1186/s12881-019-0827-6.

125. Shen, R., Zhang, Z., Zhuang, Y., Yang, X., and Duan, L. (2021). A novel TUBG1 mutation with neurodevelopmental disorder caused by malformations of cortical development. BioMed Res. Int. *2021*, 6644274. https://doi.org/10.1155/2021/6644274.

126. Chakraborti, S., Natarajan, K., Curiel, J., Janke, C., and Liu, J. (2016). The emerging role of the tubulin code: from the tubulin molecule to neuronal function and disease. Cytoskeleton (Hoboken) *73*, 521–550. https://doi.org/10.1002/cm.21290.

127. Gonçalves, F.G., Freddi, T.A.L., Taranath, A., Lakshmanan, R., Goetti, R., Feltrin, F.S., Mankad, K., Teixeira, S.R., Hanagandi, P.B., and Arrigoni, F. (2018). Tubulinopathies. Top. Magn. Reson. Imaging *27*, 395–408. https://doi.org/10.1097/RMR.0000000000000188.

128. Kapitein, L.C., Yau, K.W., and Hoogenraad, C.C. (2010). Microtubule dynamics in dendritic spines. Methods Cell Biol. *97*, 111–132. https://doi.org/10.1016/S0091-679X(10)97007-6.

129. Shaner, N.C., Lin, M.Z., McKeown, M.R., Steinbach, P.A., Hazelwood, K.L., Davidson, M.W., and Tsien, R.Y. (2008). Improving the photostability of bright monomeric orange and red fluorescent proteins. Nat. Methods *5*, 545–551. https://doi.org/10.1038/nmeth.1209.

130. Flynn, K.C., Hellal, F., Neukirchen, D., Jacob, S., Tahirovic, S., Dupraz, S., Stern, S., Garvalov, B.K., Gurniak, C., Shaw, A.E., et al. (2012). ADF/cofilin-mediated actin retrograde flow directs neurite formation in the developing brain. Neuron *76*, 1091–1107. https://doi.org/10.1016/j.neuron.2012.09.038.

131. Norris, S.R., Núñez, M.F., and Verhey, K.J. (2015). Influence of fluorescent tag on the motility properties of Kinesin-1 in single-molecule assays. Biophys. J. *108*, 1133–1143. https://doi.org/10.1016/j.bpj.2015.01.031.

132. Alfadil, E., Bradke, F., and Dupraz, S. (2021). *In situ* visualization of axon growth and growth cone dynamics in acute *ex vivo* embryonic brain slice cultures. J. Vis. Exp. *176*, e63068. https://doi.org/10.3791/63068.

133. Bindels, D.S., Haarbosch, L., Van Weeren, L., Postma, M., Wiese, K.E., Mastop, M., Aumonier, S., Gotthard, G., Royant, A., Hink, M.A., et al. (2017). MScarlet: A bright monomeric red fluorescent protein for cellular imaging. Nat. Methods *14*, 53–56. https://doi.org/10.1038/nmeth.4074.

134. Schindelin, J., Arganda-Carreras, I., Frise, E., Kaynig, V., Longair, M., Pietzsch, T., Preibisch, S., Rueden, C., Saalfeld, S., Schmid, B., et al. (2012). Fiji: an open-source platform for biological-image analysis. Nat. Methods *9*, 676–682. https://doi.org/10.1038/nmeth.2019.

135. Longair, M.H., Baker, D.A., and Armstrong, J.D. (2011). Simple Neurite Tracer: open source software for reconstruction, visualization and analysis of neuronal processes. Bioinformatics *27*, 2453–2454. https://doi.org/10.1093/bioinformatics/btr390.

136. Applegate, K.T., Besson, S., Matov, A., Bagonis, M.H., Jaqaman, K., and Danuser, G. (2011). plusTipTracker: quantitative image analysis software for the measurement of microtubule dynamics. J. Struct. Biol. *176*, 168–184. https://doi.org/10.1016/j.jsb.2011.07.009.

137. Meijering, E., Dzyubachyk, O., and Smal, I. (2012). Methods for cell and particle tracking. In Methods Enzymol., P.M. Conn, ed. (Elsevier), pp. 183–200. https://doi.org/10.1016/B978-0-12-391857-4.00009-4.

138. Kaech, S., and Banker, G. (2006). Culturing hippocampal neurons. Nat. Protoc. *1*, 2406–2415. https://doi.org/10.1038/nprot.2006.356.

139. Shaner, N.C., Lambert, G.G., Chammas, A., Ni, Y., Cranfill, P.J., Baird, M.A., Sell, B.R., Allen, J.R., Day, R.N., Israelsson, M., et al. (2013). A bright monomeric green fluorescent protein derived from Branchiostoma lanceolatum. Nat. Methods *10*, 407–409. https://doi.org/10.1038/nmeth.2413.

140. Murakoshi, H., Wang, H., and Yasuda, R. (2011). Local, persistent activation of Rho GTPases during plasticity of single dendritic spines. Nature *472*, 100–104. https://doi.org/10.1038/nature09823.

141. Vinopal, S., Černohorská, M., Sulimenko, V., Sulimenko, T., Vosecká, V., Flemr, M., Dráberová, E., and Dráber, P. (2012). γ-tubulin 2 Nucleates Microtubules and Is Downregulated in Mouse Early Embryogenesis. PLoS One *7*, e29919. https://doi.org/10.1371/journal.pone.0029919.

142. Graser, S., Stierhof, Y.D., and Nigg, E.A. (2007). Cep68 and Cep215 (Cdk5rap2) are required for centrosome cohesion. J. Cell Sci. *120*, 4321–4331. https://doi.org/10.1242/jcs.020248.

143. Hermann, M., Stillhard, P., Wildner, H., Seruggia, D., Kapp, V., Sánchez-Iranzo, H., Mercader, N., Montoliu, L., Zeilhofer, H.U., and Pelczar, P. (2014). Binary recombinase systems for high-resolution conditional

mutagenesis. Nucleic Acids Res. *42*, 3894–3907. https://doi.org/10.1093/nar/gkt1361.

144. Schelski, M., and Bradke, F. (2022). Microtubule retrograde flow retains neuronal polarization in a fluctuating state. Sci. Adv. *8*, eabo2336. https://doi.org/10.1126/sciadv.abo2336.

145. Nechiporuk, T., Fernandez, T.E., and Vasioukhin, V. (2007). Failure of epithelial tube maintenance causes Hydrocephalus and renal cysts in Dlg5−/− mice. Dev. Cell *13*, 338–350. https://doi.org/10.1016/j.devcel.2007.07.017.

146. Smith, C.L. (1994). Cytoskeletal movements and substrate interactions during initiation of neurite outgrowth by sympathetic neurons in vitro. J. Neurosci. *14*, 384–398. https://doi.org/10.1523/JNEUROSCI.14-01-00384.1994.

147. Thévenaz, P., and Unser, M. (2007). User-friendly semiautomated assembly of accurate image mosaics in microscopy. Microsc. Res. Tech. *70*, 135–146. https://doi.org/10.1002/jemt.20393.

148. Banker, G. (2018). The development of neuronal polarity: A retrospective view. J. Neurosci. *38*, 1867–1873. https://doi.org/10.1523/JNEUROSCI.1372-16.2018.

149. Susaki, E.A., Tainaka, K., Perrin, D., Yukinaga, H., Kuno, A., and Ueda, H.R. (2015). Advanced CUBIC protocols for whole-brain and whole-body clearing and imaging. Nat. Protoc. *10*, 1709–1727. https://doi.org/10.1038/nprot.2015.085.

150. Hilton, B.J., Blanquie, O., Tedeschi, A., and Bradke, F. (2019). High-resolution 3D imaging and analysis of axon regeneration in unsectioned spinal cord with or without tissue clearing. Nat. Protoc. *14*, 1235–1260. https://doi.org/10.1038/s41596-019-0140-z.

STAR★METHODS

KEY RESOURCES TABLE

REAGENT or RESOURCE	SOURCE	IDENTIFIER
Antibodies		
Rabbit polyclonal Cep135	Abcam	Cat#ab75005; RRID:AB_1523339
Rat monoclonal Ctip2	Abcam	Cat#ab18465; RRID: AB_2064130
Chicken polyclonal GFP	Abcam	Cat#ab13970; RRID:AB_300798
Rabbit monoclonal Ki67	Abcam	Cat#ab16667; RRID: AB_302459
Rabbit polyclonal Pericentrin	Abcam	Cat#ab4448; RRID:AB_304461
Mouse monoclonal Satb2	Abcam	Cat#ab51502; RRID: AB_882455
Rabbit polyclonal Tbr1	Abcam	Cat#ab31940; RRID: AB_2200219
Mouse monoclonal GM130	BD Biosciences	Cat#BD610823
Rabbit polyclonal Pericentrin	Covance	Cat# PRB-432C
Rabbit polyclonal NEDD1	Genetex	Cat#GTX32744
Rabbit polyclonal Cdk5rap2	Millipore	Cat#ABE236; RRID: AB_10918303
Mouse monoclonal Centrin	Millipore	Cat#04-1624; RRID:AB_10563501
Rabbit polyclonal MAP2	Millipore	Cat#AB5622; RRID: AB_91939
Guiney pig polyclonal NeuN	Millipore	Cat#ABN90P; RRID: AB_2341095
Mouse monoclonal Tau-1	Millipore	Cat#MAB3420; RRID:AB_94855
Rabbit polyclonal RFP	Rockland	Cat#600-401-379; RRID:AB_1523339
Chicken polyclonal RFP	Rockland	Cat#600-901-379; RRID: AB_10704808
Rabbit polyclonal βIII-tubulin	Sigma	Cat#T2200; RRID:AB_262133
Mouse monoclonal γ-tubulin	Sigma	Cat#T6557; RRID:AB_477584
Rat monoclonal Akna (clone 14D7)	Magdalena Götz (Camargo Ortega et al.[67])	N/A
Chemicals, peptides, and recombinant proteins		
Nocodazole, ≥99% (TLC), powder	Sigma	Cat#M1404-10MG
Deposited data		
Rat *Cdk5rap2* isoform	This paper	GenBank: MF541099
Rat *Nedd1* isoform	This paper	GenBank: MT415945
Experimental models: Organisms/strains		
Rat, Sprague-Dawley	Janvier labs	https://www.janvier-labs.com/en/fiche_produit/sprague_dawley_rat/
Mouse, C57BL/6JRj	Janvier labs	https://www.janvier-labs.com/en/fiche_produit/c57bl-6jrj_mouse/
Oligonucleotides		
Oligonucleotides listed in Table S2	This paper	N/A
Recombinant DNA		
Pβactin vector	C. C. Hoogenraad (Kapitein et al.[128])	N/A
pEGFP-Centrin2	R. W. Köster (Distel et al.[36])	N/A

(Continued on next page)

Continued

REAGENT or RESOURCE	SOURCE	IDENTIFIER
pCS-Centrin2-tdTomato	R. W. Köster (Distel et al.[36])	N/A
pEGFP-NEDD1-gTBD	P. Dráber	N/A
pmNeonGreen-N1	Gentaur Europe BVBA	http://www.allelebiotech.com/mneongreen/; Shaner et al.[129]
pmNeonGreen-C1	Gentaur Europe BVBA	http://www.allelebiotech.com/mneongreen/; Shaner et al.[129]
pAcGFP-CI	Clontech	Cat#632470
pEB3-mCherry	Our laboratory (Flynn et al.[130])	N/A
mOrange2-EB3-7	M. Davidson (Shaner et al.[129])	Addgene plasmid #57953
pKIF5C(1-560)-2xmCherryALTv2	K. Verhey (Norris et al.[131])	N/A
pCAG-IRES-EGFP	Magdalena Götz (Camargo Ortega et al.[67])	N/A
pCAG-Akna-IRES-EGFP	Magdalena Götz (Camargo Ortega et al.[67])	N/A
pDCx-Akna-IRES-EGFP	Magdalena Götz (Camargo Ortega et al.[67])	N/A
pTα1-iCre	Our laboratory (Dupraz et al.[14])	Addgene plasmid # 133924
pCAG-roxSTOProx-LynEGFP	Our laboratory (Dupraz et al.[14])	Addgene plasmid # 133923
pCAG-lox-STOP-lox-EB3-mNeonGreen	This paper	N/A
pTα1-Dre	Our laboratory (Dupraz et al.[14])	Addgene plasmid # 133925
pCAG-loxSTOPlox-Lyn-EGFP	Our laboratory (Dupraz et al.[14])	Addgene plasmid # 133922
pCAG-lox-roxSTOProx-tRFP-pA-lox-ZsGreen-pA	Our laboratory (Alfadil et al.[132])	Addgene plasmid # 175438
pmScarlet-Giantin-C1	Dorus Gadella (Bindels et al.[133])	Addgene plasmid # 850480
pβactin-EB3-mNeonGreen	This paper	Addgene plasmid # 196848
pβactin-AcGFP-CI	This paper	Addgene plasmid # 196849
pβactin-mNeonGreen-CI	This paper	Addgene plasmid # 196850
pβactin-td-mCherry-CI	This paper	Addgene plasmid # 196851
pβactin-mOrange2-CI	This paper	Addgene plasmid # 196852
pβactin-AcGFP-Cdk5rap2-CTD	This paper	Addgene plasmid # 196853
pβactin-td-mCherry-Cdk5rap2-CTD	This paper	Addgene plasmid # 196854
pβactin-mOrange2-Cdk5rap2-CTD	This paper	Addgene plasmid # 196855
pβactin-AcGFP-Cdk5rap2-CTDΔCBD	This paper	Addgene plasmid # 196856
pβactin-EGFP-NEDD1-gTBD	This paper	Addgene plasmid # 196857
pβactin-mOrange2-NEDD1-gTBD	This paper	Addgene plasmid # 196858
pβactin-td-mCherry-Cdk5rap2	This paper	Addgene plasmid # 196859
pβactin-Nedd1-mOrange2	This paper	Addgene plasmid # 196860
pβactin-Nedd1-mOrange2-rCM1	This paper	Addgene plasmid # 196861
pβactin-Nedd1-mOrange2-F75A	This paper	Addgene plasmid # 196862
pβactin-Nedd1-mOrange2-hCM1	This paper	Addgene plasmid # 196863
pβactin-Nedd1-mNeonGreen	This paper	Addgene plasmid # 196864
pβactin-Akna-mOrange2	This paper	Addgene plasmid # 196865
pβactin-Akna-mEGFP	This paper	Addgene plasmid # 196866
pCR-XL-rAkap9	This paper	Addgene plasmid # 196867

(Continued on next page)

Continued

REAGENT or RESOURCE	SOURCE	IDENTIFIER
pβactin-PACT-mOrange2-hCM1	This paper	Addgene plasmid # 196868
pβactin-Tubg1-mNeonGreen	This paper	Addgene plasmid # 196869
pβactin-Tubg1-mEGFP	This paper	Addgene plasmid # 196870
pβactin-AcGFP-128-425-Akap9	This paper	Addgene plasmid # 196871
pCAG-mScarlet-Giantin	This paper	Addgene plasmid # 196872
pCAG-Halo-Tag-128-425-Akap9	This paper	Addgene plasmid # 196873
pCAG-rox-inv[Tα1-iCre-pA]-rox-LynGFP	This paper	Addgene plasmid # 196874
pCAG-lox-inv[Tα1-iCre-pA]-lox-Lyn-EGFP	This paper	Addgene plasmid # 196875
pCAG-lox-inv[Tα1-Dre-pA]-lox-Lyn-EGFP	This paper	Addgene plasmid # 196876
pCAG-lox-inv[Tα1-iCre-pA]-lox-mOrange2-C1	This paper	Addgene plasmid # 196877
pCAG-lox-inv[Tα1-iCre-pA]-lox-mOrange2-NEDD1-gTBD	This paper	Addgene plasmid # 196878
pCAG-lox-inv[Tα1-iCre-pA]-lox-Nedd1-mOrange2-rCM1	This paper	Addgene plasmid # 196879
pCAG-lox-inv[Tα1-iCre-pA]-lox-Akna-mOrange2	This paper	Addgene plasmid # 196880
pCAG-lox-inv[Tα1-Dre-pA]-lox-mOrange2-Cdk5rap2-CTD	This paper	Addgene plasmid # 196881
pCAG-DIO-basic	This paper	Addgene plasmid # 196882
pCAG-DIO-inv[roxSTOProx-ZsGreen-bGH]	This paper	Addgene plasmid # 196883
pCAG-DIO-inv[roxSTOProx-Lyn-GFP-bGH]	This paper	Addgene plasmid # 196884
pCAG-DIO-inv[roxSTOProx-EB3 mNeonGreen-bGH]	This paper	Addgene plasmid # 196885
pβactin-DIO-inv[roxSTOProx-ZsGreen-bGH]	This paper	Addgene plasmid # 196886
pβactin-DIO-inv[roxSTOProx-EB3-mNeonGreen-bGH]	This paper	Addgene plasmid # 196887
pCAG-lox-roxSTOProx-tRFP-pA-lox	This paper	Addgene plasmid # 196888
pCAG-lox-roxSTOProx-lyn-mScarlet-pA-lox	This paper	Addgene plasmid # 196889
pCAG-lox-inv[Tα1-iCre-pA]-lox-mNeonGreen-hCentrin1	This paper	Addgene plasmid # 196890
pCAG-lox-inv[Tα1-iCre-pA]-lox-2xHA-hCentrin1	This paper	Addgene plasmid # 196891
pCAG-rox-inv[Tα1-iCre-pA]-rox-mNeonGreen-hCentrin1	This paper	Addgene plasmid # 196892
pCAG-lox-inv[Tα1-HA-Dre]-lox-Akna-mOrange2	This paper	Addgene plasmid # 196893
pCAG-lox-inv[Tα1-HA-Dre]-lox-NEDD1-gTBD-mOrange2	This paper	Addgene plasmid # 196894
pCAG-lox-inv[Tα1-Dre-PA]-lox-2xHA-CAMSAP3	This paper	Addgene plasmid # 196895
pCAG-lox-inv[Tα1-Dre-PA]-lox-N-Cadherin-2xHA	This paper	Addgene plasmid # 196896
pCAG-lox-inv[Tα1-iCre-pA]-lox-2xHA-128-425-Akap9	This paper	Addgene plasmid # 196897
pβactin-Halo-Tag	This paper	Addgene plasmid # 196898
Software and algorithms		
FiJi	Schindelin et al.[134]	https://fiji.sc/
Simple neurite tracer	Longair et al.[135]	N/A
Imaris 8.1.2, 9.2, 9.7.2	Bitplane	http://www.bitplane.com/imaris
u-track 2.1.3, u-track master 2.2.0	Applegate et al.[136]	https://github.com/DanuserLab/u-track
MtrackJ	Meijering et al.[137]	https://imagescience.org/meijering/software/mtrackj/
R		https://www.r-project.org/
Python 2.7		https://www.python.org/
Prism 7.0c, 8.1.2, 9.2.0	GraphPad Software	https://www.graphpad.com/
Process_EB3_centrosome_Golgi_areas.py (a python script for extraction and evaluation of EB3 tracks acquired by u-track)	This paper	Zenodo: https://doi.org/10.5281/zenodo.7554027
stitch.py (a python script for stitching tile-scan DeltaVision files)	This paper	Zenodo: https://doi.org/10.5281/zenodo.7554027

RESOURCE AVAILABILITY

Lead contact
Further information and requests for resources and reagents should be directed to and will be fulfilled by the lead contact, Frank Bradke (Frank.Bradke@dzne.de).

Materials availability
Recombinant DNA generated in this study is available upon request from the lead contact.

Data and code availability
- This study did not generate datasets of which mandatory deposition is required besides CDS of novel rat Cdk5rap2 (Genbank: MF541099) and Nedd1 (Genbank: MT415945) isoforms that have been uploaded to GenBank; the corresponding accession numbers are listed in the key resources table. Recombinant DNA generated in this work was made publicly available on Addgene and the accession numbers are reported in the key resources table. Original data reported in this paper will be shared by the lead contact upon request.
- Our in-house written macros for analysis of EB3 tracking data and for stitching of DeltaVision tile-scan image files have been deposited to Zenodo and are publicly available as of the date of publication. The corresponding DOI is listed in the key resources table.
- Any additional information required to reanalyze the data reported in this paper is available from the lead contact upon request.

EXPERIMENTAL MODEL AND SUBJECT DETAILS

Animals
All animal experiments were performed in accordance to the Animal Welfare Act and the guidelines of the Landesamt für Natur, Umwelt und Verbraucherschutz (LANUV, NRW, Germany).

Timed-pregnant Sprague-Dawley rats (Charles River and Janvier) were used as a source of E17 embryos for all primary cell cultures (detailed below).

Timed-pregnant C57BL/6JRj mice (Janvier labs) were used as a source of E13 to E18 embryos for IUE and EUE experiments or of E16, E18 and P2 wildtype animals for immunohistochemistry or E17 wildtype embryos for cortical microdisection followed by western blot (see method details). The embryos after IUE were allowed to develop to indicated timepoints depending on the experiment as elaborated further in the method details and stated in the Figure legends. The sex of either the embryos or newborn pups was never determined in this study resulting in a random mix of both sexes in all related experiments.

The mice were group housed before the surgical procedure (up to 5 female mice per cage) and single-housed after the procedure until the end of the trial, with room temperature controlled at 21–22°C, and an artificial 12 h light:dark cycle (lights off at 6:00 pm). All animals were given food and water *ad libitum* throughout the experiment.

Cell cultures
Primary meningeal cells were obtained from cortical meninges of E17 rat embryos and digested with 0.05% trypsin-EDTA (25300054, Gibco) at 37°C for 15 min. Cells were dissociated by pipetting, plated, and cultivated in MEM containing 10% fetal bovine serum (FBS) as described previously.[103] Primary astrocytes and hippocampal neurons from E17 rat embryos were isolated and cultured as described previously.[138] Cells from all isolated embryos were pooled, therefore, cultures always contained a random mixture of both sexes.

METHOD DETAILS

Plasmids and transfections
Plasmids used in vitro
Pβactin vector[128] was a kind gift from C. C. Hoogenraad (University Utrecht). pEGFP-Centrin2 and pCS-Centrin2-tdTomato[36] were a kind gift from R. W. Köster (Technische Universität Braunschweig). Both vectors contain a coding sequence (CDS) of *Danio rerio* centrin 4 (XM_002667181.6). Mismatch in naming arose likely from the higher homology of *Danio* Centrin 4 to human Centrin 2 than to human Centrin 4, and propagated through several databases including Uniprot (B1P0R9_DANRE). For continuity, we have kept the names of the vectors and the protein name as in the original publication. PmNeonGreen-N1 and C1 were purchased from Gentaur Europe BVBA (Kampenhout, Belgium; Shaner et al.[139] mNeonGreen CDS was amplified by PCR using forward 5'-CGAG GATCCCGCCACCATGGTGAGCAAGGGCGAGGAG and reverse 5'-CGAGCGGCCGCCTATTACTTGTACAGCTCGTCCATGCC CATC primers. mNeonGreen was inserted in place of mCherry in pEB3-mCherry[130] as a BamHI/NotI fragment. The whole EB3-mNeonGreen cassette was subcloned as a NheI/NotI fragment in the pβactin vector, resulting in pβactin-EB3-mNeonGreen. mOrange2-EB3-7 (Addgene plasmid #57953, Shaner et al.[129] was a gift from Michael Davidson and mEGFP-RhoA-C1 (identical

to the Addgene plasmid #29674; Murakoshi et al.[140] was a gift from Ryohei Yasuda (Max Planck Florida Institute for Neuroscience). These served as sources of fluorescent protein CDSs.

Pβactin vector and pAcGFP-C1 (Clontech) were cut by NheI and XbaI and a cassette containing AcGFP and the multicloning site from pAcGFP-C1 was inserted into linearized pβactin vector resulting in pβactin-AcGFP-C1. Tandem (Td)-mCherry CDS was amplified by PCR from pKIF5C(1-560)-2xmCherryALTv2[131] - a kind gift from K. Verhey (University of Michigan), using forward 5'-ATAGCTAGCAGCCACCATGGTCAGCAAAG and reverse 5'-GGTCAGATCTCTTGTACAGCTCGTCCATTC primers and inserted as NheI/BglII fragment into linearized pβactin-AcGFP-C1 and resulting in pβactin-td-mCherry-C1. mNeonGreen CDS was subcloned using NheI/BglII into linearized pβactin-AcGFP-C1 resulting in pβactin-mNeonGreen-C1. mOrange2 was amplified from mOrange2-EB3-7 using forward 5'-ATAAGCTAGCAGCCACCATGGTGAGCAAGGGCGAGGAG and reverse 5'- ACTGCTT AGATCTGAGTCCTGACTTGTACAGCTCGTCCATGCC primers and subcloned NheI/BglII into linearized pβactin-AcGFP-C1, resulting in pβactin-mOrange2-C1.

A cassette encoding mouse γ-tubulin 1 tagged with TagRFP was excised from pmTubg1-TagRFP[141] using NheI/NotI and inserted into linearized pβactin, resulting in pβactin-mTubg1-TagRFP. TagRFP CDS was spliced out using SalI/NotI and replaced by mNeongreen that was previously prepared by PCR using forward 5'-TACAGTCGACGGAAGTGGTGGATCCATGGTGAGCAAGGGCGAG and reverse 5'-AATCTGATGCGGCCGCTTACTTGTACAGC primers, with pmNeonGreen-N1 as a template. The resulting plasmid was named pβactin-Tubg1-mNeonGreen.

pβactin-mTubg1-TagRFP was further used for preparation of plasmids containing a longer linker in front of the C-terminal fluorescent protein, necessary for a functional fusion of Nedd1 with mOrange2. The linker encoding a protein sequence VDGSKLGGGSASGGSGSRS was prepared by sequential PCR. In the first round, forward 5'-GCATCAGGCGGAAGCGGAAGCA GATCTATGGTGAGCAAGGGCGAG and reverse 5'-AATCTGTTGCGGCCGCTTACTTGTACAGCTCGTCCATGCC primers were used with mEGFP-RhoA-C1 as a template were used. The PCR product was purified and used as a template for the second round of PCR with the same reverse and a new forward 5'-TAAGTCGACGGCAGCAAGCTTGGTGGAGGCAGCGCATCAGGCGGAAGCG GAAGC primer. The PCR product of the second round was purified, cut by SalI/NotI and inserted into pβactin-mTubg1-TagRFP linearized by the same restriction enzymes and therefore lacking the TagRFP CDS. The resulting vector containing the newly designed linker was named pβactin-mTubg1-mEGFP and was used as a backbone for the preparation of various other vectors as indicated in the following paragraphs.

Total RNA was isolated from cultured rat meningeal cells using a RNeasy Mini kit (Sigma-Aldrich) according to manufacturer's instructions. 1 μg of isolated RNA served as a template for a reverse transcription with 400 ng oligo(dT)$_{18}$ primers (#SO132, Thermo Fisher Scientific) and 250 U SuperScript III reverse transcriptase (18080093, Thermo Fisher Scientific). Next, the sample was treated with 2 U RNAse H (M0297S, NEB) and heat inactivated at 65°C. The resulting cDNA was used as a template for PCR amplification of Cdk5rap2 coding sequence using forward 5'- GTGCCACCTCTTTGTGTTCA and reverse 5'- TTAGCTGAAAGCTCTTCTCATGA primers. A new splice variant of the full-length rat Cdk5rap2 (GenBank: MF541099) was subcloned into pJet1.2/blunt using CloneJet PCR Cloning kit (K1231, Thermo Fisher Scientific, K1231) resulting in pJet1.2-rCdk5rap2. Full-length Cdk5rap2 was subcloned into pβactin-td-mCherry-C1 as a BglII/SalI fragment.

Cdk5rap2-CTD (C-CTD) coding sequence encoding AA 1736-1903 from a rat Cdk5rap2 isoform (GenPept: XP_006238335.1) and corresponding to previously described AA 1726-1893 in the human homolog[54] was amplified by PCR from full-length rat Cdk5rap2 using forward 5'-ACAAGTCCGGACT CAGATCTCACATGCTGTGCCTGATTG and reverse 5'-CCCGCGGTACCGTCGACTCATGAGCCCGGTCTGCTG primers and subcloned into pβactin-AcGFP-CI as a BglII/SalI fragment. A red color version of Cdk5rap2-CTD was created by swapping AcGFP for td-mCherry or mOrange2 as NheI/BglII fragment.

To create Cdk5rap2-CTDΔCBD (C-CTDΔCBD) we first amplified coding sequences corresponding to AA 1736-1871 and AA 1880-1903 of XP_006238335.1 by PCR. We used forward 5'-ACAAGTCCGGACTCAGATCTCACATGCTGTGCCTGATTG and reverse 5'-AGGTTTCCCCTCAACTGATCAAAGATGATTTTCTCC primers for amplification of AA 1736-1871 CDS. For AA 1880-1903 CDS forward 5'-TTGATCAGTTGAGGGGAAACCTGGAGCTCAGG and reverse CCCGCGGTACCGTCGACTCATGAGCCCGGTCTGCTG primers were used. Second, we mixed the PCR products from previous reactions and used them as templates of a new PCR using only the outer primers. The resulting C-CTDΔCBD was inserted as a BglII/SalI fragment into pβactin-AcGFP-CI.

CM1 domain of rat Cdk5rap2 corresponding to AA 52-100 in XP_006238335.1 was amplified by PCR using forward 5'-ATTGC TAGCGCCACCATGGTCTCTCCCACCAGAG reverse 5'-TACGTCATTGCTAGCGAGTAGATGTGCTCTGTGG primers and full-length rat Cdk5rap2 (GenBank: MF541099) as a template. The PCR product was then inserted into pJet1.2/blunt resulting in pJet-rCM1. pJet-rCM1 served as a template for site-directed mutagenesis using sense 5'-TGAGCTGAAGAAGGAGAACGCCAATC TAAAGCTCCGGATC and anti-sense 5'-GATCCGGAGCTTTAGATTGGCGTTCTCCTTCTTCAGCTCA primers (200 nM each) and 2.5 U PfuTurbo polymerase (QuikChange Site-Directed Mutagenesis Kit; #200518, Agilent Technologies). The resulting plasmid encoding rCM1 carrying a F75A mutation was named pJet-F75A.

The same rat meningeal-derived cDNA preparation described above was used as a template for PCR amplification of full-length rat Nedd1 using forward 5'-TCCCACGCTTGAGAGGCTCA and reverse 5'-TCAAGGTGTCCAGAGGCTTCAGA primers. The PCR product was subcloned into pJet1.2/blunt using CloneJet PCR Cloning kit (K1231, Thermo Fisher Scientific, K1231) resulting in pJet-rNedd1. Sequencing revealed a new variant of rat Nedd1 (GenBank: MT415945) encoding a previously predicted Nedd1 protein with Pro547 (Uniprot: D3ZAH3_RAT). This full-length rat Nedd1 was used as a template for PCR using 5'-ACTCGCTAGCAGCCAC

CATGCAGGAAAACCTCAG and reverse 5'-TACACTCGAGGAGGCTTGAGAAGTGGG primers. The PCR product was subcloned using NheI/XhoI sites into pβactin-Tubg1-mEGFP and pβactin-Tubg1-mNeonGreen backbones in the place of Tubg1 CDS that was removed using NheI/SalI. The resulting plasmids were named pβactin-Nedd1-mEGFP and pβactin-Nedd1-mNeonGreen, respectively. mOrange2 CDS was amplified by PCR using forward 5'-TACAGATCTATGGTGAGCAAGGGCGAGGAG and reverse 5'- AATCTGTTGCGGCCGCTTACTTGTACAGCTCGTCCATGCC primers and EB3-mOrange2-7 as a template; using BglII/NotI replaced mEGFP CDS in pβactin-Nedd1-mEGFP, resulting in pβactin-Nedd1-mOrange2.

To create Nedd1 fusions with CM1 domains, pβactin-Nedd1-mOrange2 was linearized by BglII and NotI excising mOrange2 CDS. mOrange 2 was newly amplified by PCR using forward 5'-TACAGATCTATGGTGAGCAAGGGCGAGGAG reverse 5'-TTGTATC GATGCTTCCACCTGTGCCAGACTTGTACAGCTCGTCCATGC primers and pβactin-mOrange2-C1 as a template. Rat CM1 domain of Cdk5rap2 and its F75A mutated version were amplified based on templates encoding AA 52-100 of XP_006238335.1 as described above using forward 5'-GCTAGATCGATAAGGTCTCTCCCACCAGAG and reverse 5'-AATCTGTTGCGGCCGCTTAGTAGAT GTGCTCTGTGGG primers. CM1 domain from human CDK5RAP2 was amplified from pRcCMV-Cep215 (Nigg CW493) - a gift from Erich Nigg (Addgene plasmid #41152; Graser et al.[142]) - by PCR using forward 5'- GCTAGATCGATACAG TGTCTCCCACCAG and reverse 5'-AATCTGTTGCGGCCGCTTAGTAGATATGTTCAGTGGGG primers. All PCR products were cut by respective restriction enzymes (BglII/ClaI for mOrange2 and ClaI/NotI for CM1 variants) and inserted into pβactin-Nedd1 (BglII/ NotI) giving rise to pβactin-Nedd1-mOrange2-rCM1, pβactin-Nedd1-mOrange2-F75A and pβactin-Nedd1-mOrange2-hCM1.

Full length mouse Akna was amplified from pDCx-Akna-IRES-EGFP[67] using forward 5'-TAAGCTAGCAGCCACCATGGCCAGCTC AGGGGCAAAG and reverse 5'-TTAGTCGACGAAAAGGCAGGAGCCTCGCAGG primers and inserted in the place of Tubg1 in pβactin-Tubg1-mEGFP by NheI/SalI giving rise to pβactin-Akna-mEGFP. mOrange2 CDS was put in place of mEGFP using BglII/NotI resulting in pβactin-Akna-mOrange2.

Total RNA was isolated from cultured rat meningeal cells using a RNeasy Mini kit (Sigma-Aldrich) according to manufacturer's instructions. 3 μg of isolated RNA served as a template for a reverse transcription with 2 pmol of an Akap9 gene specific primer 5'-CTCCAGTTTGTCTTCATGTG and 300 U SuperScript III reverse transcriptase (18080093, Thermo Fisher Scientific) according to manufacturer's instructions. Next, the sample was treated with 2 U RNAse H (M0297S, NEB) and then heat inactivated at 65°C. Rat Akap9 full length coding sequence was then amplified from the Akap9 cDNA by PCR using forward 5'-TTTCCTCTCCACTGCGTCCCAG and reverse 5'-CAGTTTGTCTTCATGTGCTGCTG primers. The PCR product of a predicted size of approx. 12 kb was purifed from gel and amplified by PCR using another set of forward 5'-TCTTTCCTCTCCACTGCGTC and reverse 5'-GGATTATCTCCTCATGCCAA primers. The PCR product was purified and subjected to the addition of dA overhangs by Taq polymerase (M0267L, NEB). The reaction product was purified on Crystal violet-stained gel and inserted into pCR-XL-TOPO (K4700-20, Thermo Fisher Scientific) according to manufacturer's instructions, resulting in pCR-XL-rAkap9. Sequencing revealed that XM_006236023.3 transcript variant was amplified. Of note, for successful transformation of One Shot® Cells (TOP10), it was necessary to use electroporation (Bacterial Program #3 on Nucleofector II; cuvettes #VKA-1001; Lonza) and to grow transformed bacteria at no more than 28°C for two days and with 30 μg/ml kanamycin on LB plates for full length plasmid production.

Akap9-dis AA sequence in the rat homolog was inferred from the homologous sequence in human AKAP9 based on the fragment designated AK1B in Hurtado et al.[62] Sequence encoding AA 128-425 was amplified by PCR using forward 5'- TTAC TATCCGGAAGTGGAGGAAGTATGGGGGAAAACGAGTTG and reverse 5'-CCTCCGTCGACTCGTCAAAGCTCCTCTATCTGAGA CATG primers form full length rat Akap9 and inserted as BspEI/SalI into pAcGFP-C1 (Clontech). AcGFP-Akap9-dis cassette was then cut by NheI/SalI and inserted into pβactin vector linearized using the same restriction enzymes resulting in pβactin-AcGFP-128-425-Akap9.

PACT domain[65] of Akap9 was amplified by PCR using forward 5'-GTAGGATCCGCTGACATCGAAGCC and reverse 5'-GTGAAGCTTGTTATCTCCTCATGCCAA primers from full length rat Akap9 and inserted as BamHI/HindIII into pAcGFP-C1 (Clontech).

For creating PACT-hCM1 fusion, PACT CDS was amplified by PCR using forward 5'-TAAGCTAGCAGCCACCATGGCTGACATCG AAGCCATAATCG and reverse 5'-CAGAAGCTTTCTCCTCATGCCAAAATGAAATTGAG primers and inserted in the place of Nedd1 CDS in pβactin-Nedd1-mOrange2-hCM1 by NheI/HindIII giving rise to pβactin-PACT-mOrange2-hCM1.

EGFP-NEDD1-gTBD (N-gTBD) (unpublished) was a kind gift from Pavel Dráber (IMG of the ASCR, Prague). Preparation was as follows: a fragment encoding AA 572-660 in a human NEDD1 isoform (NP_001128648.1) was amplified by PCR from NM_152905.2 (SC100748, Origene) using forward 5'-CgaattcTAGCCGACAGCATTGGA and reverse 5'-GGATCCTCAAAA GTGGGCCCGTAA primers. The resulting fragment was treated with Taq polymerase and then inserted into pCR2.1 using TOPO™ TA Cloning™ Kit (450641, Thermo Fisher Scientific). Coding sequence for NEDD1-gTBD was cut out by EcoRI/BamHI and inserted into pEGFP-C2 (Clontech). For strong expression in neurons, the whole EGFP-NEDD1-gTBD cassette was subcloned using NheI/BamHI into pβactin vector resulting in pβactin-EGFP-NEDD1-gTBD. To create an mOrange2-tagged version, mOrange2 was amplified by PCR using forward 5'-ATAAGCTAGCAGCCACCATGGTGAGCAAGGGCGAGGAG and reverse 5'-GCACTGCTTAG ATCTGAGTACTTGTACAGCTCGTCCATGCC and switched for EGFP as NheI/BglII fragment.

To construct the pβactin-Halo-Tag used as control, Halo-Tag was amplified from pENTR4-HaloTag, a gift from Eric Campeau (Addgene Plasmid #29644), with primers Halo forward: 5'-CTCTGTTCCTCCGCAGCCCCCAAGCTAGCATGGCAGAAATCGG TACTGG-3' and Halo reverse: 5'-CGACTGCAGAATTCGAAGCTTCTAGATTAGCCGGAAATCTCGAGCG-3' and cloned into pβactin plasmid backbone. pCAG-Halo-Tag-Akap9-128-425 was constructed as follows; two fragments were produced, Halo-Tag was

amplified from pβactin-Halo-Tag with primers PstI-Halotag forward 5'-GGTCGACGACCTGCAGGCCACCATGGCAGAAATCGG TACTG-3' and Halo-Tag linker reverse 5'-ACCTCCACCACCTCCGGAGCCGGAAATCTCGAGCGTC-3' and Akap9(128-425) was amplified from pβactin-AcGFP-128-425-Akap9 with primers Linker-AKAP9 fw 5'-TCCGGAGGTGGTGGAGGTATGGGGGAAAAC GAGTTG-3' and AKAP9 rv 5'-GGCTGATCAGCGAGCTCTCAAAGCTCCTCTATCTG-3'. Both PCR fragments were ligated by Gibson assembly into a PstI/SacI-linearized pCAG-EGFP vector derived from pCAG-loxSTOPlox-Lyn-EGFP (Addgene plasmid #133922; Dupraz et al.[14]).

To prepare pCAG-mScarlet-Giantin, the loxSTOPlox cassette of a pCAG-loxSTOPlox-ZsGreen was released by SalI/SacI digestion and replaced by Gibson assembly with a mScarlet-Giantin fragment amplified from pmScarlet-H_Giantin_C1, a gift from Dorus Gadella (Addgene plasmid #85049; Binder et al.[133]). with primers: SalI-Giantin fw 5'-GACTCACTATAGGGGGTCGACGACCTG CAGGCCACCATGGTGAGCAAGG-3' and SacI-Giantin rv 5'-GGCTGATCAGCGAGCTCCTATAGATGGCCCGTAAAAC-3' resulting in pCAG-mScarlet-Giantin.

Plasmid used in vivo

To attain *in vivo* neuron-specific expression of mOrange2-Cdk5rap2-CTD (C-CTD), mOrange2-NEDD1-gTBD (N-gTBD), Nedd1-mOrange2-rCM1 and Akna-mOrange2, Cre/lox-dependent neurons-specific self-activating plasmid were generated as follows. First, a tubulin-α-1-iCre-polyA and tubulin-α-1-Dre-polyA cassettes were amplified from pTα1-iCre and pTα1-Dre (Addgene plasmids #133924 and #133925 respectively; Dupraz et al.[14] with primers forward LSL-Rb-globin_pA 5'-GCGATGAATAAAT GAAAGCTGTCGAGGGATCTTCATAAG-3' and reverse LSL-Tα1-BamHI 5'-TCCGGATCAGCTTGATGGGGATCATTCCGTATTAG GAGGG-3'. The amplified cassettes were cloned into a HindIII/BamHI-linearized pCAG-loxSTOPlox-Lyn-EGFP (Addgene plasmid #133922; Dupraz et al.[14]) using Gibson assembly (HiFi DNA Assembly Cloning Kit; New England Biolabs) resulting in a pCAG-lox-inv[Tα1-iCre-pA]-lox-Lyn-EGFP and pCAG-lox-inv[Tα1-Dre-pA]-lox-Lyn-EGFP. In these vectors, the inverted Tα1-iCre-polyA and Tα1-Dre-polyA expression cassettes act as a STOP cassette for Lyn-EGFP expression replacing the original 3xsv40-polyA STOP cassette. Next, mOrange2-Cdk5rap2-CTD (CCTD), mOrange2-N-gTBD (N-gTBD), Nedd-1-mOrange2-rCM1 and Akna-mOrange2 were amplified from their respective pβactin-based formats introduced above using primers forward NewST-PstI_85-103 5'-TAGGTCCCTCGACCTGCAGCCTCCGCAGCCCCCAAGCTA-3' and reverse NewST-PstI_85-103rv 5'-GTCGAGGCTGATCAGC-GAGCTCTCATTACTTATCTAGA-3'. The amplified cassettes (mOrange2-N-gTBD, Nedd-1-mOrange2-rCM1 and Akna-mOrange2) were inserted by Gibson assembly into PstI/SacI linearized pCAG-lox-inv[Tα1-iCre-pA]-lox-Lyn-EGFP replacing Lyn-EGFP and resulting in pCAG-lox-inv[Tα1-iCre-pA]-lox-mOrange2-NEDD1-gTBD, pCAG-lox-inv[Tα1-iCre-pA]-lox-Nedd-1-mOrange2-rCM1 and pCAG-lox-inv[Tα1-iCre-pA]-lox-Akna-mOrange2 whereas the amplified mOrange2-C-CTD cassette was inserted by Gibson assembly into linearized PstI/SacI pCAG-lox-inv[Tα1-Dre-pA]-lox-Lyn-EGFP replacing Lyn-EGFP and resulting in pCAG-lox-inv[Tα1-Dre-pA]-lox-mOrange2-Cdk5rap2-CTD. Following the same strategy, pCAG-lox-inv[Tα1-Dre-pA]-lox-mOrange2-NEDD1-gTBD and pCAG-lox-inv[Tα1-Dre-pA]-lox-Akna-mOrange2 were prepared. These plasmids self-activate in neuronal cells and are transfected along with either a Cre/lox-dependent reporter pCAG-loxSTOPlox-ZsGreen [a gift from Pawel Pelczar (Addgene plasmid #51269; Hermann et al.[143]], pCAG-loxSTOPlox-Lyn-EGFP or a dual Cre/lox-Dre/rox co-transfection reporter (see next) in the case of co-transfection with the plasmids containing N-gTBD and C-CTD CDS as described before. To construct a true co-transfection reporter, we first generated a pCAG-DIO-basic plasmid as follows. Synthetic oligo pairs FlexA-s/FlexA-as and FlexB-s/FlexB-as (see primer table) were hybridized and used as a template for the amplification of the entire dsDNA fragment via overlapping PCR with primers FlexA-s fw 5'-ACCGGCGGCTCTAGACCAGGC-3' and FlexB-as rv 5'-CATGGTGGCCTGCAGCTTGAT-3'. The resulting DNA fragment containing opposed lox2272/lox sites (DIO) flanking NheI and MluI restriction sites was inserted by Gibson assembly into XbaI/PstI linearized pCAG-loxSTOPlox-LynEGFP plasmid (Addgene Plasmid 133922; Dupraz et al.[14]), replacing the loxSTOPlox cassette. The resulting pCAG-DIO-base-LynEGFP was linearized with PstI and NotI to release LynEGFP, blunted and religated (eliminating PstI and NotI sites) resulting in pCAG-DIO-base. A roxSTOProx-ZsGreen-bGH_polyA cassette was amplified from pCAG-roxSTOProx-ZsGreen - a gift from Pawel Pelczar (Addgene plasmid # 51274, Hermann et al.[143]) - with primers forward Flex-invRSR-ZsG 5'-CTAGAGCAACTAGCTAGCGAGGTTCTTTCCGCCTCAGAAG-3' and reverse Flex-invRSR-ZsG 5'-GCCACCA TAGGCGTGACGCGTAGGGGGTCGACCCGCCACC-3' and cloned inverted by Gibson assembly in a MluI-linearized pCAG-DIO-basic plasmid resulting in pCAG-DIO-inv[roxSTOProx-ZsGreen-bGH]. From this vector, the whole DIO-RSR-ZsGreen-bGH cassette was amplified with primers pBA_dio-rsr-common forward

5'-CTCCGCAGCCCCCAAGCTAGCGTTCGGCTTCTGGCGTGT-3' and

pBA_dio-rsr-common reverse

5'-CCCGCGGTACCGTCGACCGCTTGATATCGAATTC-3' and ligated by Gibson assembly into a pβactin-mOrange2-C1 previously linearized with NheI/SalI to release mOrange2 resulting into pβactin-inv[roxSTOProx-ZsGreen-bGH]. This reporter, which only expresses ZsGreen in the presence of both Cre and Dre, was used to report co-expression by pCAG-lox-inv[Tα1-Cre-pA]-lox-mOrange2-NEDD1-gTBD and pCAG-lox-inv[Tα1-Dre-pA]-lox-mOrange2-Cdk5rap2-CTD.

Control plasmids were based on Dre/Rox recombination to avoid cross-reaction with the Cre/lox-based plasmids described above and were designed as follows. A pCAG-lox-roxSTOProx-tRFP-pA-lox-ZsGreen-pA vector (Addgene plasmid #175438; Alfadil et al.[132]) was linearized with EcoRI/XhoI and religated removing ZsGreen-pA resulting in pCAG-lox-roxSTOProx-tRFP-pA-lox. This control vector shows Dre-dependent tRFP expression and, importantly, is inactivated in the presence of Cre. A similar control reporter was generated for Lyn-Scarlet expression as follows. The pCAG-lox-roxSTOProx-tRFP-pA-lox was linearized

with BglII/SacI removing STOProx-tRFP which was replaced by a BglII/SacI fragment encoding STOProx-Lyn-mScarlet and resulting in pCAG-lox-roxSTOProx-lyn-mScarlet-pA-lox. Dre-dependent control plasmids were co-electroporated with pTα1-Dre.

The dual Cre/Dre vector pβactin-DIO-inv[roxSTOProx-EB3-mNeonGreen-bGH] was constructed as follow. First, a roxSTOProx-LynEGFP-bGH fragment was amplified from pCAG-roxSTOProx-LynEGFP (Addgene plasmid #133923; Dupraz et al.[14]) with primers Flex-invRSR-ZsG forward

5'-CTAGAGCAACTAGCTAGCGAGGTTCTTTCCGCCTCAGAAG-3' and

Flex-invRSR-ZsG reverse

5'-GCCACCATAGGCGTGACGCGTAGGGGGTCGACCCGCCACC-3' and ligated by Gibson assembly into pCAG-DIO-basic linearized by NheI/MluI digestion resulting in pCAG-DIO-RSR-LynEGFP. pCAG-DIO-inv[roxSTOProx-LynEGFP-bGH] was linearized with PstI and SacI releasing LynEGFP which was replaced by a PstI-digested EB3-mNeon fragment amplified from a pCMV-EB3-mNeon with primers CMV forward 5'-CGCAAATGGGCGGTAGGCGTG-3' and mGFP,NeonGFP-SacI reverse 5'-CAGTCGAGGCTGATCAGCGAGCTCTTACTTGTACAGCTCGTCCAT-3' resulting in pCAG-DIO-inv[roxSTOProx-EB3-mNeonGreen-bGH]. From this las vector, the whole DIO-RSR-EB3-mNeonGreen cassette was amplified with primers pBA_dio-rsr-common forward

5'-CTCCGCAGCCCCCAAGCTAGCGTTCGGCTTCTGGCGTGT-3' and

pBA_dio-rsr-common reverse

5'-CCCGCGGTACCGTCGACCGCTTGATATCGAATTC-3' and ligated by Gibson assembly into a pβactin-mOrange2-C1 previously linearized with NheI/SalI to release mOrange2 resulting into pβactin-DIO-inv[roxSTOProx-EB3-mNeon-bGH]. To generate the pCAG-lox-inv[Tα1-iCre-pA]-lox-mNeonGreen-hCentrin1, we first produced a pCAG-lox-inv[Tα1-iCre-pA]-lox-mCherry-hCentrin1. A pCAG-lox[inv Tα1-iCre-pA]lox-LynEGFP was diggested with PstI/SacI releasing LynEGFP and replaced with a mCherry-Centrin1 amplified from pIRES Centrin1-mCherry - a gift from Matthieu Piel (Addgene plasmid #64338) - with primers ST-PstI_mCherry forward

5'-TAGGTCCCTCGACCTGCAGGCTACCGGTCGCCACCATGGTG-3' and New_ST-SacI_hCentrin reverse 5'-GTCGAGGCTGATCAGCGAGCTCTCAGTAAAGGCTGGTCTTC-3' resulting in pCAG-lox-inv[Tα1-iCre-pA]-lox-mCherry-hCentrin1. Next, linker-hCentrin1 was amplified from this vector with primers Linker-hCentrin1 forward

5'-TCCGGACTCAGATCTCGAGCTCAA-3' and New_ST-SacI_hCentrin reverse 5'-GTCGAGGCTGATCAGCGAGCTCTCAGTAAAGGCTGGTCTTC-3'; in parallel, a mNeonGreen was amplified from pmNeonGreen-C1 with primers ST-PstI_mScarlet_orange forward 5'-TAGGTCCCTCGACCTGCAGGCCACCATGGTGAGCAAGGG-3' and mScarlet_orange-linker reverse 5'-TTGAGCTCGAGATCTGAGTCCGGACTTGTACAGCTCGTCCAT-3'. Both mNeonGreen and linker-hCentrin1 fragments were ligated by Gibson assembly into a linearized pCAG-lox-inv[Tα1-iCre-pA]lox-LynEGFP backbone where LynEGFP was released by PstI/SacI digestion resulting in pCAG-lox-inv[Tα1-iCre-pA]lox-mNeonGreen-hCentrin1. To generate the pCAG-rox-inv[Tα1-iCre-pA]-rox-mNeonGreen-hCentrin1 we first generated a pCAG-rox-inv[Tα1-iCre-pA]-rox-LynEGFP backbone as follows. Tα1-iCre-pA was amplified from pTα1-iCre with primers:

LSL-Rb-globin_pA forward 5'-GCGATGAATAAATGAAAGCTGTCGAGGGATCTTCATAAG-3' and

LSL-Ta1-BamHI reverse 5'-TCCGGATCAGCTTGATGGGGATCATTCCGTATTAGGAGGG-3' and inserted replacing the released STOP signal into a HindIII/BamHI linearized pCAG-roxSTOProx-LynEGFP backbone (Addgene plasmid #133923; Dupraz et al.[14]) resulting in pCAG-rox-inv[Tα1-iCre-pA]rox-LynEGFP. Next, this vector was linearized with PstI/SacI releasing LynEGFP which was replaced by a NeonGreen-hCentrin1 insert amplified from pCAG-lox-inv[Tα1-iCre-pA]lox-mNeonGreen-hCentrin1 with primers ST-PstI_mScarlet_orange forward 5'-TAGGTCCCTCGACCTGCAGGCCACCATGGTGAGCAAGGG-3'

New_ST-SacI_hCentrin reverse 5'-GTCGAGGCTGATCAGCGAGCTCTCAGTAAAGGCTGGTCTTC-3' and digested with PstI before Gibson assembly, resulting in pCAG-rox-inv[Tα1-iCre-pA]-rox-mNeonGreen-hCentrin1. A 2xHA-hCentrin1 fragment was generated through three amplification rounds from pCAG-loxP-inv[Tα1-iCre-pA]-loxP-mCherry-hCentrin1 using the same reverse primer New_ST-SacI_hCentrin 5'-GTCGAGGCTGATCAGCGAGCTCTCAGTAAAGGCTGGTCTTC-3' and alternating different forward primers in each successive reaction, first Linker-hCentrin forward 5'-GACTATGCAGGAAGTTCAGGAGGTTCTAGTGGTAC CATGGCTTCCGGC-3', second Flanking-2HA forward 5'-TACGCTGGCTATCCCTATGACGTCCCGGACTATGCAGGAAGTTCAG GAG-3' and third 1-Flanking-2HA forward 5'-AGGTCCCTCGACCTGCAGCCACCATGTACCCATACGATGTTCCAGATTACGCT GGCTATCCC-3'. The resulting 2xHA-hCentrin1 fragment was ligated into into a linearized pCAG-lox-inv[Tα1-iCre-pA]lox-LynEGFP backbone where LynEGFP was released by PstI/SacI digestion resulting in pCAG-lox-inv[Tα1-iCre-pA]lox-2xHA-hCentrin1. Next, to generate a pCAG-lox-inv[Tα1-iCre-pA]-lox-2xHA-128-425-Akap9, pCAG-lox-inv[Tα1-iCre-pA]lox-2xHA-hCentrin1 is linearized with KpnI/SacI releasing hCentrin1 which is replaced by an Akap9(128-425) fragment amplified from pCAG-HaloTag-AKAP9(128-425) with primers 2xHA-AKAP9mut forward 5'-GGAGGTTCTAGTGGTACCTCCGGAGGTGGTGGAGGT-3' and

AKAP9 reverse 5'-GGCTGATCAGCGAGCTCTCAAAGCTCCTCTATCTG-3' resulting in pCAG-lox-inv[Tα1-iCre-pA]lox-2xHA-128-425-Akap9. The pCAG-lox-inv[Tα1-Dre-pA]-lox-2xHA-CAMSAP3 was generated as follows. A doublet of HA-tags was amplified from a custom-made pCMV-3xHA-C1 plasmid with primers 2-Flank-2HA-Camsap forward 5'-AGGTCCCTCGACCTGCAGCTG CAGGCCACCATGTACCCATACGATGTTCC-3' and 2xHA-tag-linker reverse 5'-ACTAGAACCTCCTGAACTTCCACCTGCA TAGTCCGGG-3'; in parallel, Camsap3 was amplified from pβactin-Halo-CAMSAP3 - a gift from Max Schelski (Schelski and Bradke[144]) - with primers Linker-CAMSAP3 forward

5'-GACTATGCAGGAAGTTCAGGAGGTTCTAGTATGGTGGAAGC-3' and CAMSAP3-SacI reverse 5'-GTCGAGGCTGATCAGC GAGCTCTTATTTGGGGGTACCGCCAC-3'. These two fragments were inserted by Gibson assembly - replacing the released

LynEGFP- from PstI/SacI-linearized pCAG-lox-inv[Tα1-Dre-pA]-lox-Lyn-EGFP and resulting in pCAG-lox-inv[Tα1-Dre-pA]-lox-2xHA-Camsap3. A N-Cadherin-2xHA insert was generated as follows: N-Cadherin was amplified from N-Cadherin-EGFP - a gift from Valeri Vasioukhin (Addgene plasmid #18870; Nechiporuk et al.[145]) - with primers

NCadher-2HA_PstI forward

5'-GGTCCCTCGACCCTGCAGGCCACCATGTGCCGGATAGC-3' and

1-NCadher-2HA reverse 5'-GGATAGCCAGCGTAATCTGGAACATCGTATGGGTAGAGCTCGTCGTCACCACCGCC-3'. Next, the PCR product was re amplified maintaining the same forward primer but introducing a new reverse 2-NCadher-2HA 5'-GAGGCTGATCAGCGTCATGCATAGTCCGGGACGTCATAGGGATAGCCAGCGTAAT-3'. The resulting PCR product, as for 2xHA-Camsap3 before, was inserted by Gibson assembly into a PstI/SacI-linearized pCAG-lox-inv[Tα1-Dre-pA]-lox-Lyn-EGFP backbone resulting in pCAG-lox-inv[Tα1-Dre-pA]-lox-N-Cadherin-2xHA.

Q5® Hot Start High-Fidelity DNA Polymerase (M0493S, NEB) was used for all PCR reactions. All vectors were verified by sequencing.

E17 rat hippocampal neurons were transfected before plating with Amaxa nucleofector system (Lonza) using program O-003. For live imaging experiments, 1.5 to 5×10^5 neurons were transfected per reaction. For immunofluorescence, 3×10^5 to 2×10^6 neurons were transfected per reaction. The total amount of transfected DNA was kept under 5 μg per reaction.

Immunocytochemistry

To visualize the Halo Tag, a stock solution of Janelia Fluor® Halo-Tag® ligand (646) (Promega) in DMSO (0.14 μg/μl) was diluted 1:1000 in conditioned N2 media to the final concentration. Cells were incubated for 30 min at 37°C and in the presence of 5% CO_2. Subsequently, cells were either fixed with -20°C methanol at -20°C for 10 min.

To stain for centrosomal proteins Cdk5rap2, centrin, γ-tubulin, Pericentrin, and Akap9, neurons were fixed with -20°C methanol supplemented with 1 mM EGTA at -20°C for 10 min.

For evaluation of MT regrowth from the centrosome, neurons were fixed using 37°C warm PHEM buffer (60 mM Pipes, 25 mM Hepes, 5 mM EGTA and 1 mM $MgCl_2$, pH 6.9) containing 0.2% glutaraldehyde, 3.7% paraformaldehyde, 3.7% sucrose and 0.15% Triton X100 (adapted from Smith[146]) at room temperature for 15 min, washed thoroughly with phosphate buffered saline (PBS) and then quenched with 0.1 M glycine in Tris-buffered saline for 10 min followed by extensive washing in PBS.

Assessment of neuronal morphology was performed on neurons fixed in 37°C 4% paraformaldehyde (PFA)/4% sucrose in PBS at room temperature for 15 min. After extensive washing with PBS, samples were quenched in 50 mM ammonium chloride in PBS for 10 min. The cells were then permeabilized with 0.1% Triton X100 for 3 min.

For evaluation of centrosome ablation, neurons were fixed with 37°C 4% PFA/4% sucrose for 1 min and then immediately post-fixed with -20°C methanol supplemented with 1 mM EGTA at -20°C for 5 min. After extensive washing with PBS, samples were quenched in 50 mM ammonium chloride in PBS for 10 min.

Neurons were blocked in a solution containing 2% FBS (Invitrogen), 2% bovine serum albumin (Sigma-Aldrich), and 0.2% fish gelatin (Sigma-Aldrich) dissolved in PBS at room temperature for 1 h. Subsequently, cells were incubated with primary antibodies diluted in 10% blocking solution at room temperature for 1 h or at 4°C overnight. Primary antibodies for Cdk5rap2 (ABE236, 1:2500), Tau-1 (MAB3420, 1:750), centrin (04-1624, 1:400) and Map2 (AB5622) were from Millipore. Anti-βIII-tubulin (T2200, 1:3000), and anti-γ-tubulin (T6557, 1:2500) antibodies were from Sigma. Anti-Pericentrin (ab4448, 1:1000) and anti-Cep135 (ab75005; 1:300) were from Abcam. Anti-NEDD1 (GTX32744, 1:80) was from GeneTex. Anti-RFP (recognizing mOrange2) was from Rockland (600-401-379, 1:800). anti-Akap9 (NBP1-89166; 1:100) was from Novus and anti-GM130 (BD610823; 1:750) from BD Biosciences. Rat monoclonal anti-Akna (clone 14D7, 1:5) was produced by Camargo Ortega et al.[67] Cross-adsorbed secondary antibodies to mouse or rabbit IgGs raised in goat and labeled with Alexa Fluor 405 (1:500), 488 (1:1000), 555 (1:1000), 647 (1:800) were all from Thermo Fisher Scientific. These were diluted in 10% blocking solution and incubated with cells at room temperature for 1 h. After immunolabeling, coverslips were mounted in Prolong Diamond (P36965) or in Prolong Gold with DAPI (P36931) from Thermo Fisher Scientific) and left to cure for at least 5 days before imaging.

MT regrowth experiment

Neurons were transfected with pEGFP-NEDD1-gTBD and pAcGFP-Cdk5rap2-CTD (N-gTBD+C-CTD) or pβactin-AcGFP-CI and pCS-Centrin2-tdTomato as a control. MTs were completely depolymerized by treatment of DIV1 neurons with (6 to 10) μM nocodazole in the cell culture incubator for 4 h. Coverslips were then quickly washed 4 times with 7 mM Hepes-buffered Hanks' Balanced Salt Solution (14025050, Thermo Fisher Scientific) at 35°C and immediately incubated in equilibrated N2-medium[138] at 35°C for indicated time periods (90 s, 2 min, 3 min and 15 min) to allow MTs to regrow. The MT regrowth time included the washing steps which were typically finished in 55 s. Neurons were fixed using the PHEM buffer (at 35°C) and stained for βIII-tubulin.

Fluorescence microscopy

Imaging of fixed immunolabeled neurons was done at room temperature. Zstacks were acquired on a DeltaVision Core system at 0.2 μm spacing and deconvolved using the built-in Softworx deconvolution algorithm. A 100x/1.40 N.A. oil objective was used for imaging of the centrosomes (Figures 1C, 1F, S4A, and S4C), a 60x/1.42 N.A. oil objective was used for imaging MT regrowth experiments (Figure 1K) and Akap9 displacement from the Golgi (Figure S3B); a 20x/0.85 N.A. oil objective was used for imaging neuronal

morphology (Figures 2B and 3D). Alternatively, Zeiss Observer.D1 equipped with a 25x/0.8 N.A. water/oil immersion or 20x/0.8 N.A. air objective for imaging neuronal morphology (Figures 4D, S2A, and S2C), and a 100x/1.40 N.A. oil objective was used for imaging centrosomes after centrosome laser ablation (Figure S1F).

Images acquired with 60x and 100x objectives on the DeltaVision were deconvolved by Softworx and images corrected for chromatic shift by imaging of 0.1 μm Tetraspeck microspheres (T7279, Thermo Fisher Scientific) mounted on the same coverslip type and with the same mounting media as neuronal samples.

Live cell imaging

Transfected neurons were plated on μ-Slide 8 Well Glass Bottom slides (80827, ibidi). For all experiments, neurons were initially plated in MEM supplemented with 10% horse serum and then switched to astrocytes-conditioned N2 medium.[130] All live-cell imaging was performed in astrocytes-conditioned N2 medium.

Live cell imaging was performed on the DeltaVision Core (Centrosome) or Elite (Golgi) in an environmental chamber maintaining 37°C and equipped with an air supply containing 5% CO_2. Image acquisition parameters were empirically determined to balance signal quality and phototoxicity. 5% to 10% neutral density filters were used to keep the illumination intensity of neurons with blue light (GFP excitation) low.

For measurement of centrosomal MT nucleation (Figures 1H–1I, 3B, 3C, 4B, 4C, S1C, and S1D), neurons were always co-transfected with pβactin-EB3-mNeonGreen, to visualize growing MT plus tips, together with pCS-Centrin2-tdTomato or pβactin-td-mCherry-Cdk5rap2-CTD (C-CTD) or pβactin-mOrange2-NEDD1-gTBD (N-gTBD); or their combination (N-gTBD+C-CTD); or td-mCherry-Cdk5rap2; or pβactin-Nedd1-mOrange2; or pβactin-PACT-mOrange2-hCM1; or pβactin-Nedd1-mOrange2-rCM1 or pβactin-Nedd1-mOrange2-F75A; or pβactin-Nedd1-mOrange2-hCM1; or pβactin-Akna-mOrange2. To visualize the centrosome in neurons expressing N-gTBD, neurons were co-transfected with pCS-Centrin2-tdTomato. The rest of the tested proteins localized clearly to the centrosome, enabling its tracking in the red fluorescence channel. The centrosome was visually located in the red fluorescence channel and a 1.5 μm thick z-stack was defined to obtain the whole centrosomal signal. The optical axis integration (OAI) option was used to gather all possible EB3 tracks emanating from the centrosome. During acquisition, the shutter is opened, while the table moves in the z-axis direction along the predefined (1.5 μm) range and exposure time. Time-lapse imaging of EB3-mNeonGreen and the centrosome signal in the red channel was performed using OAI scan of 1 s intervals for 3 minutes. A 60x/1.42 N.A. oil objective and GFP/mCherry, or alternatively GFP/TRITC dichroics, was used with corresponding emission and excitation filters. The resulting time-lapse sequences were deconvolved by DeltaVision Softworx. To improve visualization in Figures 1H, 3B, 4B, and S1C, EB3 signal was boosted by subtracting Gaussian blurred images (σ = 1.5 pixels minus σ = 5 pixels) before making MIPs in Fiji.[134]

For measurement of Golgi-mediated MT nucleation (Figure S3D), neurons were always co-transfected with pCAG-EB3-mNeonGreen, pmScarlet-Giantin-C1 to visualize the Golgi and pβactin-Halo-Tag as control or pCAG-Halo-Tag-128-425-Akap9 encoding Akap9-dis. To visualize the Halo Tag, a stock solution of Janelia Fluor® Halo-Tag® ligand (646) (Promega) in DMSO (0.14 μg/μl) was diluted 1:1000 in conditioned N2 media to the final concentration and added to the neurons. Cells were incubated for 30 min at 37°C 5% CO_2. Subsequently cells were then washed three times with fresh conditioned N2 medium before imaging. Time-lapse imaging of EB3-mNeonGreen and the Golgi signal in the red channel was performed with 1 s intervals for 3 minutes. A 60x/1.42 N.A. oil objective and FITC/TRITC dichroic was used with corresponding emission and excitation filters. The resulting time-lapse sequences were deconvolved by DeltaVision Softworx.

For long term live imaging of neuronal polarization (Figures 2E and 2F), neurons were transfected either with pβactin-mOrange2-CI and pEGFP-Centrin2 as a control or with pβactin-AcGFP-Cdk5rap2-CTD (C-CTD) and pβactin-EGFP-NEDD1-gTBD (N-gTBD). Separately transfected control and N-gTBD+C-CTD expressing neurons were mixed and plated into the same well. Imaging started 7 h after plating of neurons to allow time for expression of transfected plasmids. Images were acquired every 15 min for 80 h using a 40x/1.35 N.A. oil objective. Images of whole neurons were acquired after the end of the time-lapse and stitched using the MosaicJ plugin of Fiji.[147] Neurite length measurements were performed using Simple Neurite Tracer plugin of Fiji.[135]

For measuring centrosomal MT nucleation *ex vivo*, the brain of E14.5 mouse embryos were *in utero* electroporated with three plasmids including a dual Cre/Dre activatable MT plus tip reporter pβactin-DIO-inv[rox-STOP-rox-EB3-mNeonGreen-bGH] together with pCAG-rox-inv[Tα1-iCre-pA]-rox-mNeonGreen-hCentrin and either pCAG-loxP-inv[Tα1-HA-Dre]-lox-Akna-mOrange2 or pCAG-lox-inv[Tα1-HA-Dre]-loxP-NEDD1-gTBD-mOrange2. For control groups, brains were electroporated with pCAG-lox-STOP-lox-EB3-mNeonGreen, pCAG-lox-inv[Tα1-iCre-pA]-lox-mOrange2 and pCAG-lox-inv[Tα1-iCre-pA]-lox-mNeonGreen-hCentrin. After *in utero* electroporation, the embryos were allowed to continue their development for two days, subsequently sacrificed and their brains sliced in a vibratome as previously described. Slices were transferred to μSlide 8 Well Glass Bottom slides (80827, ibidi) and imaged with the DeltaVision Elite equipped with an incubation chamber which was maintained at 37°C and 5% CO_2. Time-lapse imaging of EB3-mNeonGreen and the centrosome signal in the green channel was performed using 1.0 μm thick z-stacks with the interval of 0.2 μm between sections and 1 s interval between z-stacks for 2 minutes. A 60x/1.42 N.A. oil objective and GFP/mCherry or GFP/TRITC dichroics were used with corresponding emission and excitation filters. The resulting time-lapse sequences were deconvolved by DeltaVision Softworx.

For imaging of n-c coupling *ex vivo*, brains were IUE at E14.5 with pCAG-lox-inv[Tα1-iCre-pA]-lox-mOrange2 and pCAG-lox-inv[Tα1-iCre-pA]-lox-mNeonGreen-hCentrin (Ctrl); pCAG-lox-inv[Tα1-HA-Dre]-lox-Akna-mOrange2 and pCAG-rox-inv[Tα1-iCre-pA]-rox-mNeonGreen-hCentrin (Akna); pCAG-lox-inv[Tα1-HA-Dre]-lox-NEDD1-gTBD-mOrange2 and pCAG-rox-inv[Tα1-iCre-pA]-rox-mNeonGreen-hCentrin (N-gTBD). Brain slices were then imaged every 30 min in tiled 30 μm to 50 μm z-stacks for an additional 10 h to 15 h using an LSM880 confocal microscope (Zeiss) equipped with a CO_2 regulated incubation chamber maintained at 37°C and an objective C-Achroplan 32x/0.85 W Corr M27 VIS-IR (Zeiss). Stitching of the tiles was performed in Zen 2.3 sp1 software and analyzed with Fiji.

Centrosome ablation

Centrosome ablation was performed as described previously.[25] Only neurons without neurites (stage 1; Banker[148]), expressing Centrin2-EGFP, were used for centrosome ablation. Success of centrosome ablation was evaluated 2 days later in fixed neurons stained for γ-tubulin and Pericentrin. Absence of their fluorescence signal was considered as successful centrosome ablation. Neurons that retained γ-tubulin and Pericentrin centrosome-like signal detectable, despite the laser ablation attempt, were assigned to a second control group, 'Failed centrosome ablation'. Illustrative images were rotated using Fiji and stitched using MosaicJ.

FRAP

FRAP was performed on DIV1 neurons expressing Nedd1-mNeonGreen, Tubg1-mNeonGreen or Tubg1-mNeonGreen together with Nedd1-mOrange2. A 60x/1.42 N.A. oil objective, a GFP filter cube and a 488 nm laser on DV Elite was used for point bleaching guided by the Photokinetics (PK) module of the Softworx software. The environmental conditions were the same as described above for a typical live imaging experiment above.

Adaptive time intervals option was used with an estimated half-time of 1 s, 5 pre-bleaching event images and 80 post bleaching-event images with a constant exposure time of 200 ms. Bleaching laser parameters were kept constant.

In Utero Electroporation (IUE)

IUE was performed as described in Alfadil et al.[132] Briefly, timed-pregnant C57BL/6J mice (Janvier) carrying E14 embryos were anesthetized under a constant flow of isoflurane (Abbot) and the uterus was carefully exposed from the abdominal cavity. Throughout the surgery, warm saline was used to prevent dehydration. The lateral ventricles of the embryos were filled with 2 to 3 μl of a 10:1 mix of EndoFree DNA of interest and Fast Green dye (Sigma) using micropipettes pulled in a pipette-puller device (Zeitz) and a Picospritzer III microinjection device (Intracel). The DNAs used for electroporation included, pCAG-lox-inv[Tα1-iCre-pA]-lox-mOrange2-NEDD1-gTBD; pCAG-lox-inv[Tα1-iCre-pA]-lox-Nedd-1-mOrange2-rCM1; pCAG-lox-inv[Tα1-iCre-pA]-lox-Akna-mOrange2; pCAG-lox-inv[Tα1-Dre-pA]-lox-mOrange2-Cdk5rap2-CTD, pCAG-loxSTOPlox-ZsGreen; pCAG-loxSTOPlox-LynEGFP; pCAG-DIO-inv[roxSTOProx-ZsGreen-bGH]; pTα1-Dre, pCAG-lox-roxSTOProx-tRFP-pA-lox; and pCAG-lox-roxSTOProx-lyn-mScarlet-pA-lox. Forcep-like electrode paddles (Platinum Tweezertrode) controlled by an ECM 830 electroporator (both from BTX Harvard Apparatus) were used to deliver 5 pulses at 35 mV at duration of 50 ms and 600 ms intervals. Following the electroporation of all embryos, the uterus was returned into the abdomen, which was carefully stitched and closed. The mother was sacrificed at E18. Alternatively, the mother was allowed to deliver and kept with the pups until they reached P2, when both mother and pups were sacrificed. In either case, brains were extracted from the embryos and processed for histological analysis.

Ex Utero Electroporation (EUE) and Organotypic Culture of Brain Slices

Timed-pregnant C57BL/6J mice (Janvier) carrying E14 embryos were extracted from the uterine sack, injected with pCAG-lox-STOPlox-LynEGFP paired with either of the plasmids pCAG-lox-inv[Tα1-iCre-pA]-lox-mOrange2-NEDD1-gTBD, pCAG-lox-inv[Tα1-iCre-pA]-lox-Nedd-1-mOrange2-rCM1, or pCAG-lox-inv[Tα1-iCre-pA]-lox-Akna-mOrange2, and electroporated. The same electrodes and electroporator described for the IUE procedure above were used to deliver 5 pulses at 54 mV with a duration 50 ms and 1 s intervals. Immediately after, the heads of the embryos were collected in Gey's Balanced Salt Solution (GBSS, Sigma) supplemented with 0.5% glucose (GBSS-Glucose) and the brains extracted under scope. The brains were subsequently embedded in 4% low-melting point agarose (Biozym) and cut in 180 μm thick coronal sections (flanking the electroporated areas) using a VT1200 vibratome (Leica). Brains were always kept and cut in cold GBSS-Glucose. The brain slices were placed on 30 mm Polytetrafluoroethylene (PTFE) membranes (Millipore) in 35 mm transwell plates (Fluorodish, WPI) with slice media [Neurobasal 1X, FCS 5%, B27 supplement 1:50, Glutamax 1:400, penicillin/streptomycin 1:200 (all from Thermo Fisher), horse serum 5%, Neuropan-2 supplement 1:100 (from Pan-Biotech, pH = 7.3)]. 20 h to 30 h after culturing them, sections were imaged every 15 min in tiled 30 μm to 50 μm z-stacks for an additional 16 h to 20 h using a LSM880 confocal microscope (Zeiss) equipped with a CO_2 regulated incubation chamber maintained at 37°C and an objective (Plan-Apochromat 10x/0.45 N.A. M27-FWD = 2.1 mm dry, Zeiss). Stitching of the tiles was performed in Zen 2.3 sp1 software and analyzed with Fiji.

Immunohistochemistry

The heads of the mouse embryos or pups were fixed in 4% paraformaldehyde, 4% sucrose in phosphate-buffered saline (PBS) at RT for 2 h and then at 4°C overnight. The fixed heads were cryopreserved through incubation in 30% sucrose in PBS for 48 h. Brains were extracted, rinsed in PBS, embedded in Surgipath® cryo-gel (Leica) and frozen. The frozen brains were then cut with a cryostat (Leica)

into 25 μm to 50 μm thick coronal sections and adhered to positively charged microscopy slides (Superfrost, Thomas Scientific). The brain sections were warmed to room temperature and further adhered to the slides by baking at 65°C for 1 h. Next, the cryoembedding medium was washed with PBS and the sections let to hydrate for 30 min in PBS. Then, the cryosections were permeabilized in 0.3% Triton X-100 for 30 min and blocked with 5% normal donkey serum (NDS, Sigma) - or 10% normal goat serum (NGS) when antigen retrieval was used - plus 0.3% Triton X-100 in PBS (all performed at RT) for 1 h. The brain sections were incubated overnight at 4°C with the primary antibodies diluted in PBS. Anti-Ctip2 (ab18465, 1:100), anti-GFP (ab13970, 1:1000), anti-Ki67 (ab16667, 1:200), anti-Pericentrin (ab4448, 1:200), anti-Tbr1 (ab31940, 1:50); Satb2 (ab51502, 1:100) were from Abcam; anti-Pericentrin from Covance (#PRB-432C, 1:500); anti-RFP [recognizing specifically mOrange2, mScarlet and mCherry; (600-401-379, 1:1000 or 600-901-379, 1:1000)] from Rockland; anti-NeuN (ABN90P, 1:300) and anti-Map2 (AB5622, 1:500) from from Millipore; anti-γ-tubulin (T6557, 1:300) from Sigma. After washing three times with PBS, cryosections were incubated with Alexa Fluor conjugated secondary antibodies (1:300-400) at RT for 2 h. Of note, the performances of anti-NeuN and anti-GFP/RFP antibodies were greatly impaired when used after antigen retrieval treatments; therefore, we developed a two-step fixation-staining approach to overcome the loss of antibody sensitivity. Briefly, a regular immunohistochemistry procedure is performed with the antigen retrieval-sensitive primary antibodies, followed by the selected secondary antibodies and subsequent PBS washes as described above. Next, the stained brain sections and the primary/secondary antibodies complexes formed within were re-fixed on slides in 4% paraformaldehyde/4% sucrose in phosphate-buffered saline (PBS) at RT for 15 min. Subsequently, the slides were gently washed 3 times in PBS, dried and baked again in a hot plate at 65°C for 5 min to ensure tissue attachment. Next, the tissue sections received antigen retrieval treatment by incubation with 10 mM Tris/1 mM EDTA, pH 9.0 buffer supplemented with 0.05% of Tween-20 at 95°C for 10 min (GFP/NeuN/Ki67) or 40 min (NeuN/Pericentrin/γ-Tubulin). After antigen retrieval the staining for the epitopes requiring retrieval continued as described above, starting from the blocking step. Alexa Fluor dyes resisted the high temperatures from the antigen retrieval procedure undamaged, even after 1 h at 95°C. Next, the sections were incubated with DAPI (Invitrogen, D21490), diluted 1:20000 from a 5 mg/ml stock, for 10 min and then washed three times with PBS before mounting with Fluoromount™ aqueous mounting media (Sigma). Epifluorescent tilescan images were acquired as z-stacks with a Plan-Apochromat 20X/0.95 N.A. autocorrect air objective (20X/0.8 N.A. at 1X magnification) using a CellDiscoverer 7 (automated boxed LSM900 confocal microscope; all from Zeiss). Images showing centrosomal colocalization of Pericentrin/γ-tubulin, NeuN (Figures 5B and 5C), layer markers and Map2 staining (Figure S8) were acquired as z-stacks with a Plan-Apochromat 40X/1.4 N.A. objective in an LSM800 confocal microscope (Zeiss). Tiled images were stitched with Zen 3.1 software blue edition (Zeiss) and maximum intensity projection of the images were produced and analyzed using Fiji or Imaris. NeuN images were modified to remove unspecific speckles signal using the Fiji function "Remove Outliers" with the following parameters: size = 6 pixels, threshold = 50 (Bright). Gaussian Blurr was applied using 1 sigma. The resulting images were projected using maximum intensity projection in Fiji.

Clearing of brain sections and imaging

Paraformaldehyde-fixed E18 brains from embryos electroporated at E14 were sliced in 1 mm to 2 mm thick coronal sections comprising the electroporated area and washed overnight in PBS supplemented with 0.02% NaN$_3$ and 10 μg/ml Heparin (both from Sigma). Next, the sections were cleared following the CUBIC protocol described previously.[149,150] Briefly, PBS was removed from the sections and replaced with a 50% water dilution of CUBIC L reagent (TCI chemicals) and left with gentle agitation overnight at 37°C. The following day, the 50% CUBIC-L reagent was removed and replaced by 100% CUBIC-L reagent and left overnight at 37°C with gentle agitation. The next day, the 100% CUBIC-L reagent was removed and the sections were washed 4 times, 2 h each, with PBS. After washing steps, PBS was removed and replaced with a 50% water dilution of CUBIC-R+ reagent (TCI chemicals) and left with gentle agitation overnight at 37°C. The following day, the 50% CUBIC-R+ reagent was removed and replaced by 100% CUBIC-R reagent and let overnight at 37°C with gentle agitation. The cleared brain coronal sections were imaged with a 2-photon microscope (LSM 7MP, Zeiss) equipped with a Spectra Physics InSight X3 laser set at 920 nm and a Plan Apochromat 20x/1.0 N.A. DIC D = 0.17 M27 FWD 1.7 mm water objective (Zeiss). Images were 3D-reconstructed for further analysis using Imaris 9.2 software (Bitplane).

Experimental design

All experiments were repeated at least 3 times (N ≥ 3) and were not blinded. Sample size estimation was not based on a statistical model.

QUANTIFICATION AND STATISTICAL ANALYSIS

Image analysis

DIV1 neurons expressing pβactin-AcGFP-Cdk5rap2-CTDΔCBD, pβactin-AcGFP-Cdk5rap2-CTD (C-CTD), pβactin-EGFP-NEDD1-gTBD (N-gTBD), their indicated combinations or pAcGFP-C1 as a control were used in Figures 1C–1G. DIV1 and DIV5 neurons expressing Nedd1-mOrange2, Nedd1-mOrange1-rCM1, Nedd1-mOrange2-F75A or mOrange2 as a control were used in Figures S4A and S4B. DIV1 and DIV5 neurons expressing pCAG-Akna-IRES-EGFP or pCAG-IRES-EGFP as a control were used in Figures S4C and S4D.

Centrosomal signal in cultured neurons was automatically detected in deconvolved images using Surface Function in Imaris 8.1.2. 'Surface Area Detail Level' was set to 2 pixels (0.128 μm). Thresholding was performed using Background Subtraction (Local Contrast) with 'Diameter of the Largest Sphere Which Fits Into an Object' set to 1 pixel (0.064 μm). The lower threshold value was constant for all conditions for a given fluorescence channel in each experiment. Intensity sum for the whole centrosomal signal was measured in every cell.

γ-Tubulin and Pericentrin in E16, E18 and P2 mouse brain coronal sections (Figure 5) were automatically detected in confocal z-stacks using Surface function in Imaris 9.7.2. The z-stacks were in some cases rotated using Fiji (Bilinear interpolation) prior to analysis to enable cutting of 100 μm wide stripes incorporating all cortical layers. These 100 μm stripes were acquired from all brains, saved as.tif images using Fiji and then analysed in Imaris. 'Surface Area Detail Level' was set to 1 pixel (0.155 μm). Thresholding was performed using Background Subtraction (Local Contrast) with 'Diameter of the Largest Sphere Which Fits Into an Object' set to 1 pixel (0.155 μm). Due to the vast range of signals of Pericentrin and γ-tubulin foci (the latter in particular exhibited greatly decreased intensity in upper cortical layers), two sets of threshold values (stringent and medium) for both channels were used to detect as many γ-tubulin positive (γ-Tub+) and Pericentrin positive (Pcnt+) foci as possible. The threshold values were manually adjusted to maximally detect the centrosomal signal in the VZ. The thresholds could not be set as constant for all measured brain slices, since the staining intensity was variable among different brains. The detected foci were further restricted by a size of at least 5 pixels and an area of less than 4 μm². The foci detected using medium stringency (i.e., lower) threshold were set to exclude the foci that were previously detected using the stringent threshold, to avoid duplication of identical foci. Only γ-tub+ foci that overlapped at least 1E-06 μm³ with Pcnt+ foci were quantified and visualized as the center of their mass as black squares of uniform size, regardless of γ-tubulin or Pericentrin intensity in the given foci.

Deconvolved βIII-tubulin images were additionally background-subtracted with the Rolling Ball algorithm in Fiji using 15 pixels diameter. The fluorescence intensity sum at the centrosome in MT regrowth experiments (Figures 1K and 1L) was measured in Imaris as described above for the centrosomal signal, with a larger pixel size (0.106 μm) due to use of the 60x/1.42 N.A. oil objective.

Quantification of Akap9 intensity at the Golgi

Deconvolved images were used to measure the Golgi signal using the Surface function in Imaris 9.5.1. Surface Detail value was set to 2 pixels (0.216 μm). Thresholding was performed using background substraction (Local Contrast) with ''Diameter of the largest Sphere which fits into an Object'' set to 1 pixel (0.108 μm). The lower threshold value was constant for all conditions for a given fluorescence channel in each experiment.

Quantitative analysis of EB3 comets emanation from the centrosome and from the Golgi

We used u-track 2.1.3 (https://github.com/DanuserLab) from the Danuser laboratory[136] for detection of centrosomes or the Golgi and EB3 tracks in deconvolved time-lapse sequences. For detection of the centrosomes, the 'Gaussian Mixture-Model Fitting' method was used on the centrosomal fluorescence channel with all parameters set to default, with the exception of 'Alpha-Value for Comparison with Local Background' set to 0.01 and the 'Use Rolling Window Time Averaging' set to 5 frames. For tracking, 'Maximum Gap to Close' was set to 4 frames and 'Minimum Length of Track Segments' was set to 2 frames. 'Cost Functions'' and ''Kalman Filter Functions' were all set to 'Brownian + Directed Motion Models' with default parameters. 'Track Analysis' was set to 'Motion Analysis' with default parameters.

For the detection of EB3 comets, 'Comet Detection' was used on the EB3 fluorescence channel with the following parameters: 'Low-Pass Gaussian Standard Deviation' set to 1.5 pixels, 'High-Pass Gaussian Standard Deviation' set to 5 pixels, and 'Watershed Segmentation' parameters of 'Minimum Threshold' set to 4 standard deviations (SD) and 'Threshold Step' set to 1.1 SD. For tracking, 'Maximum Gap to Close' was set to 3 frames, 'Minimum Length of Track Segments' set to 3 frames. 'Cost Functions' were all set to 'Microtubule Plus-End Dynamics'. Step 1 'Frame-to-Frame Linking' parameters were: 'Brownian Search Radius', 'Lower Bound' set to 1 pixel, with 'Upper Bound' set to 8 pixels, 'Multiplication Factor' set to 3, and 'Number of Frames for Nearest Neighbor Distance Calculation' set to 4. Step 2 'Gap Closing, Merging, Splitting' parameters were: 'Break Non-Linear Tracks' checked, 'Maximum Forward Angle' set to 30 degrees, 'Maximum Backward Angle' set to 1 degree, 'Maximum Shrinkage Factor Relative to Growth Speed' set to 1.5, and 'Fluctuation Radius' set to 1 pixel. 'Kalman Filter Functions' were set to 'Search Radius for First Iteration' which was set to 20 frames.

Detected centrosomal signal tracks (in red channel) were manually picked up based on the sum of the centrosome fluorescence channel in the whole time-lapse sequence. Only EB3 tracks starting inside the 0.8 μm radius surrounding the detected centrosomal signal were automatically filtered by an in-house written macro (Process_EB3_centrosome_Golgi_areas.py) and considered centrosomal. The detected EB3 tracks were overlaid on top of the original time-lapse sequences in Videos S1 and S4 using the in-house written macro utilizing output data of u-track.

For assignment of EB3 tracks to the Golgi, an area occupied by Golgi was manually selected using Lasso function in Python based on the sum of the Golgi fluorescence channel in the whole time-lapse sequence. Only EB3 tracks starting inside the Golgi area were automatically filtered by the in-house written macro and considered of Golgi origin. The detected EB3 tracks were overlaid on top of the original time-lapse sequences in the Video S3 using the in-house written macro utilizing output data of u-track. The macro is publicly available in Zenodo (see the key resources table).

For analysis of centrosomal MT nucleation *ex vivo*, we manually tracked EB3 comets emanating from the centrosome labeled by Centrin1 using a plugin MtrackJ[137] in Fiji.

Quantitative analysis of neuronal polarization

Neurons were labeled with anti-βIII-tubulin and Tau-1 antibodies to stain neuronal MTs and Tau protein specifically in axons, respectively (Figures 2B–2D, 3D–3F, and 4D–4G). DIV1 and DIV2 neurons expressing AcGFP-Cdk5rap2-CTD together with EGFP-NEDD1-gTBD (N-gTBD+C-CTD) or AcGFP only as a control were compared in Figures 2B–2D. DIV2 neurons expressing Nedd1-mOrange2, Nedd1-mOrange2-rCM1, Nedd1-mOrange2-F75A and mOrange2 only as a control were compared in Figures 3D–3F. DIV2 neurons expressing Akna-mEGFP and AcGFP only as a control were compared in Figures 4D–4G. In the case of Figures 2E, 4D, and S1G, the tile-scanned images were stitched in Fiji (MosaicJ). For quantifications of DIV1 and DIV2 neuronal morphology, the tile-scanned images acquired on DeltaVision were stitched with our in-house macro (stitch.py, publicly available in Zenodo, see the key resources table). The only exception was the quantification of data in Figures S3F–S3H that were based on the tile stitching done in Zen software (Zeiss).

DIV1 and DIV2 neurons were classified into 3 groups: stage 1 neurons did not have any neurite (wo. neurites), stage 2 neurons (w. neurites) had at least 1 neurite (a process longer than 10 μm and thinner than 2 μm in the thinnest region between the soma and growth cone), and stage 3 neurons (w. axon) had one or more axons (a process longer than 100 μm, positive for Tau-1 gradient). Length of the longest neurite was measured only in stage 2 and 3 neurons (zeroes from stage 1 neurons were not included in the calculation).

In time-lapse sequences (Figures 2E and 2F), measurement of the time of the first neurite outgrowth was based on the same minimal definition of a neurite as above. The axon was defined retrospectively as the longest neurite that persisted until the end of the time-lapse sequence (DIV4) and was longer than 100 μm. Stitching of images needed for the reconstruction of the whole axon was performed in MosaicJ plugin of Fiji.[147] Tracing of neurites was performed using Simple Neurite Tracer plugin of Fiji.[135]

DIV5 neurons were labeled with anti-βIII-tubulin and Tau-1 or with anti-Map2 and Tau-1 (Figure S2). The tile-scanned images were stitched in Zen software (Zeiss). Neurites were traced using the Simple neurite tracer plugin of Fiji. Axons and dendrites were classified manually based on Tau-1 and Map2 staining. Neurites with distal Tau-1 gradient and without Map2 staining were classified as an axon. Neurites with Map2 staining were classified as a dendrite.

FRAP analysis

The centrosome signal (only one centriole per cell was tracked in the instance of two distinct centrosomal signals) was encircled manually in Fiji by a circular ROI (the centrosome) of 5 pixels in diameter (corresponding to 541.2 nm) and tracked manually throughout the acquired FRAP timelapse sequence. To find local fluorescence intensity maximum, the Lookup table (LUT) 'Thermal' was employed. Subsequently, a ROI (the whole cell) was manually drawn around the measured cell. Finally, background mean fluorescence intensity was measured in a random ROI (background) outside the area occupied by cells. Mean fluorescence intensity was measured in every frame in all three ROIs.

The value of background fluorescence mean intensity was subtracted from the centrosomal and the whole cell mean fluorescence intensity. The background-subtracted fluorescence signal in 5 pre-photobleaching images was then averaged in the centrosomal and the whole cell datasets, and this average was used for normalization of the centrosomal and the whole cell fluorescence intensity, respectively. The relative centrosomal signal was corrected for a general fluorescence loss after photobleaching by dividing it by the relative whole cell signal in a given frame. The resulting centrosomal corrected relative fluorescence intensity was further normalized by setting the fluorescence intensity in the first image after photobleaching to zero using the following formula: normalized corrected relative fluorescence intensity at the centrosome$_i$=("Corrected relative fluorescence intensity$_i$" - "Corrected relative fluorescence intensity in the first frame after photobleaching")/(1 - "Corrected relative fluorescence intensity in the first frame after photobleaching"); i=frame number (85 frames in total). Only post-photobleaching time points are shown in the FRAP curves in Figure S4G. Only cells with low to moderate expression of studied proteins were analyzed.

Nucleus-Centrosome coupling analysis

NC coupling analysis was performed as described in Gonçalves et al.[9] Briefly, Fiji "straight line" was used to measure nuclear displacement and nuclear centrosome distance. Nuclear displacement, starting from the point of origin at t = 0, was measured every 30 mins for 10 hours. For measuring nuclear displacement, a line was drawn connecting the centre of the nuclei from one time-point to the next. If the nucleus migrates upwards (in the positive direction) the value is summed to the previous value. However, if the nucleus moved downwards (in the negative direction) the value is subtracted from the previous value. Similarly, the distance between the nucleus and the centrosome was also measured at each time point using the line tool. A line was drawn connecting the centrosome and the nucleus. Finally, the nuclear-centrosome distance was added to the nuclear displacement and values were plotted.

Speed and directionality analysis

Speed of migration in organotypic slices (Figure 6O) was automatically tracked using the Spots function in Imaris 9.8. Spot diameter was set to 7.50 μm. Spots tracking was executed using the "Autoregressive Motion" algorithm. For directionality analysis (Figures 6M and 6N), the videos were orientated so that the cortical column is at 90°. The starting [X1, Y1] and end [X2, Y2] coordinates for each

tracked neuron were used to calculate the angle (α) between the line connecting the starting and final position of the neuron and the vertical line using arccosine function in MS Excel. The directionality of neuronal migration was finally calculated using the folowing formula:

$$Directionality = \frac{Cell\ displacement}{Cell\ trajectory\ length} \cdot cos\ \alpha$$

Depending on whether the neuron migrated straight up, laterally or down, the angle coefficient (cos α) will be close to 1, 0 or -1, respectively.

Statistical analyses

Generally, for comparisons of one-parameter data in multiple groups, we tested first whether ordinary one-way ANOVA is appropriate using the built-in Brown-Forsythe test build in Prism (GraphPad Software). If an ordinary one-way ANOVA could not be used, we used Brown-Forsythe and Welch ANOVA tests with Games-Howell's multiple comparisons test. For comparisons of only two groups, un-paired Welch's t-test was applied. For two-parameter grouped data (e.g., groups vs. multiple bins), we used two-way ANOVA with Šídák's or Tukey's multiple comparisons test. The used statistical test is always indicated in the figure legend.

Distribution of fluorescence intensities of centrosomal proteins was non-normal (Figures 1D, 1G, S4B, and S4D) and skewed from one side (though not negative, it was zero on several occasions, which was especially pronounced in displacement experiments). We used a generalized linear model (GLM) run in R (https://www.r-project.org/) to test if expression of constructs of interest had a positive or negative effect on the intensity values. The outcomes (intensities) were modeled using a γ-distribution with an inverse link function. The reference for comparison was AcGFP-C-CTDΔCBD (Figure 1D), AcGFP (Figure 1G), mOrange2 (Figure S4B) and pCAG-IRES-EGFP (Figure S4D) expressing neurons. Multiple comparisons were performed using Simultaneous Tests for GLM (R multcomp package).

Counts of EB3 tracks per minute were analysed by GLM using a Poisson distribution, followed by Simultaneous Tests for GLM (Figures 1I, 3C, 4C,and S1D). The microtubule regrowth experiment was analysed using Brown-Forsythe and Welch ANOVA tests with Games-Howell's multiple comparisons test (Figure 1L).

Neuronal polarization as quantified using fractions of neurons in different developmental stages was analyzed using the ordinal logistic regression model in R (polr; proportional odds logistic regression). The model assumes that the cell progresses from stage 1 to stage 2 and then to stage 3. We tested whether the speed of stage progression in the tested conditions is different from control and corrected for an experiment-dependent effect using "weight" parameter set to "freq" (weight == freq) (Figures 2C, 3E, 4F, and S3G). The length of the longest neurite, time of the first neurite formation and axon outgrowth in two-groups comparisons were analyzed using Welch's unpaired t-test (Figures 2D, 2F, and S3H). Length of the longest neurite in the centrosome ablation experiment was analyzed using ordinary one-way ANOVA with Tukey's multiple comparisons test (Figure S1H). For the length of the longest neurite measurements in multiple groups, we used Brown-Forsythe and Welch ANOVA tests with Games-Howell's multiple comparisons test (Figure 3F). Curve fitting using a build-in two-phase association model using default parameters (only Y_0 was set to 0) was performed in Prism (Figure S4G).

In vivo analysis: The relative axon density distribution from electroporated neurons in E18 brain coronal sections (Figures 6D, 7C, 7F, S3K, S7C, S7F, and S7I) was determined as follows. Using individual fluorophore-related channels, and the segmented line tool of Fiji, a line-scan covering the electroporated area (EA) was adjusted via line width to match the entire span of the cortex [VZ-marginal zone (MZ)], after which we proceeded to measure the fluorescence intensity in the EA (as mean grey values) along with a measure of the general background (GB) in a neighboring area. Next, using the segmented line tool, a line-scan was drawn following the axonal bundle (AB) from its exit from the EA until the last visible axon was surpassed for at least 200 μm. The width of the line was then adjusted to match the span of the IZ and a measure of the fluorescence intensity was taken as an intensity profile with plot profile tool. Note, the profile is considered to end when it consistently matches the background baseline for which the extra 200 μm taken after the last axonal signal was detected, serving as a background reference. The relative axon density (rAD) for each point of the profile over distance from the EA - normalized to the amount of electroporated neurons and corrected for channel-specific-related fluorescent background - was calculated as rAD = [(AB − GB)/(EA − GB)]. After a normalized intensity profile was generated, the area under the curve was calculated as $= \sum_{d=0}^{d}((rADd0+rADd1)/2 * (d1 − d0))$ where "d" is the distance from the EA and "rADd" the corresponding relative axon density at that distance. Analysis of P2 electroporated brain coronal sections was performed as described for E18 coronal sections. However, due to the fact that the corpus callosum (CC) funnels axons from neurons residing in different focal planes, normalizing the fluorescent axon intensity across the whole span of the axon bundle using a focal plane–specific measured EA intensity is inappropriate. Therefore, the fluorescent axon intensity is measured before axons enter and concentrate at the CC; in this case, namely the first 500 μm after axons exit the EA. This variation in the analysis method provides a more accurate representation of the axon contribution by electroporated neurons residing in that particular EA focal plane to the axon bundle. At least two consecutive coronal sections were analyzed for each brain. Values obtained after calculating the area under the curve were analyzed by unpaired Welch's t-test.

γ-Tub+ and Pcnt+ foci in E16, E18 and P2 brain slices were considered centrosomes (Figure 5B). These were classified based on their position in cortical layers (VZ, SVZ, IZ, CP) and plotted as a density of γ-Tub+ centrosomes per 100 μm^2 in a given layer. Differences in centrosome densities among the cortical layers during development were statistically evaluated using two-way ANOVA with Tukey's multiple comparisons test (Figure 5D).

The migration of electroporated neurons in E18 and P2 brain coronal sections was analyzed as follows. The signal of individual fluorophore-related channels was thresholded until cell bodies were the main source of signal and a grid of five equal rectangular ROI or 'bins' were continuously placed over the EA to cover the entire span of the cortex. The relative intensity in each bin was reported as percentage of the total signal (summed signal from the 5 bins). Statistical analysis of this data was performed by two-way ANOVA with Šídák's multiple comparisons test.

Active Cleaved-Caspase 3 (cCasp3) immunofluorescence was determined as follows. The signal of individual fluorophore-related channel was thresholded to eliminate background-associated signal until only cCasp3-positive cells were detected. Next, equally-sized ROIs were generated over representative regions of the control (tRFP) and target (ZsGreen plus constructs) EA, followed by measurement of fluorescence intensity. Statistical analysis of this data was performed by unpaired Welch's t-test.

In Figure legends, "N" is used for the number of independent experiments, "n" is used for the number of cells (or brains in case of some *in vivo* experiments). An exception to this rule is Figures 8D–8F where "n" denotes number of measurements in the given video. Data are presented as means and error bars are SDs if not indicated otherwise in the figure legend. In boxplots, whiskers represent the 5th and 95th percentile, borders of the box represent the 25th and 75th percentile, the line in the middle is the median, and the mean is represented by +. Statistical significance means a P value (P) lower than 0.05.